

**Mechanics of Granular Materials:
Constitutive Behavior and Pattern
Transformation**

Cover image © Luca Galuzzi - www.galuzzi.it

Sand dunes of Wan Caza in the Sahara desert region of Fezzan in Libya.

Used under Creative Commons Attribution-Share Alike 2.5 Generic license.

Mechanics of Granular Materials: Constitutive Behavior and Pattern Transformation

PROEFSCHRIFT

ter verkrijging van de graad van doctor
aan de Technische Universiteit Delft,
op gezag van de Rector Magnificus prof.ir. K.C.A.M. Luyben,
voorzitter van het College van Promoties,
in het openbaar te verdedigen op maandag 2 juli 2012 om 10.00 uur

door

Fatih GÖNCÜ
Master of Science in Applied Mathematics,
École Normale Supérieure de Cachan, France
geboren te Ilgaz, Turkije

Dit proefschrift is goedgekeurd door de promotoren :

Prof. dr. rer.-nat. S. Luding

Prof. dr. A. Schmidt-Ott

Samenstelling promotiecommissie :

Rector Magnificus

Prof. dr. rer.-nat. S. Luding

Prof. dr. A. Schmidt-Ott

Dr. K. Bertoldi

Prof.dr.ir. L.J. Sluys

Prof.dr.-ing. H. Steeb

Prof.dr.ir. A.S.J. Suiker

Prof.dr. M. Liu

Prof.dr. S.J. Picken

voorzitter

Universiteit Twente, promotor

Technische Universiteit Delft, promotor

Harvard University, Verenigde Staten

Technische Universiteit Delft

Ruhr-Universität Bochum, Duitsland

Technische Universiteit Eindhoven

Universität Tübingen, Duitsland

Technische Universiteit Delft, reservelid

This research has been supported by the Delft Center for Computational Science and Engineering (DCSE).

Keywords: granular materials, pattern transformation, discrete element method

Published by Ipskamp Drukkers, Enschede, The Netherlands

ISBN: 978-94-6191-341-8

Copyright © 2012 by Fatih Göncü

All rights reserved. No part of the material protected by this copyright notice may be reproduced or utilized in any form or by any means, electronic or mechanical, including photocopying, recording or by any information storage and retrieval system, without written permission of the author.

Hatice ve Veysel'e

Summary

Mechanics of Granular Materials: Constitutive Behavior and Pattern Transformation

by F. Göncü

From pharmaceutical to mining or travelling desert dunes to earthquakes, granular materials are at the heart of many industries and natural phenomena. Improving the efficiency of the machines, handling them or, constructing safer buildings requires a critical understanding of their behavior. However, this is not a straightforward task as opposed to what one might think due to the abundance of particulate matter. From a fundamental point of view, it has been only recently realized that they cannot be easily classified as a solid or liquid or even a gas as they are able to mimic all of these states under slightly different conditions. The challenge of the scientific research today, is to establish the link between the collective behavior and properties of individual particles composing granular materials. Such a relation would enable to characterize them with only a few parameters in contrast to billions of particles typically found in practice.

In the first part of this thesis, we study the mechanical behavior of idealized disordered sphere packings with discrete element simulations. The polydispersity and coefficient of friction of the particles are varied systematically to characterize their influence on the macroscopic stress-strain response. In isotropically deformed packings, the critical volume fraction marking the transition from a solid to fluid like state increases with polydispersity, whereas it decreases with the coefficient of friction. The coordination number, i.e. average number of contact per particle, is discontinuous at this density. During decompression it drops from its isostatic value to zero and obeys a power law at higher volume fractions. The effect of polydispersity on the pressure is determined by the ratio of critical volume fraction and the contact density which is equal to the trace of the fabric times a correction factor that depends only on the moments of the particle size distribution. Using the micromechanical definition of the stress tensor, we derive an incremental constitutive model for the pressure which includes changes of fabric. With one fit parameter the linear regime of lower pressure

is described, while with two parameters, the model captures well the non-linear pressure evolution in isotropically deformed polydisperse, frictionless and frictional packings.

Anisotropic deformations are studied with triaxial test simulations. The shear strength of the packings is measured by the deviatoric stress ratio which first increases then saturates with increasing particle coefficient of friction. Volumetric strain also depends on the particle friction albeit in a non monotonic way. The maximum compaction after which packings start to dilate, is achieved at a relatively small coefficient of friction. The stress-strain response depends indirectly on the polydispersity which determines initial packing conditions. When initially the volume fraction is fixed, the pressure as well as the shear strength decrease with polydispersity. The opposite is observed when the initial pressure is imposed, although the effect of polydispersity on the stress-strain behavior is less significant in this case. Finally, a hypoplastic constitutive model is calibrated with simulation results and the resulting material coefficients are related to particle properties.

Most granular materials are amorphous and disordered as realized up to now. However, crystal structures can be built by placing uniform particles on a regular lattice. The second part of the thesis is about pattern transformation in two-dimensional granular crystals composed of bi-disperse soft and hard cylindrical particles. We show with experiments and simulations that upon uniaxial compression the particles undergo structural rearrangements from an initial square to hexagon-like lattice. It is found that the characteristics of the transformation strongly depend on the size ratio of the particles rather than their material properties. If the ratio is small enough the transformation is homogeneous and practically reversible.

The band structure of the granular crystal changes due to the pattern transformation. Using a linearized contact force model, we compute the dispersion relation at different levels of deformation and show that band gaps open and close as the structure of the crystal changes. This could find applications in tunable acoustic devices such as filters or vibration isolators.

In short, this thesis concerns the mechanics of granular materials subject to different modes of deformation. The constitutive behavior of disordered sphere packings and pattern transformation in regular arrays of cylinders have been studied.

Samenvatting

Mechanica van Granulaire Materialen: Constitutief Gedrag en Patroontransformatie door F. Göncü

Van farmacie tot mijnbouw en van wandelende woestijnduinen tot aardbevingen, granulaire materialen liggen in het hart van talrijke industriële processen en natuurlijke fenomenen. Het verbeteren van het rendement van verwerkingsmachines, het operationeel houden ervan, en het bouwen van veiligere gebouwen vereisen een essentieel begrip van de eigenschappen van granulaire materie. Dit is geen simpele opgave, in tegenstelling tot wat men zou verwachten gezien de overvloed aan granulaire materialen. Pas recentelijk is vanuit een fundamenteel standpunt het inzicht gekomen dat granulaire materie niet eenvoudig geklassificeerd kan worden als vaste stof, noch als vloeistof of als gas, maar dat granulaire materie kenmerkend gedrag van alle drie fasen kan vertonen onder kleine veranderingen van de omstandigheden. De uitdaging voor het hedendaags wetenschappelijk onderzoek is om een verband te vinden tussen het collectieve gedrag en de eigenschappen van de individuele deeltjes waaruit een granulaire materiaal bestaat. Met een dergelijke relatie zou een karakterisatie van een granulaire materiaal in termen van een paar parameters mogelijk worden, in tegenstelling tot de huidige beschrijving in termen van miljarden deeltjes.

In het eerste deel van dit proefschrift bestuderen we met discrete elementen simulaties het mechanisch gedrag van ideale ongeordende stapelingen van bollen. De grootteverdeling en frictiecoëfficiënt van de deeltjes zijn systematisch gevarieerd om hun invloed op het macroscopische stress-strain gedrag te karakteriseren. In isotroop vervormde stapelingen stijgt de kritieke volumefractie die de overgang van vaste stof naar vloeistof-achtig gedrag markeert met toenemende polydispersiteit, terwijl die fractie daalt bij toenemende frictiecoëfficiënt. Het coördinatiegetal, d.w.z. het gemiddelde aantal contacten per deeltje, is bij deze overgang discontinuë. Het zakt bij decompressie van de isostatische waarde tot nul en volgt een machtsfunctie voor hogere volumefracties. Het effect van polydispersiteit op de druk wordt bepaald door de verhouding van kritieke volumefractie en contactdichtheid; deze laatste is

gelijk aan het spoor van de structuurtensor van de stapeling vermenigvuldigd met een correctiefactor die alleen van de momenten van de deeltjesgrootte-verdeling afhangt. Gebruik makend van de micro-mechanische definitie van de stresstensor leiden we een incrementeel constitutief model af dat structuurveranderingen toestaat. Het lineaire regime voor lage spanningen wordt beschreven met n fitparameter, en het model geeft een goede beschrijving van de niet-lineaire spanningsontwikkeling in isotroop vervormde polydisperse stapelingen van deeltjes met en zonder wrijving.

Anisotropische deformaties zijn bestudeerd met tri-axiale test simulaties. De deformatieweerstand van de stapelingen is bepaald via de deviatorische spanningsverhouding, die eerst toeneemt en dan verzadigt met toenemende frictiecoëfficiënt. De volumetrische spanning hangt ook af van de frictiecoëfficiënt, maar op een niet-monotone wijze. De maximale compactie waarna een de stapeling begint te dilateren wordt bereikt bij een relatief lage frictiecoëfficiënt. Het stress-strain gedrag hangt indirect af van de polydispersiteit, via de invloed van laatstgenoemde op de vorming van een initiële stapeling. Bij constante initiële volumefractie nemen de druk en de deformatieweerstand af met toenemende polydispersiteit. Het omgekeerde wordt waargenomen bij een constante initiële spanning, al is in deze situatie het effect van polydispersiteit op het stress-strain gedrag minder groot. Tot slot is een hypoplastisch constitutief model geïjkt met simulaties resultaten en zijn de resulterende materiaal-parameters gerelateerd aan de deeltjes eigenschappen.

De tot nu toe besproken granulaire materialen zijn amorf en wanordelijk. Echter, granulaire kristallen kunnen gemaakt worden door uniforme deeltjes te stapelen in een regelmatig rooster. Het tweede deel van dit proefschrift behandelt patroondeformaties in tweedimensionale granulaire kristallen samengesteld uit zachte en harde cilindrische deeltjes met twee verschillende groottes. We laten met experimenten en simulaties zien dat een vierkant rooster onder uni-axiale compressie overgaat in een hexagonaal rooster. We vinden dat de karakteristieken van de overgang sterk afhangen van de grootte-verhouding van de deeltjes, terwijl de materiaaleigenschappen van de deeltjes van weinig belang zijn. Voor voldoende kleine ratio's verloopt de transformatie homogeen en vrijwel omkeerbaar.

De bandstructuur van het granulaire kristal verandert door de patroontransformatie. Met een gelineariseerd model voor de contactkrachten hebben we de dispersierelaties berekend voor verscheidene deformatiegraden en aangetoond dat een 'band gap' ontstaat en verdwijnt als de structuur van het kristal verandert. Dit effect zou toegepast kunnen worden in afstembare akoestische apparaten zoals filters en trillings-isolatoren.

Samenvattend, dit proefschrift beschrijft de mechanica van granulaire materie onder verscheidene vervormingen. Het constitutief gedrag van wanordelijke stapelingen van bollen en structuur-deformaties in ordelijke stapelingen van cilindres zijn bestudeerd.

Acknowledgements

About 5 years ago I graduated from an engineering school in France without knowing what to do next. The same year I had done an internship at Philips Research Laboratories in Eindhoven which gave me a zest of doing research. I decided hesitatingly to apply for a PhD in the Netherlands and sent an application for a project advertised with title “Hierarchical Computational Methods for Scale Bridging in Composite Materials” on the website of Delft Center for Computational Science and Engineering. The project turned out to be very different from what I expected but now I am really happy that I have taken this step forward. This thesis is the result of the following four years of research. The financial support from the Delft Center for Computational Science and Engineering is gratefully acknowledged. Along the way many people have contributed directly or indirectly to the completion of this thesis. I would like to thank all of them.

First of all my supervisor Prof. Stefan Luding deserves the biggest recognition for giving me the chance to join his group and introducing me to the research on granular materials. As a supervisor, he has been always patient, supportive and available, and gave me all the freedom I needed. As a person, he has been always kind, friendly and generous. I learned a lot from him not only about science but also how to be a good person. I would like to also thank Stefan and his wife Gerlinde for the many group dinners and gatherings they hosted.

An important part of this thesis would not be written if Prof. Katia Bertoldi had not proposed me to work on pattern transformation in soft granular crystals. I am grateful to her for this, and the wonderful time I spent in her research group at Harvard University. Katia is one of the most energetic and positive persons I have ever met. Her enthusiasm motivates everybody around her.

I would like to thank the committee members for their interest in my research. In particular, I am grateful to Prof. Andreas Schmidt-Ott for accepting to be my promotor in Delft and Prof. Mario Liu for joining the committee on a short notice. Prof. Bert Sluys has helped me to correct important mistakes in the thesis. Besides he is the one who forwarded my PhD application to Stefan.

I am indebted to Prof. Tom Mullin and Stephen Willshaw from Manchester University for their collaboration and hospitality during my short visit. Thanks also to JongMin Shim from Harvard University.

Most of this work has been carried out in the Multi Scale Mechanics group at the University Twente where I had the privilege to work in a truly international environment. I would like to thank my former and current colleagues in MSM Abhinendra Singh, Anjenet Mettievier Meyer, Anthony Thornton, Brian Lawney, Dinant Krijgsman, Holger Steeb, Katia Bertoldi, Kay Imole, Kazem Yazdchi, Kuniyasu Saitoh, Martin Robinson, Mateusz Wojtkowski, Micha-Klaus Müller, Nicolás Rivas, Nishant Kumar, Olaf Herbst, Orencio Durán Vinent, Orion Mouraille, Remco Hartkamp, Saurabh Srivastava, Sebastian Gonzalez, Sylvia Hodes-Laarhuis, Thomas Weinhart, Vanessa Magnanimo, Vitaliy Ogarko, Wouter den Breeijen and Wouter den Otter for the pleasant atmosphere. Moreover, thank you Anjenet, Sylvia and Wouter for the help with administrative and computer matters. Abhi, my longtime office mate, I will miss our discussions!

Although practically all of my time was spent at the University of Twente, I was also a member of the NanoStructured Materials research group in the department of Chemical Engineering. Karin Wilhelm and Wil Stolwijk have always made me feel welcome in Delft whenever I was there and helped with all administrative formalities. Thank you both!

Outside work I met a lot of nice people who helped me during my stays in the Netherlands and the US. My house mates deserve especially to be mentioned: Hamza, Hamdi, Ahmet, Salih, Burak, Ferhat, Alim, Eren, Murat and Kerem, Maxat, Kairat, Dauren, Nyssanbay thank you for your friendship! I will never forget all the dinners, trips and good times we spent together!

My brothers Ahmet and Ömer were always there to encourage and support me in difficult times. Finally I do not know how to express my gratitude to my parents. Their unconditional love, sacrifice and prayers have been the biggest support throughout this journey. This thesis is dedicated to them.

Fatih Göncü
Enschede, May 2012

Contents

Summary	v
Samenvatting	vii
Acknowledgements	ix
1 Introduction	1
1.1 Background: Granular materials	1
1.2 Jamming, force chains, granular crystals and sound propagation	3
1.3 Shear bands, dilatancy, constitutive laws and patterns	6
1.4 Scope and outline	9
2 Discrete and continuous models of granular materials	11
2.1 The Discrete Element Method	11
2.2 Micro-Macro transition: Averaging procedures	16
2.3 Analysis of the components of a hypoplastic constitutive model	18
3 Isotropic deformation of frictionless systems	25
3.1 Introduction	26
3.2 Simulation method	27
3.3 Evolution of the coordination number	31
3.4 Fabric Tensor	40
3.5 Pressure	43
3.6 Summary and Conclusion	49
3.A Determination of the critical volume fraction	51
4 Effect of particle friction and polydispersity	61
4.1 Introduction	62
4.2 Simulation setup	63
4.3 Isotropic deformations: Evolution of the pressure	64
4.4 Hypoplastic constitutive model	68

4.5	The triaxial test	70
4.6	Summary and conclusions	80
4.A	Calibration of the hypoplastic constitutive model	81
5	Pattern transformation in a soft granular crystal	85
5.1	Introduction	85
5.2	Experiments	87
5.3	Simulations	87
5.4	Results	88
5.5	Conclusions	93
5.A	Finite element simulations of contact and pattern transformation	94
6	Phononic band gaps in a two-dimensional granular crystal	99
6.1	Introduction	99
6.2	Modeling	100
6.3	Results	103
6.4	Discussion and conclusion	105
6.A	Wave propagation in periodic lattices	105
7	Conclusions and Recommendations	109
	References	113
	Curriculum vitae	123
	Propositions	125
	Stellingen	127

Chapter 1

Introduction

1.1 Background: Granular materials

A glass bead has no apparent difference from a block of glass except its extensive properties such as mass, volume, etc. However, when two or more beads are put together their behavior significantly deviates from the glass block. Depending on the volume they occupy and the external forces applied on them, the collection of beads behaves like a solid, a liquid or a gas. For example, when they are poured on a frictional surface or densely packed in a container they stay still like a solid and are able to resist external forces. On the other hand when the container is tilted they flow like a fluid. If we increase the external force even more i.e. shake the container they will fly around and bounce on to each other like gas molecules provided they have enough space.

Glass beads are not the kind of substance we encounter often but they belong to a broader class of materials which we are practically surrounded with: *Granular materials*. If we make a tour in the kitchen we will quickly notice that many of the food is in granular form: sugar, rice, coffee, cereals etc, Fig. 1.1. Walking outside we step on the soil which is particulate hence a granular matter. These are just a few examples of daily life from which one can easily realize the importance of granular materials. Their industrial applications are equally important and crucial for the society and our civilization. For example, mining and construction industries rely on the extraction, transportation and handling of rocks, gravels and sand. Similarly agricultural and pharmaceutical industries store, process and transport grains, powders and pills. In fact, granular materials are the second most manipulated raw materials after fluids [25]. Nevertheless, it is estimated that 40% of the capacity of the plants processing them is wasted [53].



Figure 1.1: Granular materials are ubiquitous in daily life. Sugar, rice, coffee or muesli are only a few examples from the kitchen.

Granular materials are assemblies of macroscopic objects. A glass bead is much larger than the atoms and molecules which compose it. The consequence of this is the irrelevance of temperature at the particle scale. The thermal energy of the bead is orders of magnitude less than its potential and kinetic energies when it is raised by its own diameter or moved at a speed of 1 cm/s [5, 53]. Actually, a definition of granular materials was given based on the lower limit of size (c.a. $1 \mu\text{m}$) of particle where thermal agitation i.e. Brownian motion becomes important [25].

Dissipation is another characteristic feature of granular materials. Energy is lost due to inelasticity and friction when particles collide or slide past each other. Again this is different from ordinary liquids or gases where it is assumed that energy is conserved during collisions between atoms or molecules. Therefore granular materials are out of thermodynamical equilibrium and they quickly settle to metastable configurations when external energy input is stopped. Dissipation and the irrelevance of temperature are one of the reason why classical theories like thermodynamics and statistical mechanics have difficulties describing granular materials. Thermal fluctuations and conservation of energy in ordinary fluids and gases cause the molecules and atoms to explore phase space and smooth out irregularities.

Despite its simplicity and omnipresence the physics of granular matter is poorly understood. Its distinction from ordinary phases of matter has incited some authors to present it as a new state of matter on its own [53]. Below we will briefly touch upon some peculiarities of

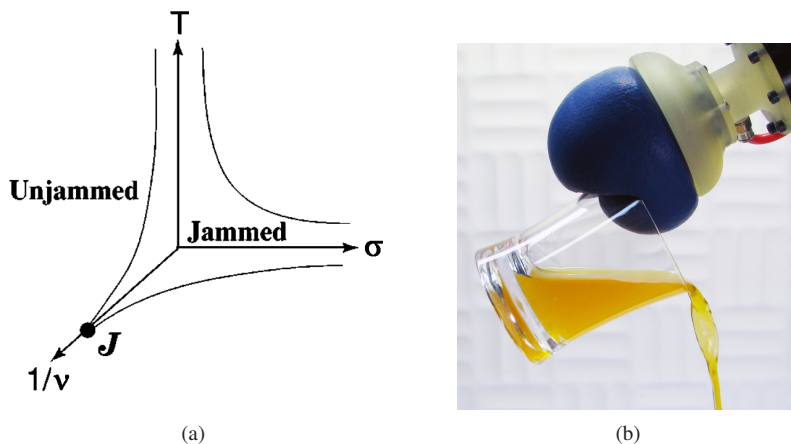


Figure 1.2: (a) The jamming phase diagram. (Adapted from [77] and [114]). (b) Robotic gripper based on jamming [12].

granular matter when it behaves like a solid, liquid or gas. For a comprehensive review we refer to [5, 25, 37, 53, 54] among others.

1.2 Jamming, force chains, granular crystals and sound propagation

When filling a container with granular matter we will notice that its density is variable. Initially the packing of grains is relatively loose and to open up room for more material one usually shakes the container. The variation in density comes from the friction between particles and randomness in the packing. As pointed out in the previous section, the absence of thermal fluctuations prevents the system to reach an equilibrium state with constant density. Consequently particles can rearrange in a multitude of metastable states depending on the initial conditions and history. Experiments have shown that the loosest packing of monodisperse spheres (commonly referred to as the random loose packing) has a filling fraction of $v_{rlp} \approx 0.56$ [115]. On the other hand, the volume fraction of the densest “random close packing” of hard spheres was repeatedly measured as $v_{rcp} \approx 0.64$ in experiments and simulations [8, 15, 27, 113] even though there is a debate about the definition of the random close packing [114, 136] due to the ambiguous meaning of random. Finally the maximum density is achieved when equal size spheres are placed on a regular lattice such as hexagonal close pack (hcp) or face centered cubic (fcc). In this case the volume fraction is $v_{hcp} = v_{fcc} \approx 0.74$.

Sometimes granular matter stops flowing without any apparent reason, it is jammed. This

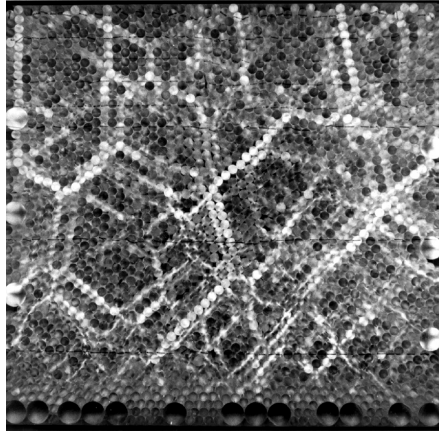


Figure 1.3: Force chains in a compression test with birefringent photoelastic disks.

can be a major problem in many practical situations such as flows from hoppers or transport of powders in conduits. Jamming is the general term used to describe the transition from a flowing state to a solid like state in disorder. It is manifested by dynamical arrest, an infinite increase of viscosity and emergence of mechanical stability with a finite resistance to external loading. In contrast to crystals, the origin of mechanical stability in amorphous solids is not well understood.

Jamming occurs in thermal as well as athermal systems such as glasses, colloids, foams or granular materials. The similarities between different systems has led Liu and Nagel to propose a jamming phase diagram [77] to unify various phenomena, see Fig. 1.2a. The diagram is represented by three control parameters, i.e. temperature T , inverse of volume fraction $1/v$ and shear stress σ which are on the axes, and the surface which separates the jammed phase from the unjammed state. As mentioned earlier the temperature axis is inapplicable for granular materials and other athermal systems and therefore the transition is solely controlled by the density and applied stress. In particular, the point J on the $1/v$ axis in Fig. 1.2a marks the transition in isotropically compressed frictionless systems with finite range repulsive potential [113, 114].

Jamming is usually an unwanted phenomenon, but recent studies have demonstrated its use in robotics [12, 105]. Figure 1.2b shows a gripper which holds objects by conforming an elastic shell filled with granular matter to their shape and jamming it by sucking out the air. Another similar but more familiar application is the vacuum mattress used to stabilize and carry injured persons.

A consequence of randomness in the grain positions is the disorder and amorphous structure of granular materials. This leads to the inhomogeneity in many quantities observed at the

particle scale. For example, force chains are subsets of the contact network formed by the particles which carry much larger forces than average. It is relatively easy to visualize them in computer simulations whereas in experiments photoelastic materials with polarized light are typically used, see Fig. 1.3. Depending on the nature of external loading force networks show strong directional anisotropy. Majmudar and Behringer [93] reported that when shear deformation is applied to an assembly of photoelastic disks, contact forces align along the direction of shear. In case of isotropic compression a 6-fold symmetry is observed in the angular distribution [93]. In general forces align in the direction of the major principal stress [135].

Like many macroscopic properties, sound propagation in granular materials depends on their amorphous disordered structure. In continuum theories, sound speed can be directly extracted from macroscopic elastic constants i.e. shear and bulk moduli. However this approach relies on the separation of scales and discards the heterogeneity and discreteness at the microscale. On the other hand, it is widely recognized that in granular materials there is not a clear separation between scales as the system size may be comparable to the grain size. For small systems a tiny disorder at particle scale may have a huge consequence on sound propagation [78, 103]. Figure 1.4 illustrates the effect of only 0.2 % size variation on stress propagation in an ordered packing of particles. Only low frequency signals can propagate in the presence of disorder. The magnitude of disorder seems small relative to the particle size, however, it is comparable to the more relevant length scale, namely contact deformation.

Recent studies investigated the role of force chains in sound propagation. It was first noted in simulations that the coherent wave front advances independent of the force chains [129]. However, later experiments with photoelastic disks indicated that the wave amplitude is larger in particles along the force chains [116]. Finally, based on the experimental observation that there is a reproducible coherent wave it was suggested that an effective medium theory could describe sound propagation in granular media [60]. The observation of a reproducible coherent wave in experiments was interpreted as a sign that irregularities at the microscale are smoothed out and an effective medium theory could describe sound propagation in granular media in the long wave length limit [60]. However, available models (e.g. [139]) fail to estimate correctly the shear and bulk moduli especially at low pressures due to the assumption of affine deformation [94].

In contrast to the disorder of natural granular materials, highly uniform particles can be placed on a lattice to build artificial granular crystals. Perhaps, the simplest example is the linear chain of particles which has been studied extensively for its non-linear dynamics. It was first predicted theoretically that this system can sustain solitary waves [110] which were later observed experimentally [16, 74]. An application of this type of structure is in shock absorbers where energy is spread through the chain in time and space [21, 29]. Furthermore, the ability to control the non-linearity of the interactions between particles with pre-compression allows to tune the frequency of propagating waves. This property was exploited

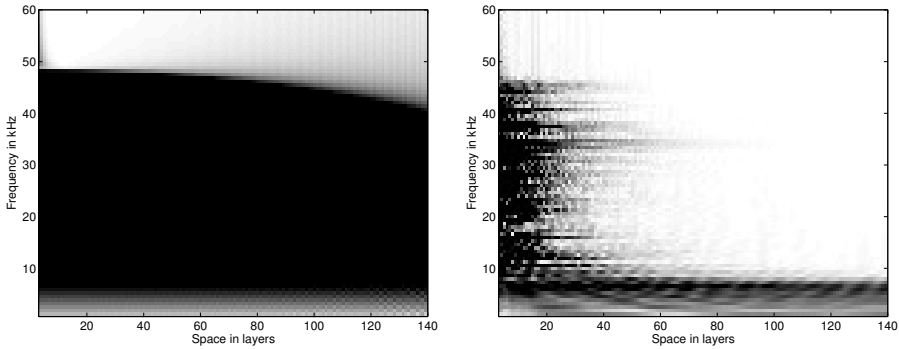


Figure 1.4: Effect of size disorder on sound propagation in a face centered cubic structure. Amplitude of Fourier coefficients of the propagating stress signal as function of the distance from the source. Left: No disorder. Right: 0.2% disorder. After [103].

to focus sound with acoustic lenses and design tunable phononic crystals [10, 130].

1.3 Shear bands, dilatancy, constitutive laws and patterns

Granular materials can flow like a liquid. One of the most familiar example is the granulated sugar we pour into our coffee or tea. However granular flows are not restricted to daily life routines. Many industries such as agriculture, food and energy rely on them for processing and transport of raw materials. On a much larger scale they play an important role in geophysical phenomena such as landslides, avalanches or earth quakes. Below we discuss some particularities of granular flows distinguishing them from those of classical fluids.

In contrast to ordinary fluids shearing a dense granular material does not induce a linear velocity profile, instead deformation is localized in thin shear bands of five to ten grain diameters [106, 138]. Shear bands have been studied extensively in geomechanics because of their role in natural hazards such as earth quakes or landslides [26]. From a continuum mechanics point of view, it was shown that localization can result from an instability of the constitutive model [123]. However, capturing the width of the shear bands with continuum models has been problematic due to the lack of a microscopic length scale which reflects the microstructure. As a result, gradient enhanced [36] and micropolar Cosserat [24] type constitutive models have been proposed. Recent studies have demonstrated that shear bands of arbitrary width can be achieved in split bottom Couette cell geometries [13, 35, 82]. This allows a more detailed study of the velocity profile and microstructure within the shear band.

Shear deformation of granular materials is accompanied with positive volume change. This phenomenon was first observed about one century ago by Reynolds who named it dilatancy

[120]. He illustrated it by showing that to distort a crystal of rigid particles the volume must increase. Physically dilatancy can be explained with the fact that two layers of interlocking grains have to separate first before they can slide past each other. This principle was generalized to disordered systems and is implemented in many constitutive models for granular media for quasi-static deformation or dense flows [63, 98].

Analyzing the behavior of granular materials by tracking the motion of particles is unfeasible for most applications. The huge number of particles in real size problems prohibits practical results even with the most advanced numerical methods and computer hardware. Instead a continuum approach is usually adopted. Then the problem consists of solving a set of partial differential equations given by the conservation of mass, momentum and energy supplemented with boundary conditions and constitutive equations which characterize the behavior of the material under consideration. This works well for classical fluids or solids because there is separation of scales i.e. the macroscopic scale is much larger than the scale of atoms or molecules composing the liquid or solid. However as discussed before this assumption may not hold for granular media. Furthermore, dissipation and the absence of thermal fluctuations prevents the development of a single constitutive model capable of describing all features of granular materials. As a result, granular flows are generally studied in three categories [5, 37, 39, 51, 53]:

1. Slow quasi-static deformation of dense systems
2. Dense but a liquid like behavior where inertia effects cannot be neglected
3. A dilute state where particles interact mainly with binary collisions.

In the following we briefly summarize main features of the flows in these regimes and the constitutive models employed to describe them.

Slowly deforming quasi-static dense granular materials are characterized by long lasting contacts and rate independent behavior [100]. A prominent example of this category is the soil which is probably the most abundant and the most studied granular material on earth. The study of mechanical properties of soil goes back to Coulomb who introduced the first yield criterion [17]. There the condition for failure is given by the coefficient of friction which limits the ratio of shear and normal stresses. The tangent of the angle of repose of static piles is usually measured as the internal coefficient of friction. When the stress ratio equals or exceeds it the material starts to deform plastically. The majority of the constitutive models for dense granular materials are based on the theory of plasticity in combination with the assumption of coaxiality of the stress and strain tensors [50]. The direction of the plastic strains are determined by the flow rule which is perpendicular to the yield surface if it is associated. The first of these models was proposed by Drucker and Prager [30] who used the Mohr-Coulomb yield criterion to derive the flow rule [50]. Later these models

were improved by including work hardening and softening and non-associated flow rules [125]. Other models relaxed the condition of coaxiality by adopting alternative kinematic assumptions [3, 98]. A different approach to the modelling of rate independent behavior of dense granular materials is given by hypoplasticity [66]. Here the relation between stress and strain rates is defined by a non-linear equation that automatically produces an inelastic strain-stress curve without the need to decompose the strain tensor to elastic and plastic parts. Another advantage of hypoplastic constitutive models over classical plastic theories is its simpler formulation which does not require a yield surface or flow rule. For an overview of constitutive models for the plastic deformation of dense granular materials we refer to [50].

When the shear rate is increased the grains flow similar to an ordinary liquid. There is still a dense contact network but grain inertia cannot be neglected anymore [37, 51, 100]. Dimensional analysis has shown that [19] the relative contributions of inertia and confining pressure P can be expressed with a single dimensionless inertia number $I = \dot{\gamma}d/\sqrt{P/\rho}$ where $\dot{\gamma}$, d and ρ are the macroscopic shear rate, grain diameter and density respectively. This is interpreted as the ratio of two time scales: the macroscopic time to displace a layer of particles imposed by the shear rate and a microscopic time scale of particle rearrangements controlled by the pressure [100]. Several experimental and numerical results in various geometries indicate that the effective coefficient of friction and volume fraction have a functional dependence on the inertia number I [37]. As a result, constitutive relations have been proposed by Jop *et al.* based on the local rheology assumption [62]. The generalization of this model to three-dimensions gave good quantitative agreement with experiments in the inclined rough plane geometry [63]. We refer to [37] for a review and [100] for a detailed comparison of several experiments and simulations of dense granular flows.

In the limit of low density and strong agitation particles detach from the contact network and interact mainly with binary collisions. This behavior is analogous to molecular gases and as a result these systems have been denominated as granular gases [39]. Theoretical modeling is naturally inspired by the kinetic theory of ideal gases which was extended to include the inelasticity of contacts. This topic goes beyond the scope of this thesis, however, we refer to the review of Goldhirsch [39] for the interested reader. Nevertheless, we will briefly mention some phenomena observed in granular gases. Inelastic collapse happens in a many particle system when an infinite number of contacts occur in a finite time, in a way similar to a ball bouncing on the floor. It is manifested by string like structures and can be a source of problem in event driven molecular dynamics simulations. Inelastic collapse can lead to high density regions i.e. clusters. The rate of dissipation in these regions is higher than in the surrounding which causes neighboring particles to migrate to them thereby growing clusters.

Clustering is an example of pattern formation in granular systems. In a review on this subject Aranson and Tsimring define pattern formation as “*a dynamical process leading to the spontaneous emergence of a nontrivial spatially nonuniform structure which is weakly de-*

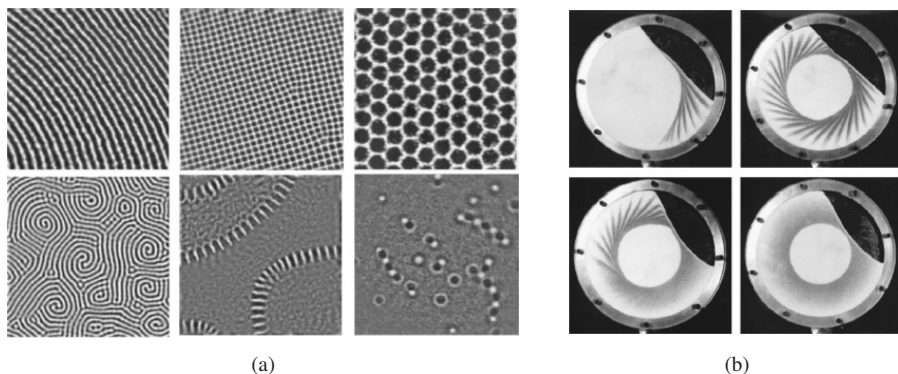


Figure 1.5: (a) Patterns in vertically vibrated granular layers, after [5] . (b) Segregation in rotating drums, after [46].

pendent on initial and boundary conditions” [5]. Patterns are observed in various setups and geometries. Vertically vibrated layers of a few dozens of particle diameter thick show surprising patterns of standing waves oscillating at half of the driving frequency. Depending on the acceleration and the driving frequency of the container stripes, squares, hexagons and ocellons are observed (Fig. 1.5a). Another famous phenomenon in vertically vibrated polydisperse assemblies known as the Brazil-nut effect is the segregation of large particles near the top. This is counter intuitive as the classical entropy arguments would require that vibration favors mixing [53]. Segregation also occurs in chute flows or rotating drums (Fig. 1.5b). Other examples of nontrivial patterns in granular materials are fingering and avalanches in chute flows and dunes. Several theoretical models have been proposed to describe these phenomena, we refer to [5] for a detailed account.

1.4 Scope and outline

This thesis relates to the quasi-static behavior of dense granular materials. We study using discrete particle simulations the deformation and mechanical response of idealized polydisperse assemblies of spheres or disks. In particular, the constitutive behavior of disordered packings and pattern transformation in crystal structures are considered. Accordingly, the thesis can be split in two parts:

1. The effect of particle properties on the macroscopic stress-strain relation are investigated in Chapters 3 and 4
2. Pattern transformations in two-dimensional regular arrays of soft and hard particles are studied in Chapters 5 and 6

Below we outline the contents of the chapters.

In Chapter 2 we introduce the discrete element method which is the main numerical tool used throughout the thesis. The Verlet integration and the basic algorithm of the method are described. We then elaborate the formalism used to obtain averaged quantities such as stress or fabric. In the last part of this chapter we analyze the terms in a hypoplastic constitutive model in order to determine their role in the material response.

In Chapter 3, the isotropic deformation of frictionless packings are studied. The effect of the system size, history, deformation rate and polydispersity on the evolution of the average number of contacts i.e. coordination number is investigated. A correction factor for the contact density in terms of the moments of the size distribution is computed. Finally an expression for the average pressure and effective bulk modulus taking the contact network into account is derived and results are compared with simulations.

The effect of particle friction and the behavior under anisotropic loading are studied in Chapter 4. We test the validity of the model for pressure developed in the previous chapter for isotropically compressed frictional packings and confirm that it is also applicable in this case. Triaxial test simulations are performed to characterize the effect of friction and polydispersity on the macroscopic stress-strain response to anisotropic loading. Furthermore, the hypoplastic model introduced in Chapter 2 is calibrated with the simulation results to understand the relation between model parameters and particle friction and polydispersity.

In Chapter 5 we study the pattern transformation in two-dimensional regular arrays i.e. granular crystals composed of soft silicone rubber and polytetrafluoroethylene particles. We show with experiments and simulations that under uniaxial compression the system transforms from an initial square lattice arrangement to an hexagonal structure. The transformation is smooth, homogeneous and quasi-reversible for sufficiently small size ratios of particles.

Chapter 6 investigates the phononic properties of the previously studied granular crystal. We compute the band structure of the crystal at different levels of deformation and show that band gaps open and close with pattern transformation. Finally, the effect of material properties and tangential contact forces on the phononic properties is analyzed and the possible application of the crystal as a tunable phononic crystal is discussed.

Chapter 2

Discrete and continuous models of granular materials

Abstract

The discrete element method which allows to simulate the motion of a large number of interacting particles is the main numerical tool used in this thesis. We briefly summarize the principle of the method and give the details of the contact force model used in the next chapters. Numerical integration of the equations of motion and the formalism to obtain averaged quantities from the simulation results are also discussed. In the last section of this chapter, we analyze analytically the terms of an hypoplastic constitutive model assuming a two-dimensional bi-axial geometry. The relation of the material coefficients of the model to the bulk and shear moduli and anisotropy are discussed.

2.1 The Discrete Element Method

The discrete element method (DEM) has been introduced by Cundall & Strack for problems in geotechnical engineering [18]. Since then it has been adopted as an analysis tool in many fields dealing with granular matter such as process and pharmaceutical industries. DEM which is sometimes also called soft particle Molecular Dynamics is closely related to Molecular Dynamics (MD). The principle of both methods can be summarized as finding the trajectories of particles obeying principles of classical mechanics by solving Newton's equation of motion. However, as the name suggests MD is mainly used to study thermodynamic

properties of ensembles of atoms or molecules. DEM, on the other hand, is generally used to simulate the motion of macroscopic particles. Consequently in DEM the interactions between particles are usually dissipative whereas in MD the forces are conservative i.e. derived from a potential. Algorithm 1 illustrates the main steps of DEM and MD.

Algorithm 1 Discrete Element Method / Molecular Dynamics

Require: Initial positions and velocities, time end of simulation T

Initialize the time and particle positions, velocities and forces

while $t < T$ **do**

for all particles **do**

- Find contacts or interacting pairs
- Compute and add up forces

end for

for all particles **do**

- Integrate the equations of motion
- Update positions and velocities

end for

 Update system boundaries

$t = t + \Delta t$

end while

2.1.1 Contact forces

If particles are large enough long range interactions such as van der Waals forces are negligible. In this case particles interact only when they are in close contact. At this point they start deforming due to the forces exerted on to each other. In real granular materials particles have complicated shapes and their deformation and forces acting on them can be very complex. To reduce the computational cost, in DEM particles are typically modeled as spheres or disks and it is assumed that they are in contact when they overlap. Furthermore the contact forces are computed as a function of the overlap.

In the following, we study the normal collision of two spherical particles interacting with the linear spring-dashpot contact force model which is also used in the Chapters 3 and 4. The overlap of two particles with position vectors \mathbf{r}_i and \mathbf{r}_j is defined as follows (Fig.2.1):

$$\delta = \max(0, \frac{1}{2}(d_i - d_j) - (\mathbf{r}_i - \mathbf{r}_j) \cdot \mathbf{n}_{ij}) \quad (2.1)$$

where d_i and d_j are the diameters of the particles and \mathbf{n}_{ij} is the unit normal vector parallel to the line connecting their centers. The relative speed of the particles is:

$$\dot{\delta} = -\mathbf{v}_{ij} \cdot \mathbf{n}_{ij} \quad (2.2)$$

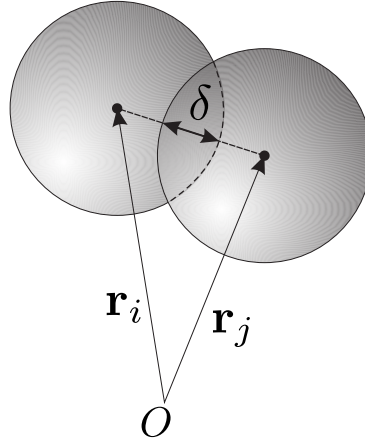


Figure 2.1: Schematic description of the overlap δ during a collision.

where $\mathbf{v}_{ij} = \mathbf{v}_i - \mathbf{v}_j$. The acceleration is found by taking the derivative of (2.2):

$$\ddot{\delta} = -(\mathbf{a}_i - \mathbf{a}_j) \cdot \mathbf{n}_{ij} = -(\mathbf{f}_i/m_i - \mathbf{f}_j/m_j) \cdot \mathbf{n}_{ij} = -\frac{1}{m_{ij}} \mathbf{f}_i \cdot \mathbf{n}_{ij} = -\frac{f_i}{m_{ij}} \quad (2.3)$$

where $m_{ij} = \frac{m_i m_j}{m_j + m_i}$ is the effective mass and $\mathbf{f}_i = -\mathbf{f}_j$ is the contact force acting on the particles. According to the spring-dashpot model:

$$f_i = -m_{ij} \ddot{\delta} = k\delta + \gamma \dot{\delta}. \quad (2.4)$$

where k is the linear spring constant and γ is the viscous damping coefficient. Rearranging this equation and using the following substitutions for the natural frequency $\omega_0 = \sqrt{k/m_{ij}}$ and the viscous dissipation $\eta = \frac{\gamma}{2m_{ij}}$, we obtain the ordinary differential equation of the harmonic oscillator

$$\omega_0^2 \delta + 2\eta \dot{\delta} + \ddot{\delta} = 0. \quad (2.5)$$

With the initial conditions $\delta(0) = 0$ and $\dot{\delta}(0) = v_0$, the solution is given as:

$$\delta(t) = \frac{v_0}{\omega} e^{-\eta t} \sin(\omega t) \quad (2.6)$$

where $\omega = \sqrt{\omega_0^2 - \eta^2}$ is the oscillation frequency of the damped system.

The duration of a contact can be defined in two ways. The first criterion is expressed by $\delta(t_c^\delta) = 0$. Then t_c corresponds to the half-period of the oscillator.

$$t_c^\delta = \pi/\omega \quad (2.7)$$

Another way is to assume that the contact ends when the force is zero i.e. $f(t_c^f) = 0$. Then t_c^f can be obtained by substituting (2.6) and its derivative in (2.4):

$$t_c^f = \frac{1}{\omega} \left(\pi - \arctan \frac{2\eta\omega}{\omega^2 - \eta^2} \right) \quad (2.8)$$

Finally, using one of the t_c described above we can obtain the restitution coefficient with $r = -\frac{v(t_c)}{v_0}$. For t_c^δ , this gives $r = \exp(-\eta t_c^\delta)$. The contact duration and the coefficient of restitution for the bouncing of a particle on a wall can be computed following the same procedure and assuming $m_{wall} = \infty$.

Linear elastic and viscous tangential contact forces are modeled in a similar way

$$\mathbf{f}^t = -k^t \delta^t - \gamma^t \mathbf{v}_{ij}^t \quad (2.9)$$

with the spring stiffness k^t , viscous dissipation γ^t and tangential displacement δ^t and the tangential velocity at contact

$$\mathbf{v}_{ij}^t = \mathbf{v}_{ij} - (\mathbf{v}_{ij} \cdot \mathbf{n}_{ij}) \mathbf{n}_{ij} - \Omega_i \times \mathbf{l}_{ij} + \Omega_j \times \mathbf{l}_{ji} \quad (2.10)$$

where Ω_j is the angular velocity of particle i and $\mathbf{l}_{ij} = -((d_i - \delta)/2) \mathbf{n}_{ij}$ is the branch vector from the center of particle i to the contact point. The tangential spring length is calculated by integrating :

$$\frac{d\delta^t}{dt} = \mathbf{v}_{ij}^t - \frac{(\delta^t \cdot \mathbf{n}_{ij}) \mathbf{n}_{ij}}{|\mathbf{r}_i - \mathbf{r}_j|} \quad (2.11)$$

starting from the time of contact. The second term of (2.11) is needed to rotate the spring so that it is always perpendicular to the contact normal \mathbf{n}_{ij} .

Contact friction is described by the Coulomb friction model where μ is the coefficient of friction which limits the tangential contact forces such that $|\mathbf{f}^t| \leq \mu |\mathbf{f}^n|$ with \mathbf{f}^n the normal contact force. Particles slide past each other if $|\mathbf{f}^t| = \mu |\mathbf{f}^n|$ and are stuck otherwise. If $|\mathbf{f}^t| > \mu |\mathbf{f}^n|$ the tangential displacement is adjusted to satisfy Coulomb criterion.

For more complex contact models including, rolling, torsion, adhesion and elasto-plasticity we refer to [85].

2.1.2 Numerical integration

After force calculation, the next step of DEM is the integration of the equations of motion:

$$m_i \mathbf{a}_i = \mathbf{f}_i \quad \text{and} \quad I_i \frac{d\Omega_i}{dt} = \mathbf{q}_i \quad (2.12)$$

where I_i is the moment of inertia and \mathbf{f}_i and \mathbf{q}_i are the total force and torque acting on the particle, respectively. There are a few popular numerical integration schemes used for this purpose. We present here the Verlet and Velocity-Verlet algorithm which is also implemented in the code we have been using.

Verlet algorithm

The main advantages of the Verlet algorithm [2] are its simplicity, numerical stability and energy preserving properties. It can be derived by taking the Taylor series approximation of the position vector $\mathbf{r}(t)$ in the neighborhood of t around Δt and $-\Delta t$:

$$\mathbf{r}(t + \Delta t) = \mathbf{r}(t) + \mathbf{v}(t)\Delta t + \frac{\mathbf{a}(t)\Delta t^2}{2} + \frac{\mathbf{b}(t)\Delta t^3}{6} + O(\Delta t^4)$$

$$\mathbf{r}(t - \Delta t) = \mathbf{r}(t) - \mathbf{v}(t)\Delta t + \frac{\mathbf{a}(t)\Delta t^2}{2} - \frac{\mathbf{b}(t)\Delta t^3}{6} + O(\Delta t^4)$$

where \mathbf{b} is the third derivative of the position with respect to the time. Adding these two expressions we get:

$$\mathbf{r}(t + \Delta t) = 2\mathbf{r}(t) - \mathbf{r}(t - \Delta t) + \mathbf{a}(t)\Delta t^2 + O(\Delta t^4).$$

The position of the particles at $t + \Delta t$ can be computed using this expression. The acceleration is deduced from the force using Newton's second principle. As it is seen from the above equation the local error of the Verlet algorithm is $O(\Delta t^4)$. It is possible to demonstrate by induction that the global error is $O(\Delta t^2)$. In this version of the algorithm velocities are not given explicitly and must be calculated using the positions:

$$\mathbf{v}(t) = \frac{\mathbf{r}(t + \Delta t) - \mathbf{r}(t - \Delta t)}{2\Delta t} + O(\Delta t^2).$$

However this is not possible for velocity dependent viscous forces where the velocities must be known before computing the positions.

The Velocity Verlet

Algorithm 2 Velocity Verlet

Require: Forces \mathbf{f}_i , positions \mathbf{r}_i and velocities \mathbf{v}_i from the previous time step

for particles $i \leftarrow 1, N$ **do**

$$\mathbf{r}_i \leftarrow \mathbf{r}_i + \mathbf{v}_i\Delta t + \frac{1}{2}\mathbf{a}_i(\Delta t)^2$$

$$\mathbf{v}_i \leftarrow \mathbf{v}_i + \mathbf{a}_i \frac{\Delta t}{2}$$

$$\mathbf{a}_i \leftarrow \frac{\mathbf{f}_i}{m_i}$$

$$\mathbf{v}_i \leftarrow \mathbf{v}_i + \mathbf{a}_i \frac{\Delta t}{2}$$

end for

This is a slight modification of the original Verlet algorithm which accounts for the velocities explicitly. After having solved the first time step with the basic Verlet the scheme in Algorithm 2 is applied for translations. The accuracy of the velocity Verlet is of the same order as the basic Verlet. The velocity Verlet is necessary when velocity dependent forces are present. Also, notice that the time step for \mathbf{v} is half of the usual.

2.2 Micro-Macro transition: Averaging procedures

DEM allows a very detailed description of granular materials including contact forces and exact position of the particles. However, the amount of data generated during a DEM simulation is huge. In order to compare it to macroscopic experiments or theories, smoothing and averaging are necessary. In this section we present the averaging procedures used to obtain macroscopic tensorial quantities such as the fabric tensor and the stress for granular materials which are computed in the next chapters.

2.2.1 Averaging formalism

The general rule to obtain any average quantity Q in volume V is defined as follows [73]:

$$Q = \frac{1}{V} \sum_{p \in V} w_V^p V^p Q^p \quad (2.13)$$

where V^p is the volume of the particle and w_V^p is the weight of its contribution to the average and Q^p is the pre-averaged particle quantity

$$Q^p = \sum_{c=1}^{C^p} Q^c \quad (2.14)$$

with Q^c the local quantity at the contact and C^p the number of contacts of the particle. The simplest example of averaging is the solid volume fraction of a particle assembly obtained when $Q^p = 1$:

$$v = \frac{1}{V} \sum_{p \in V} w_V^p V^p. \quad (2.15)$$

From this the average density can be easily computed by assigning the weight to the particle densities $w_V^p = \rho_p$.

2.2.2 Fabric Tensor

The fabric is a tensorial quantity which is used to characterize the internal structure of an assembly of grains. For a single particle its definition is given as [38, 73]:

$$\mathbf{F}^p = \sum_{c=1}^{C^p} \mathbf{n}^c \otimes \mathbf{n}^c \quad (2.16)$$

where \mathbf{n}^c is the unit vector pointing outwards in the direction of the contact. An equivalent definition is given in terms of the branch vectors connecting the center of the particle to the

contact points:

$$\mathbf{F}^p = \frac{1}{a^2} \sum_{c=1}^{C^p} \mathbf{l}^{pc} \otimes \mathbf{l}^{pc} \quad (2.17)$$

where a is the particle radius assuming that it is spherical. The average fabric is computed using Eq. (2.13):

$$\mathbf{F} = \langle \mathbf{F}^p \rangle = \frac{1}{V} \sum_{p \in V} w_V^p V^p \sum_{c=1}^{C^p} \mathbf{n}^c \otimes \mathbf{n}^c \quad (2.18)$$

Note that $\text{tr}(\mathbf{F}^p)$ is equal to C^p the number of contacts of the particle. In a regular lattice arrangement assuming that $w_V^p = 1 \forall p$, $\text{tr}(\mathbf{F})$ is exactly equal to Cv i.e. the coordination number times the volume fraction.

2.2.3 Stress

The average stress of a body inside a volume V is defined by[71]:

$$\bar{\boldsymbol{\sigma}} = \frac{1}{V} \int_V \boldsymbol{\sigma} dV \quad (2.19)$$

Using the static equilibrium condition $\text{div } \boldsymbol{\sigma} = 0$ and the divergence theorem it can be shown that:

$$\bar{\boldsymbol{\sigma}} = \frac{1}{V} \int_{\partial V} (\mathbf{x} \otimes \boldsymbol{\sigma}) \cdot \mathbf{n} dV \quad (2.20)$$

where \mathbf{x} is the position vector and \mathbf{n} is the outward normal vector. Therefore the average stress inside a particle which is in contact with other particles can be expressed as:

$$\boldsymbol{\sigma}^p = \frac{1}{V^p} \sum_{c=1}^{C^p} \mathbf{l}^{pc} \otimes \mathbf{f}^c \quad (2.21)$$

here we have assumed that the contact forces \mathbf{f}^c are equal to point loads such that $\boldsymbol{\sigma}^c \cdot \mathbf{n} = \mathbf{f}^c$ where $\boldsymbol{\sigma}^c$ is the stress tensor at the contact point. Now following the formalism expressed in Eq. (2.13), the average stress tensor in a particle assembly can be written as:

$$\boldsymbol{\sigma} = \langle \boldsymbol{\sigma}^p \rangle = \frac{1}{V} \sum_{p \in V} w_V^p \sum_{c=1}^{C^p} \mathbf{l}^{pc} \otimes \mathbf{f}^c \quad (2.22)$$

If the weights w_V^p are ignored, the average stress can also be expressed as a sum over all contacts inside the assembly [71]. Since $\mathbf{f}^c = \mathbf{f}^{pq} = -\mathbf{f}^{qp}$ where \mathbf{f}^{pq} and \mathbf{f}^{qp} are the forces exerted by particles q and p on to each other respectively; it is possible to write:

$$\boldsymbol{\sigma} = \frac{1}{V} \sum_{c \in V} \mathbf{l}^c \otimes \mathbf{f}^c. \quad (2.23)$$

2.3 Analysis of the components of a hypoplastic constitutive model

As mentioned in §1.3 of the previous chapter, several constitutive models within the framework of continuum mechanics have been developed to describe the mechanical behavior of granular materials. In this section we focus on a variant of a hypoplastic constitutive model proposed by Wu et al. [141]. More precisely, in a two-dimensional bi-axial geometry we investigate the relation of the material coefficients of the model to the classical elastic moduli such as the shear and bulk modulus, and anisotropy as introduced in a recent work by Luding and Perdahcioglu [87].

Before giving the specific form of the equation let us summarize the basic properties of hypoplasticity following [66, 141, 142]. A hypoplastic constitutive model relates the rate of the stress $\dot{\mathbf{T}}$ to the stress \mathbf{T} and rate of deformation \mathbf{D} (i.e. symmetric part of the velocity gradient):

$$\dot{\mathbf{T}} = \mathbf{H}(\mathbf{T}, \mathbf{D}) \quad (2.24)$$

where the co-rotational Jaumann rate of stress is given by $\dot{\mathbf{T}} = \dot{\mathbf{T}} - \mathbf{W}\mathbf{T} + \mathbf{T}\mathbf{W}$ with \mathbf{W} the skew-symmetric part of the velocity gradient. To ensure rate independence the stress rate must be homogeneous of the first degree in \mathbf{D}

$$\mathbf{H}(\mathbf{T}, \lambda \mathbf{D}) = \lambda \mathbf{H}(\mathbf{T}, \mathbf{D}). \quad (2.25)$$

Objectivity with respect to rigid body rotations is satisfied by the following condition:

$$\mathbf{H}(\mathbf{Q}\mathbf{T}\mathbf{Q}^T, \mathbf{Q}\mathbf{D}\mathbf{Q}^T) = \mathbf{Q}\mathbf{H}(\mathbf{T}, \mathbf{D})\mathbf{Q}^T \quad (2.26)$$

where \mathbf{Q} is an orthogonal rotation matrix. Furthermore, it is required that (2.24) is homogeneous in \mathbf{T} :

$$\mathbf{H}(\lambda^n \mathbf{T}, \mathbf{D}) = \lambda^n \mathbf{H}(\mathbf{T}, \mathbf{D}) \quad (2.27)$$

so that proportional stress paths lead to proportional strain paths and vice versa [141, 142]. More details about these restrictions and general properties of hypoplasticity can be found in aforementioned references.

The specific form of the constitutive equation (2.24) studied here is given by [141]:

$$\dot{\mathbf{T}} = K_1 (\text{tr } \mathbf{T}) \mathbf{D} + K_2 \frac{\text{tr}(\mathbf{T}\mathbf{D})}{\text{tr } \mathbf{T}} \mathbf{T} + K_3 \frac{\mathbf{T}^2}{\text{tr } \mathbf{T}} \sqrt{\text{tr } \mathbf{D}^2} + K_4 \frac{\mathbf{T}^{*2}}{\text{tr } \mathbf{T}} \sqrt{\text{tr } \mathbf{D}^2} \quad (2.28)$$

where K_1, K_2, K_3 and K_4 are dimensionless material coefficients and \mathbf{T}^* is the deviatoric part of stress. Note that the first two terms are linear in \mathbf{D} while the last two are non-linear.

2.3.1 Decomposition into volumetric and deviatoric parts

A second order tensor in \mathcal{D} dimensions can be split into a volumetric (i.e. isotropic) and a deviatoric part:

$$\mathbf{M} = m_v \mathbf{I} + \mathbf{M}^* \quad (2.29)$$

where the scalar $m_v = \frac{1}{\mathcal{D}} \text{tr}(\mathbf{M})$. This means that the deviatoric part of \mathbf{M} is traceless i.e. $\text{tr}(\mathbf{M}^*) = 0$ or equivalently $\sum_{i=1}^{\mathcal{D}} m_i^* = 0$ where m_i^* are the principal components. Our goal is to express the deviatoric part \mathbf{M}^* as a product of a scalar and a tensor similar to its volumetric part. This requires additional constraints on the eigenvalues of \mathbf{M} . For example in 3D if

$$m_2^* = 0 \quad (2.30)$$

the deviatoric part can be expressed as:

$$\mathbf{M}^* = m_d \mathbf{I}^*(\phi), \quad \text{such that} \quad m_d = \max(m_1^*, m_3^*) \geq 0 \quad (2.31)$$

and $\mathbf{I}^*(\phi) = \mathbf{Q}(\phi) \mathbf{I}^* \mathbf{Q}^T(\phi)$. The unit deviator and the rotation matrix are given by

$$\mathbf{I}^* = \begin{bmatrix} 1 & 0 & 0 \\ 0 & 0 & 0 \\ 0 & 0 & -1 \end{bmatrix} \quad \text{or} \quad \mathbf{I}^* = \begin{bmatrix} -1 & 0 & 0 \\ 0 & 0 & 0 \\ 0 & 0 & 1 \end{bmatrix} \quad \text{and} \quad \mathbf{Q}(\phi) = \begin{bmatrix} \cos \phi & 0 & \sin \phi \\ 0 & 1 & 0 \\ -\sin \phi & 0 & \cos \phi \end{bmatrix},$$

respectively. In general, without (2.30) or similar conditions, it is not possible to express \mathbf{M}^* as a product of a scalar and a tensor because, e.g. in 3D, two of its invariants are independent ($m_2^* = 0$ sets $\det(\mathbf{M}^*) = 0$). However, in 2D the unit deviator and the rotation matrix are simplified by removing the second rows and columns and only one invariant is independent. Consequently, the relation (2.31) is unambiguous up to the sign convention or the ordering of the eigenvalues of \mathbf{M}^* .

2.3.2 Analysis of the linear part

In the following, for simplicity we consider a 2D bi-axial system (i.e. $\mathcal{D} = 2$) corresponding to a plane stress or strain condition, and assume that the stress and strain rates can be decomposed according to Eqs. (2.29) and (2.31):

$$\mathbf{T} = p \mathbf{I} + \sigma_d \mathbf{I}^*(\phi_T) \quad (2.32)$$

$$\mathbf{D} = \dot{\epsilon}_v \mathbf{I} + \dot{\epsilon}_d \mathbf{I}^*(\phi_D) \quad (2.33)$$

Furthermore, we denote $\mathbf{I}^*(\phi_T)$ and $\mathbf{I}^*(\phi_D)$ simply by \mathbf{I}_T^* and \mathbf{I}_D^* respectively, assuming that the angles of rotation ϕ_T and ϕ_D are known. Note that, stress and strain rate tensors are colinear in the bi-axial geometry, however $\phi_T \neq \phi_D$ in general.

The first two terms of Eq. (2.28) express the elastic part of the hypoplastic constitutive and are linear in \mathbf{D} . Using Eqs. (2.32) and (2.33) the first term is given by:

$$K_1(\text{tr}\mathbf{T})\mathbf{D} = 2K_1p(\dot{\epsilon}_v\mathbf{I} + \dot{\epsilon}_d\mathbf{I}_D^*), \quad (2.34)$$

which shows its linear dependence on the pressure and deformation rate.

Similarly after substitution of Eqs. (2.32) and (2.33) the second term is given by:

$$\begin{aligned} K_2 \frac{\text{tr}(\mathbf{TD})}{\text{tr}(\mathbf{T})} \mathbf{T} &= K_2 \frac{\text{tr}([p\mathbf{I} + \sigma_d\mathbf{I}_T^*][\dot{\epsilon}_v\mathbf{I} + \dot{\epsilon}_d\mathbf{I}_D^*])}{\text{tr}(\mathbf{T})} (p\mathbf{I} + \sigma_d\mathbf{I}_T^*) \\ &= K_2 \frac{\text{tr}(p\dot{\epsilon}_v\mathbf{I} + \sigma_d\dot{\epsilon}_v\mathbf{I}_T^* + p\dot{\epsilon}_d\mathbf{I}_D^* + \sigma_d\dot{\epsilon}_d\mathbf{I}_T^*\mathbf{I}_D^*)}{2p} (p\mathbf{I} + \sigma_d\mathbf{I}_T^*) \\ &= K_2 \frac{2p\dot{\epsilon}_v + \sigma_d\dot{\epsilon}_d \text{tr}(\mathbf{I}_T^*\mathbf{I}_D^*)}{2p} (p\mathbf{I} + \sigma_d\mathbf{I}_T^*) \\ &= K_2 \left\{ p \left[\dot{\epsilon}_v + \frac{\sigma_d}{2p} \dot{\epsilon}_d \text{tr}(\mathbf{I}_T^*\mathbf{I}_D^*) \right] \mathbf{I} \right. \\ &\quad \left. + p \left[\frac{\sigma_d}{p} \dot{\epsilon}_v + \frac{\dot{\epsilon}_d}{2} \left(\frac{\sigma_d}{p} \right)^2 \text{tr}(\mathbf{I}_T^*\mathbf{I}_D^*) \right] \mathbf{I}_T^* \right\}. \end{aligned}$$

Using the identity $\text{tr}(\mathbf{I}_T^*\mathbf{I}_D^*) = 2\cos(2\phi_T - 2\phi_D)$ and denoting $s_d = \sigma_d/p$ as the deviatoric stress ratio the second term is reduced to

$$\begin{aligned} K_2 \frac{\text{tr}(\mathbf{TD})}{\text{tr}(\mathbf{T})} \mathbf{T} &= K_2 \left\{ p [\dot{\epsilon}_v + \dot{\epsilon}_d s_d \cos(2\phi_T - 2\phi_D)] \mathbf{I} \right. \\ &\quad \left. + p [\dot{\epsilon}_v s_d + \dot{\epsilon}_d s_d^2 \cos(2\phi_T - 2\phi_D)] \mathbf{I}_T^* \right\}. \end{aligned} \quad (2.35)$$

Now we focus on the contribution of the first two terms in the hypoplastic constitutive model by plugging back Eqs. (2.34) and (2.35) in Eq. (2.28) and neglecting the non-linear terms:

$$\begin{aligned} \dot{\mathbf{T}}_{1,2} &= 2K_1p(\dot{\epsilon}_v\mathbf{I} + \dot{\epsilon}_d\mathbf{I}_D^*) \\ &\quad + K_2 \left\{ p [\dot{\epsilon}_v + \dot{\epsilon}_d s_d \cos(2\phi_T - 2\phi_D)] \mathbf{I} \right. \\ &\quad \left. + p [\dot{\epsilon}_v s_d + \dot{\epsilon}_d s_d^2 \cos(2\phi_T - 2\phi_D)] \mathbf{I}_T^* \right\} \end{aligned} \quad (2.36)$$

where $\dot{\mathbf{T}} = \dot{\mathbf{T}}$ since $\mathbf{W} = 0$ in the biaxial box.

The rate of pressure change due to the linear terms can be computed by taking the trace of Eq. (2.36):

$$\begin{aligned} \dot{p}_{1,2} &= \frac{1}{2} \text{tr}(\dot{\mathbf{T}}_{1,2}) \\ &= 2K_1p\dot{\epsilon}_v + K_2p[\dot{\epsilon}_v + s_d\dot{\epsilon}_d \cos(2\phi_T - 2\phi_D)] \\ &= (2K_1 + K_2)p\dot{\epsilon}_v + K_2ps_d\dot{\epsilon}_d \cos(2\phi_T - 2\phi_D) \end{aligned} \quad (2.37)$$

since the traces of the unit deviators vanish.

The deviatoric part of the stress rate is:

$$\dot{\mathbf{T}}_{1,2}^* = \dot{\mathbf{T}}_{1,2} - \dot{p}_{1,2} \mathbf{I}$$

that after plugging in Eqs. (2.36) and (2.37) and grouping under common factors leads to:

$$\dot{\mathbf{T}}_{1,2}^* = 2K_1 p \dot{\epsilon}_d \mathbf{I}_D^* + K_2 p [\dot{\epsilon}_v s_d + \dot{\epsilon}_d s_d^2 \cos(2\phi_T - 2\phi_D)] \mathbf{I}_T^*. \quad (2.38)$$

The meanings of material coefficients K_1 and K_2 become clear if pure isotropic deformation ($\dot{\epsilon}_d = 0$) is applied:

$$\dot{p}_{1,2}(\dot{\epsilon}_v) = 2B_{1,2} \dot{\epsilon}_v \quad (2.39)$$

where $B_{1,2} = \frac{p}{2}(2K_1 + K_2)$ is the “linear” bulk modulus. Likewise, for pure shear ($\dot{\epsilon}_v = 0$) one has

$$\dot{p}_{1,2}(\dot{\epsilon}_d) = K_2 p s_d \cos(2\phi_T - 2\phi_D) \dot{\epsilon}_d. \quad (2.40)$$

According to Luding and Perdahcioglu [87] in the 2D bi-axial geometry the deviatoric strain and pressure increments are coupled with an anisotropy term which characterizes the difference between the horizontal and vertical stiffnesses

$$\Delta p = 2B \Delta \epsilon_v + A \Delta \epsilon_d.$$

Therefore the “linear” anisotropy $A_{1,2} = K_2 p s_d \cos(2\phi_T - 2\phi_D)$ is proportional to the scalar deviatoric stress $\sigma_d = p s_d$.

Similarly the anisotropy appears when the response of the deviatoric stress rate (2.38) to pure isotropic deformation ($\dot{\epsilon}_d = 0$) is computed:

$$\dot{\mathbf{T}}_{1,2}^*(\dot{\epsilon}_v) = A_{1,2}^* \dot{\epsilon}_v \mathbf{I}_T^* \quad (2.41)$$

with $A_{1,2}^* = K_2 p s_d$. Note that $A_{1,2}^* = A_{1,2}$ only when the stress and strain rates are colinear i.e. $\cos(2\phi_T - 2\phi_D) = 1$. Finally, computing the response to pure deviatoric strain ($\dot{\epsilon}_v = 0$) leads to

$$\dot{\mathbf{T}}_{1,2}^*(\dot{\epsilon}_d) = 2K_1 p \dot{\epsilon}_d \mathbf{I}_D^* + K_2 p \dot{\epsilon}_d s_d^2 \cos(2\phi_T - 2\phi_D) \mathbf{I}_T^* \quad (2.42)$$

in the directions of \mathbf{I}_D^* and \mathbf{I}_T^* . In the special case of colinearity $\dot{\mathbf{T}}_{1,2}^*(\dot{\epsilon}_d) = 2G_{1,2} \dot{\epsilon}_d \mathbf{I}^*(\phi)$ where the shear modulus $G_{1,2} = \frac{p}{2}(2K_1 + K_2 s_d^2)$ and $\phi = \phi_T = \phi_D$.

Given constant K_1, K_2 both $B_{1,2}$ and $G_{1,2}$ are linear proportional to p , where $G_{1,2}$ has a nonlinear term $\sigma_d s_d = p s_d^2$. Both anisotropy terms are proportional to σ_d , whereas in [87] they were assumed to be independent of σ_d *a priori*. In the colinear case $A_{1,2}$ and $A_{1,2}^*$ are

identical, as assumed in Ref. [87]. Because $\dot{\epsilon}_d \geq 0$, reversal of the strain rate corresponds to $\phi_D = \phi_T + \pi/2$ and thus causing $\cos(2\phi_T - 2\phi_D)$ to change sign. Strain rate reversal therefore affects $A_{1,2}$ and the second term of $G_{1,2}$. In the spirit of Ref. [87], for $\phi_T = \phi_D$ one has:

$$\begin{aligned}\dot{p}_{1,2} &= 2B_{1,2}\dot{\epsilon}_v + A_{1,2}\dot{\epsilon}_d \\ \dot{\mathbf{T}}_{1,2}^* &= A_{1,2}^*\dot{\epsilon}_v\mathbf{I}_T^* + 2G_{1,2}\dot{\epsilon}_d\mathbf{I}_D^*.\end{aligned}$$

2.3.3 Analysis of the non-linear part and combination of all terms

The norm of the strain rate $\sqrt{\text{tr}\mathbf{D}^2}$ is a common factor of the non-linear terms and is the reason of the inelasticity in the model. Let us first compute the square of \mathbf{D} using (2.33):

$$\begin{aligned}\mathbf{D}^2 &= [\dot{\epsilon}_v\mathbf{I} + \dot{\epsilon}_d\mathbf{I}_D^*]^2 \\ &= \dot{\epsilon}_v^2\mathbf{I} + 2\dot{\epsilon}_v\dot{\epsilon}_d\mathbf{I}_D^* + \dot{\epsilon}_d^2\mathbf{I}_D^*\mathbf{I}_D^*\end{aligned}$$

noting that $\mathbf{I}_D^*\mathbf{I}_D^* = \mathbf{I}$ in 2D the square root of the trace becomes:

$$\sqrt{\text{tr}\mathbf{D}^2} = \sqrt{2}\sqrt{\dot{\epsilon}_v^2 + \dot{\epsilon}_d^2}. \quad (2.43)$$

Now grouping the 3rd and 4th terms under this factor and using (2.32) and $\mathbf{I}_T^*\mathbf{I}_T^* = \mathbf{I}$ for the stress tensor we obtain:

$$\begin{aligned}\dot{\mathbf{T}}_{3,4} &= \left[K_3\mathbf{T}^2 + K_4\mathbf{T}^{*2} \right] \frac{\sqrt{\text{tr}\mathbf{D}^2}}{\text{tr}\mathbf{T}} \\ &= \left[K_3(p^2\mathbf{I} + 2p\sigma_d\mathbf{I}_T^* + \sigma_d^2\mathbf{I}) + K_4\sigma_d^2\mathbf{I} \right] \frac{\sqrt{2}\sqrt{\dot{\epsilon}_v^2 + \dot{\epsilon}_d^2}}{2p}\end{aligned} \quad (2.44)$$

Similar to the previous section the contributions of the non-linear terms to the pressure evolution are computed by taking the trace:

$$\begin{aligned}\dot{p}_{3,4} &= \frac{1}{2}\text{tr}(\dot{\mathbf{T}}_{3,4}) \\ &= \left[K_3p^2 + (K_3 + K_4)\sigma_d^2 \right] \frac{\sqrt{2}\sqrt{\dot{\epsilon}_v^2 + \dot{\epsilon}_d^2}}{2p} \\ &= \frac{p}{\sqrt{2}}\sqrt{\dot{\epsilon}_v^2 + \dot{\epsilon}_d^2} \left[K_3 + \sigma_d^2(K_3 + K_4) \right]\end{aligned} \quad (2.45)$$

and for the deviatoric part:

$$\begin{aligned}\dot{\mathbf{T}}_{3,4}^* &= \dot{\mathbf{T}}_{3,4} - \dot{p}_{3,4}\mathbf{I} \\ &= \sqrt{2}K_3\sigma_d\sqrt{\dot{\epsilon}_v^2 + \dot{\epsilon}_d^2}\mathbf{I}_T^*.\end{aligned} \quad (2.46)$$

Under pure isotropic deformation ($\dot{\epsilon}_d = 0$) the non-linear terms lead to the following rate of pressure change:

$$\dot{p}_{3,4}(\dot{\epsilon}_v) = \frac{P}{\sqrt{2}} |\dot{\epsilon}_v| [K_3 + s_d^2(K_3 + K_4)] \quad (2.47)$$

and for pure deviatoric strain ($\dot{\epsilon}_v = 0$):

$$\dot{p}_{3,4}(\dot{\epsilon}_d) = \frac{P}{\sqrt{2}} |\dot{\epsilon}_d| [K_3 + s_d^2(K_3 + K_4)]. \quad (2.48)$$

The response of the deviatoric part of the non-linear terms (2.46) to pure isotropic deformation ($\dot{\epsilon}_d = 0$) is:

$$\dot{\mathbf{T}}_{3,4}^*(\dot{\epsilon}_v) = \sqrt{2} K_3 \sigma_d |\dot{\epsilon}_v| \mathbf{I}_T^*, \quad (2.49)$$

and for pure deviatoric strain ($\dot{\epsilon}_v = 0$):

$$\dot{\mathbf{T}}_{3,4}^*(\dot{\epsilon}_d) = \sqrt{2} K_3 \sigma_d |\dot{\epsilon}_d| \mathbf{I}_T^*. \quad (2.50)$$

Combining all terms The responses of pressure and deviatoric stress rates to pure isotropic and deviatoric strains including linear and non-linear terms are:

$$\dot{p}(\dot{\epsilon}_v) = p \left\{ (2K_1 + K_2) \dot{\epsilon}_v + \frac{1}{\sqrt{2}} [K_3 + s_d^2(K_3 + K_4)] |\dot{\epsilon}_v| \right\} \quad (2.51)$$

$$\dot{p}(\dot{\epsilon}_d) = p \left\{ K_2 s_d \cos(2\phi_T - 2\phi_D) \dot{\epsilon}_d + \frac{1}{\sqrt{2}} [K_3 + s_d^2(K_3 + K_4)] |\dot{\epsilon}_d| \right\} \quad (2.52)$$

$$\dot{\mathbf{T}}^*(\dot{\epsilon}_v) = \left(K_2 p s_d \dot{\epsilon}_v + \sqrt{2} K_3 \sigma_d |\dot{\epsilon}_v| \right) \mathbf{I}_T^* \quad (2.53)$$

$$\dot{\mathbf{T}}^*(\dot{\epsilon}_d) = 2K_1 p \dot{\epsilon}_d \mathbf{I}_D^* + K_2 p \dot{\epsilon}_d s_d^2 \cos(2\phi_T - 2\phi_D) \mathbf{I}_T^* + \sqrt{2} K_3 \sigma_d |\dot{\epsilon}_d| \mathbf{I}_T^*. \quad (2.54)$$

From these relations it is clear that the behavior for loading and unloading is different because of the $|\dot{\epsilon}_v|$ term. For example, the bulk modulus

$$\begin{cases} B = \frac{p}{2} \left\{ (2K_1 + K_2) + \frac{1}{\sqrt{2}} [K_3 + s_d^2(K_3 + K_4)] \right\} & \text{if } \dot{\epsilon}_v > 0 \\ B = \frac{p}{2} \left\{ (2K_1 + K_2) - \frac{1}{\sqrt{2}} [K_3 + s_d^2(K_3 + K_4)] \right\} & \text{if } \dot{\epsilon}_v < 0. \end{cases} \quad (2.55)$$

On the other hand, the anisotropy for the pressure and deviatoric stress rates do not coincide even when the stress and strain rates are colinear:

$$A = K_2 \sigma_d + \frac{P}{\sqrt{2}} [K_3 + s_d^2(K_4 + K_3)] \quad (2.56)$$

$$A^* = \begin{cases} (K_2 + \sqrt{2} K_3) \sigma_d & \text{if } \dot{\epsilon}_v > 0 \\ (K_2 - \sqrt{2} K_3) \sigma_d & \text{if } \dot{\epsilon}_v < 0. \end{cases} \quad (2.57)$$

Note that $\dot{\epsilon}_d$ is always positive or zero due to the condition in (2.31). Finally if the strain rate and stress are colinear the shear modulus obtained from combination of all terms is

$$G = \frac{P}{2} \left(2K_1 + K_2 s_d^2 + \sqrt{2} K_3 s_d \right). \quad (2.58)$$

The above analysis shows that in the bi-axial geometry the material coefficients of the hypoplastic constitutive model (2.28) are related to the classical elastic moduli and anisotropy as introduced in [87]. The inelastic behavior in the model also appears from the analysis as the derived moduli depend on the direction of loading. On the other hand, there is not a simple relation between the material coefficients and the moduli such that each term in Eq. (2.28) corresponds to a distinct effect. In particular, the bulk modulus and anisotropy depend on all four coefficients.

Chapter 3

Isotropic deformation of frictionless systems*

Abstract

The isotropic compression of polydisperse packings of frictionless spheres is modeled with the discrete element method (DEM). The evolution of coordination number, fraction of rattlers, isotropic fabric, and pressure (isotropic stress) is reported as function of volume fraction for different system parameters. The power law relationship, with power $\approx 1/2$, between coordination number and volume fraction is confirmed in the jammed state for a broad range of volume fractions and for different (moderate) polydispersities. The polydispersity in the packing causes a shift of the critical volume fraction, i.e., more heterogeneous packings jam at higher volume fractions. Close to jamming, the coordination number and the jamming volume fraction itself depend on both history and rate. At larger densities, neither the deformation history nor the loading rate have a significant effect on the evolution of the coordination number.

Concerning the fabric tensor, comparing our DEM results to theoretical predictions, good agreement for different polydispersities is observed. An analytical expression for the pressure as function of isotropic (volumetric) strain is proposed for polydisperse packings, based on the assumption of uniform deformation. We note that, besides the implicit proportionality to contact number density (or fabric), no single power-law is evidenced in the relation for the pressure. However, starting from zero

*Based on F. Göncü, O. Durán, and S. Luding. Constitutive relations for the isotropic deformation of frictionless packings of polydisperse spheres. *Comptes Rendus Mécanique*, 338(10-11):570–586, Oct. 2010

pressure at the jamming point, a linear term with a quadratic correction describes the stress evolution rather well for a broad range of densities and for various polydispersities. Finally, an incremental evolution equation is proposed for both fabric and stress, as function of isotropic strain, and involving the coordination number and the fraction of rattlers, as starting point for further studies involving anisotropic deformations.

3.1 Introduction

Dense granular materials show peculiar mechanical properties quite different from classical fluids or solids [25, 53]. This is true not only for realistic contact forces involving friction and adhesion [18, 83], but already in the frictionless case. Describing granular matter with continuum models is difficult due to their inherent discrete structure and since the origin of their behavior is far from understood [77, 83, 92, 113, 118].

The transition from liquid to solid phases in disordered systems is generally investigated in the context of jamming [28, 92, 113]. Liu and Nagel [77] have suggested that this concept can be applied to different materials in a single framework using a jamming phase diagram with temperature, shear stress, and volume fraction as control parameters. (The volume fraction is the ratio of solid volume to total volume.) For athermal systems like granular materials jamming, i.e., the transition from fluid-like to solid-like behavior, is then essentially determined by the volume fraction and the shear stress [56, 124, 126, 134]. Particularly, if a granular packing is subject to isotropic compression the shear stress is practically zero and the only control parameter is the volume fraction, or equivalently the density (which is the product of volume fraction and material density). Recent numerical and experimental studies with disk and sphere assemblies were performed to identify the critical value at which jamming first occurs [1, 40, 92, 114]. For monodisperse systems it corresponds approximately to the random close packing [1, 28, 114]. Other quantities such as coordination number and pressure were reported to evolve as power laws of the volume fraction in a small interval above the jamming density [92, 113, 114], resembling a phase transition and critical phenomena [25, 53, 77, 113, 114].

Another issue is predicting the mechanical properties of granular materials, which are controlled by the internal structure of the assembly of grains – where the internal structure itself depends on the history of the sample. Although, particles are much smaller than the packing, the presence of discrete force chains in the contact network can lead to long range correlations and thus precludes a straightforward continuum description. Fluctuations of quantities like stress are extreme on the particle scale, i.e., much larger than the mean values, and only over rather large representative volumina these fluctuations decay.

The fabric tensor is commonly used as first harmonic approximation to quantify the structure in disordered systems with an average and a deviatoric (anisotropic) contact density [38, 90]. Numerical studies of the fabric tensor under isotropic deformation of systems with disks, for different polydispersities, have been realized [89, 90] and at least the contact number density could be related to the first three moments of the size-distribution for isotropic situations. Advanced constitutive models within the framework of continuum mechanics employ various definitions of the fabric tensor as a non-classical field. For example, elasto-plasticity and hypoplasticity [140, 146] were generalized to include structure field variables, however, accurate modelling of the effect of structure on the anisotropy of granular materials remains a challenge.

The goal of this study is to test the validity of the power law for the coordination number in polydisperse packings of frictionless spheres also at relatively high volume fractions above jamming and to provide incremental evolution equations for fabric and stress under isotropic deformation. For this, we perform DEM simulations, as introduced in section 3.2, with packings of different polydispersities, number of particles and loading rates. In Secs. 3.3 and 3.4, we numerically analyze the evolution of the coordination number and of the (isotropic) trace of fabric as function of volume fraction and compare the result with theoretical predictions in Refs. [33, 90]. In section 3.5, based on a theory derived in Ref. [33], we present an analytical expression for the pressure as function of the volume fraction, resulting in an incremental evolution equation for isotropic structure (fabric) and stress.

3.2 Simulation method

The Discrete Element Method (DEM) [18, 83, 84] allows us to enclose frictionless particles in a cubic volume with periodic boundary conditions. A linear viscoelastic contact model determines the particle contact forces in normal direction. In order to reduce dynamical effects and shorten relaxation times an artificial viscous background dissipation proportional to the particle velocity is added, resembling the damping due to a background medium. In all simulations gravity is neglected, so that the applied deformations can be assumed isotropic.

3.2.1 Simulation Parameters

Typical values of the simulation parameters are: system size $N = 1000, 5000, \text{ or } 10000$ particles with average radius $\langle r \rangle = 1$ [mm], density $\rho = 2000$ [kg/m³], elastic stiffness $k_n = 10^8$ [kg/s²], particle damping coefficient $\gamma = 1$ [kg/s], background dissipation $\gamma_b = 0.1$ [kg/s] (see Ref. [83] for a discussion of these artificial units, which can be re-scaled due to the simplicity of the contact model). Since the particle size distribution is polydisperse, the

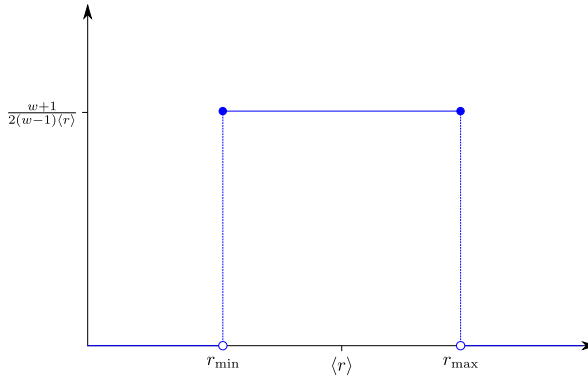


Figure 3.1: Probability density function of the uniform distribution.

contact time depends on the radius of the particles. For example, according to Eq. (2.7)¹ $t_c = 0.31$ [s] is the duration of a contact between the smallest and the biggest particles, with the polydispersity parameter $w = r_{\max}/r_{\min} = 3$ as defined below. The contact time between two average particles with $r/\langle r \rangle = 1$, is $t_c = 0.64$ [s] and their mutual coefficient of restitution is $r = 0.92$. Because t_c is stiffness dependent and can be scaled arbitrarily [83], we do not consider it as an important simulation parameter (as long as the deformation is performed slow, i.e., quasi-statically). Increasing stiffness leads to smaller t_c , i.e., the system has a shorter response time, but has otherwise no effect on the quasi-static results presented in this study.

In order to quantify the volume fraction rate of change during isotropic deformation, the relative loading rate for packings undergoing the same deformation is defined as $D = T_{\text{ref}}/T_{\text{sim}}$, where $T_{\text{ref}} = 1000$ [s] is the duration of the fastest simulation. Values of D used for simulations are 10^{-3} , 10^{-2} , 10^{-1} and 1.

A typical deformation is applied in a strain-controlled manner to the system boundaries (periodic “walls”), with a cosine-shape in order to avoid shocks. In a few cases, other strain functions such as pressure-controlled “wall” displacement and uniform strain field deformation were tested. In the latter case, the particle displacements are determined such that the instantaneous strain field is uniform inside the packing, but relaxation is allowed due to the interactions. We observe that there are no strong differences in the simulation results obtained from different methods as long as the deformation rates are small. (Therefore we do not discuss the actual strain rate, but refer to the scaled (relative) inverse period of deformation $D = T_{\text{ref}}/T_{\text{sim}}$ as dimensionless rate.)

¹ given by the condition $\delta(t_c) = 0$ where δ is the overlap, see Chapter §2.1.

3.2.2 Polydispersity

The polydispersity of the particles can be quantified by the width $w = r_{\max}/r_{\min}$ of the uniform distribution:

$$f(r) = \frac{w+1}{2(w-1)\langle r \rangle} \Theta\left(\frac{2w\langle r \rangle}{w+1} - r\right) \Theta\left(r - \frac{2\langle r \rangle}{w+1}\right), \quad (3.1)$$

with the step function $\Theta(x \geq 0) = 1$ and $\Theta(x < 0) = 0$. The dimensionless moments of the size distribution can be expressed as functions of w :

$$\hat{r}_k := \frac{\langle r^k \rangle}{\langle r \rangle^k} = \frac{2^k}{(k+1)(w+1)^k} \sum_{i=0}^k w^i, \quad (3.2)$$

with the first two moments $\hat{r}_1 = 1$, and $\hat{r}_2 = \frac{4}{3} \frac{1+w+w^2}{(w+1)^2}$. Typical values of w are 1, 2 and 3, where $w = 1$ corresponds to a monodisperse packing. A few simulations with larger $w \leq 8$ were also performed. Simulations with other size distribution functions and a theoretical analysis of polydisperse packings will be published elsewhere [33].

3.2.3 Preparation and test procedure

The initial packing is obtained by compressing a (fully) random granular “gas” up to a volume fraction close to jamming and letting it relax. Figure 3.2 shows the initial configuration of a system of 1000 particles, the granular gas state, before, and the granular fluid state, after first relaxation at an initial volume fraction below jamming $v_i = 0.64$. The initial granular gas (Fig. 3.2(a)) has many particles which have large overlaps due to the random positioning. However they quickly repel each other after a short simulation time (Fig. 3.2(b)). From the granular fluid, below jamming, the system is slowly compressed and the evolution of the kinetic and potential energies is displayed during relaxation and compression. The packings are isotropically compressed by moving simultaneously inwards the (fictive, periodic) boundaries of the simulation domain, see Figs. 3.2(b)-(d). After maximal compression to $v_{\max} = 0.75$, the process is reversed until the initial volume fraction v_i is recovered.

Besides (artificial) contacts at the initial state (which disappear immediately due to the high repulsive forces involved), contacts are closed permanently only above the jamming volume fraction. The potential energy is an indicator of the overlaps of the particles. However, since the compression is rather fast, one can observe considerable potential energy due to collisions in the fluid-like state, at densities $v_i < v < v_j$, with jamming volume fraction v_j . From Fig. 3.2(f), in the loading or un-loading state, one observes that the kinetic energy is smaller than the potential energy at the higher densities. In the (isotropic) jammed, solid state, the potential energy is considerably larger than the kinetic energy, whereas in the fluid-like state referred to above it is significantly smaller. This is a rough indicator of the

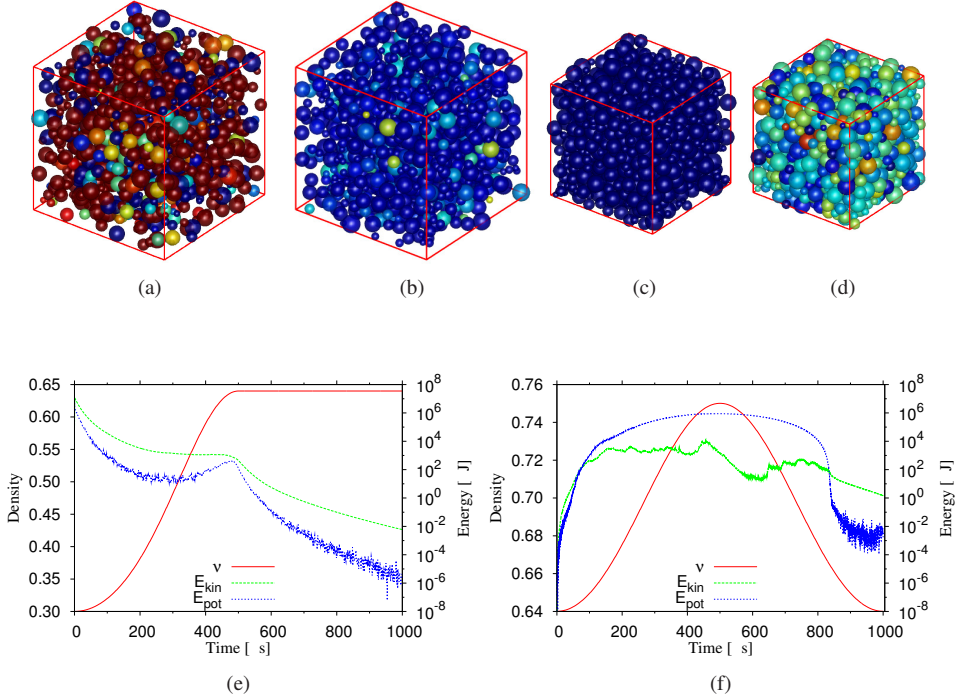


Figure 3.2: Snapshots of the (a) initial (fully) random configuration of the particles ($N = 1000$) with big (artificial) overlaps and (b) the situation after only 40 seconds compression when all artificial overlaps have disappeared. The color code indicates overlaps of the particles (red: big overlaps, blue: no overlap). (c) Snapshot of the relaxed granular “fluid” with volume fraction $v_i = 0.64$. Note that although particles are densely packed they have still practically no overlap, since the volume fraction is below the jamming value v_j . (d) Snapshot of the strongly compressed packing, with $v_{max} = 0.75$ using the same color code as in (a), (b) and (c). (e) Evolution of the volume fraction, the potential and the kinetic energy during initial compression and relaxation and (f) the loading-unloading cycle.

jammed regime, however, not really an objective criterion due to the dynamic loading and unloading. Close to the maximal volume fraction, due to our co-sinusoidal loading procedure, the kinetic energy drops exponentially over about two orders of magnitude between times $t = 480$ s and ~ 580 s. For larger times, the rate of change increases so that the kinetic energy increases again, showing jumps whenever the packing re-arranges.

Around time $t = 850$ s, the volume fraction drops below the un-loading jamming value and the kinetic energy becomes larger than the potential energy. Also in this fluid-like high-density granular gas, the kinetic energy drops approximately exponentially due to collisional cooling, however, with a different rate as before in the high density, slow deformation regime.

3.3 Evolution of the coordination number

In theory, the jamming transition occurs at the isostatic point [113, 114, 127]. In an isostatic packing of frictionless particles, the coordination number, i.e., the average number of contacts per particle, is $C = 2D$ where D is the dimensionality of the system. One can expect smaller coordination numbers when tangential elastic forces are involved, however, even in simulations and experiments with very small tangential forces, the reported values of C are consistently below $2D$. This is due to the definition of an isostatic packing, which excludes all particles that do not belong to the force network, i.e., ideally, particles with exactly zero contacts are excluded. Nevertheless, in addition to the particles with zero contacts, there may be particles having a finite number of contacts for some short time, which do not contribute to the mechanical stability of the packing. The contacts of these rattlers are transient because the repulsive contact forces push them away from the mechanically stable backbone. Thus, if the packing was allowed to relax after every deformation step, or deformed very slowly, these particles would lose all of their contacts.

Although it is possible to numerically check the contribution of every particle to the force network [70] an easier although less rigorous way to identify rattlers is to just count their contacts. Since frictionless particles with less than four contacts are not mechanically stable they are defined as rattlers. This leads to the following abbreviations and definitions as used in the rest of this study.

N : Total number of particles

$N_4 := N_{C \geq 4}$: Number of particles with at least 4 contacts

M : Total number of contacts

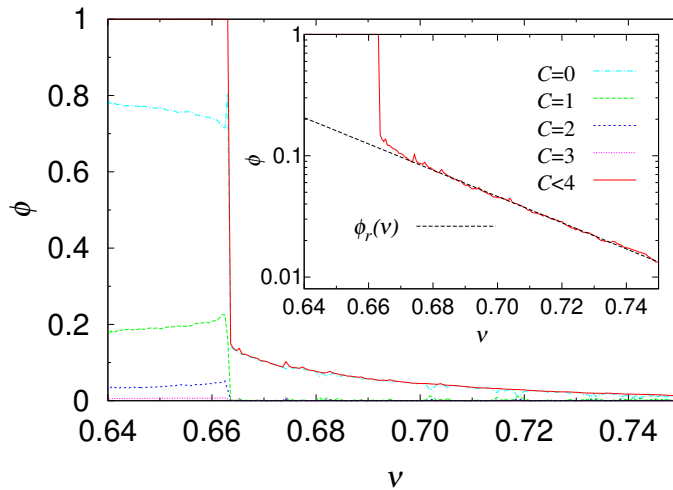
$M_4 := M_{C \geq 4}$: Total number of contacts of particles with at least 4 contacts

$$\begin{aligned}
C^r &:= \frac{M}{N} : \text{Coordination number (classical definition)} \\
C &:= C^m = \frac{M_4}{N} : \text{Coordination number (modified definition)} \\
C^* &:= \frac{M_4}{N_4} = \frac{C}{1 - \phi_r} : \text{Corrected coordination number} \\
\phi_r &:= \frac{N - N_4}{N} : \text{(Number) fraction of rattlers} \\
v &:= \frac{1}{V} \sum_{p \in N} V_p : \text{Volume fraction of particles} \\
v^* &:= v - v_r = \frac{1}{V} \sum_{p \in N_4} V_p : \text{Volume fraction of particles excluding rattlers} \\
v_r &:= \frac{1}{V} \sum_{p \notin N_4} V_p : \text{Volume fraction of rattlers}
\end{aligned}$$

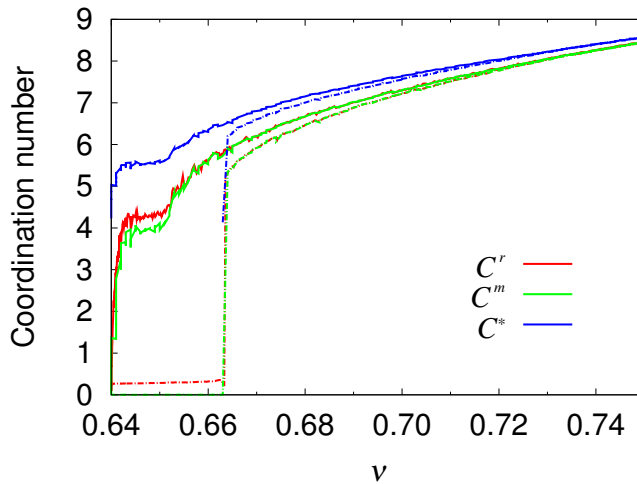
The difference between coordination numbers C^r and C is not caused by the “ideal rattlers” with $C = 0$, since those do not contribute to C anyway. It is caused by those particles (virtual, dynamic rattlers) with $1 \leq C \leq 3$, which are not mechanically stable, i.e., temporary, members of the contact network. They are neglected when counting the contacts M_4 . In the following, we will use the modified coordination number $C := C^m$, instead of C^r , since it better resembles the slow, quasi-static deformation mode of the system, as will be discussed below.

The ratio of M_4 and N_4 provides the *corrected coordination number* C^* , which perfectly follows the isostaticity arguments. The fraction of rattlers and a comparison between the classical, the modified and the corrected definitions are shown in Fig. 3.3. The values of C^r and C^m are very similar, since the number of contacts originating from particles with $C = 1, 2$, or 3 contacts is small anyway and decays with decaying rate of deformation. considerably larger and all coordination numbers display a sharp jump at the jamming transition during un-loading. In the left panel, Fig. 3.3(a), the respective fractions of particles with different numbers of contacts are shown, where the red solid line represents ϕ_r . Coming from high densities, the fraction of rattlers increases and jumps to unity when approaching v_r . In the right panel, Fig. 3.3(b), the different versions of the coordination numbers are compared, showing that, while the loading and unloading branch are clearly different, C^r , and C , are only slightly different close to and below the critical volume fraction v_c . Even though larger, C^* behaves qualitatively similar below and above the jamming transition.

However, since C^* involves not all particles, it cannot easily be related to the total particle volume, or the mass-density of the system – that is equivalent to the volume fraction, i.e., $\rho = \rho^p v$, with the particle material density ρ^p – as experimentally accessible for many systems. The average contact number density vC can be related to the mechanically relevant



(a)



(b)

Figure 3.3: (a) Evolution of the fraction of rattlers as function of volume during fraction during unloading for a simulation with $N = 10000$, $w = 3$, and $D = 0.001$. Inset: Fit of Eq. (3.3). (b) Comparison of the coordination numbers computed using the classical C^r , the modified C^m and the corrected C^* , for the same simulation. The data for loading and unloading are shown by solid and dashed lines, respectively.

contact number density v^*C^* (without rattlers):

$$vC = \frac{N\langle V_p \rangle}{V} C = \frac{(1 - \phi_r)N\langle V_p \rangle}{V} \frac{C}{1 - \phi_r} = (1 - \phi_r)vC^* \neq v^*C^* = (v - v_r)C^*,$$

where V is the volume occupied by the packing. The non-equality could become equal only if the average volume of rattlers is equal to the average volume of all particles, i.e., if $v_r/v = \phi_r$. Unfortunately, there is no simple exact relation between vC and v^*C^* , as discussed below in section 3.4, since the smaller particles are more likely to be rattlers. Therefore, we will work with the parameters v , $C^*(v)$ (see below), and $\phi_r(v)$.

The fraction of rattlers, in the quasi-static limit, i.e., for extremely slow deformations, as presented below, obeys the empirical relation:

$$\phi_r(v) = \phi_c \exp \left[-\phi_v \left(\frac{v}{v_c} - 1 \right) \right] \quad (3.3)$$

for $v \geq v_c$ and $\phi_r(v < v_c) = 1$ otherwise. This involves two fit parameters (i) the fraction of rattlers at jamming, ϕ_c , and (ii) the rate of decay of rattlers with increasing packing fraction, ϕ_v . A fit of $\phi_r(v)$ is shown in the inset of Fig. 3.3(a). Note that v_c cannot be obtained by the fit like Eq. (3.3), but has to be obtained by other means [40], e.g., by identification of the jump/discontinuity of $\phi_r(v_c)$. Typical values are $\phi_c \approx 0.13 \pm 0.03$ and $\phi_v \approx 15 \pm 2$. The observation that one has $\phi_r(v_{\text{RLP}}) \approx 1$ at the random loose packing fraction $v_{\text{RLP}} \approx 0.57$ is presumably accidental.

The corrected coordination number C^* , obtained by disregarding rattlers, obeys a power law of volume fraction as reported previously [92, 113, 114, 127]:

$$C^*(v) = C_0 + C_1 \left(\frac{v}{v_c} - 1 \right)^\alpha, \quad (3.4)$$

where v_c is the critical volume fraction, C_0 is the critical coordination number, and C_1 is the prefactor for the power-law with power α . Given $C_0 = 4, 6$ in two and three dimensions, for isostatic packings of frictionless particles, this would leave three more fit parameters (iii) $v_c \approx v_{\text{RCP}}$, (iv) $C_1 \approx 8$, and (v) $\alpha \approx 0.5$. However, we sometimes allow also C_0 as a variable in order to check the consistency with the isostaticity assumption for the packings.

Below we check this analytical expression for $C^*(v)$ for the un-loading branch of our simulations, since these data show less dynamical artefacts than data from the loading branch. We do not discuss cyclic loading and un-loading, which can lead to a continuous ‘‘drift’’ (increase) of v_c with each loading cycle [23]. Within the present work, the hysteresis under cyclic loading, and possible quantitative information that can be extracted from it (as, e.g., in magnetic systems), is not studied in detail.

Note that we do *not* identify the v_c for un-loading with *the* jamming volume fraction v_j . Actually, we doubt if there is *one* jamming volume fraction. The critical value rather depends on the contact properties and on the history of the packing, especially when realistic

properties like friction are involved, but also for the frictionless case studied here. A detailed study of the dependence of v_c on the contact properties and on the history of the packing in general is far from the scope of this study, so that we focus mainly on the first un-loading branch.

3.3.1 Influence of polydispersity

In order to understand the effect of polydispersity, we first perform simulations using three rather small packings of 1000 particles with three different widths of the size distribution $w = 1, 2, 3$. These samples are compressed and then decompressed, at the same rate, between $v_1 = 0.5$ and $v_{\max} \simeq 0.9$. Figure 3.4 displays the relation between volume fraction and coordination number for these packings. The finite values of the coordination number during compression, at low densities, make the transition from fluid to solid state difficult to detect. This is due to temporary contacts which arise from the dynamics at low densities. If the packing is allowed to relax the dynamic contacts become less and the state of zero coordination is approached, as expected.² However, not even our slowest simulations allowed us to avoid dynamic contacts in the compression branch.

On the other hand, a much cleaner, very sharp decrease in C is observed during un-loading (decompression), when we approach v_c from high densities, see Fig. 3.4. The fit of Eq. (3.4) to the corrected coordination number, C^* , computed during decompression, is shown in the inset of Fig. 3.4. The transition from the jammed to the unjammed state occurs at higher volume fractions for more polydisperse, heterogeneous packings. A list of the numerical values of the fit parameters is given in table 3.2.

Even though the system is rather small and the deformation rate is rather high, the fitted parameters are almost consistent with the isostaticity assumption, $C_0 = 6$. When this is imposed, the fit parameters are close to each other and become almost independent of w . Only for v_c there is an increasing trend for increasing w .

²**Remark on the fit of Equation (3.4).** We choose to fit Eq. (3.4) to the decompression branch of the simulation data because the system's kinetic to potential energy ratio is much lower than during compression in this density range, see Fig. 3.2(f), even for the rather fast compression used. Furthermore, boundary effects are less important during decompression because the system is expanding and possible spurious contacts caused by the (virtual, periodic) wall motion are avoided. In a separate set of simulations, we find that by adding extra relaxation between deformation steps, the compression and decompression branches of $C(v)$ can get closer to each other (data not shown). The distance between the branches reduces with the relaxation step but does not disappear even for the largest relaxation-times. Since the unloading branch is much less sensible to the protocol and rate of deformation, from now on, we will fit Eq. (3.4), i.e., the analytical expression of the corrected coordination number, exclusively to the decompression branch of the simulation data.

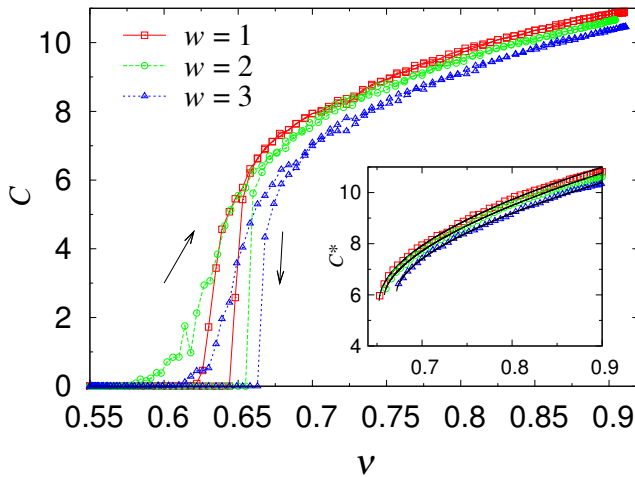


Figure 3.4: Coordination number C as function of volume fraction v for packings of 1000 particles with different size distributions of width w , as given in the figure. The arrows indicate the compression (up) and decompression (down) directions. Inset: The lines are fits of the corrected coordination number according to Eq. (3.4), with the fit-parameters given in table 3.2.

3.3.2 History and system size dependence

It is especially interesting to see how parameters such as deformation history and system size affect jamming and the evolution of the coordination number. We studied the effect of deformation history by compressing and decompressing isotropically two packings with 1000 particles and polydispersity $w = 3$, but for different volume fraction ranges. The first sample is compressed from an initial state close to jamming up to a very high volume fraction ($v : 0.64 \rightleftharpoons 0.9$) and back. The second sample is compressed from the same initial state up to a moderate volume fraction ($v : 0.64 \rightleftharpoons 0.75$) and back.

Figure 3.5(a) shows the evolution of the coordination number as function of v for both samples. Although, the highly compressed packing seems to have a larger critical volume fraction, the difference practically disappears when rattlers are removed. Figure 3.5(b) shows the corrected coordination number C^* during decompression and the fit of Eq. (3.4) to the data obtained from the moderately compressed sample. Note that the fit is also quite good as an extrapolation for stronger compression, i.e., higher densities, suggesting that isotropic deformation history has no substantial effect on the coordination number at higher volume fractions.

The size of the system has no effect on the critical volume fraction and the evolution of the

(a)				(b)			
w	1	2	3	w	1	2	3
C_0	6.0000	5.9690	6.1158	C_0	6	6	6
C_1	8.7989	8.5539	7.9439	C_1	8.7363	8.5561	7.9367
α	0.5363	0.5776	0.5737	α	0.5662	0.5826	0.5542
v_c	0.6524	0.6582	0.6718	v_c	0.6548	0.6585	0.6707

Table 3.2: (a) Numerical values of the fit-parameters obtained by fitting Eq. (3.4) to the un-loading simulation data of Fig. 3.4, in the intervals $[0.655:0.85]$, $[0.66:0.85]$ and $[0.672:0.85]$ for $w = 1, 2$ and 3 , respectively. (b) Numerical values of the fit-parameters obtained by fitting Eq. (3.4) to the un-loading simulation data of Fig. 3.4, in the same intervals and fixing $C_0 = 6$.

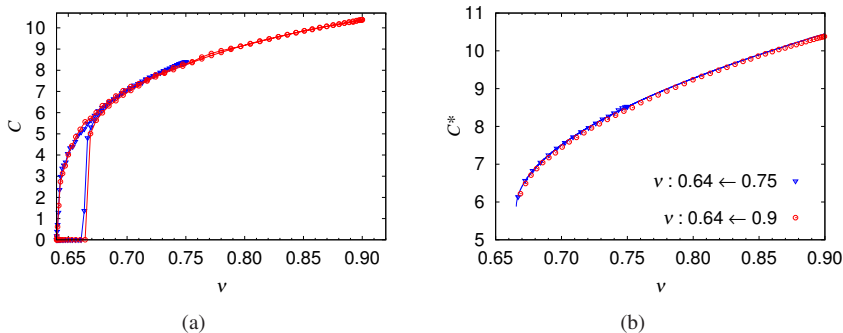


Figure 3.5: (a) Coordination number C as function of volume fraction v for different compression histories. (b) Evolution of C^* during decompression. The solid line is the fit of Eq. (3.4) to the data obtained from the moderately compressed sample ($v : 0.64 \rightleftharpoons 0.75$).

coordination number. Figure 3.6 illustrates the coordination number as function of volume fraction during a cycle of compression–decompression for three packings comprising $N = 1000, 5000$ and 10000 particles. All samples are deformed at the same relative rate $D = 0.5$, with the same polydispersity parameter $w = 3$. The small size systems show stronger fluctuations prior to jamming since dynamical effects are more pronounced for. On the other hand, after jamming all curves obey a similar power law as confirmed by the fits of Eq. (3.4) to the corrected coordination number C^* , shown in the inset of Figure 3.6.

The values of the critical volume fractions obtained from the fits are 0.6650 ± 0.0002 , 0.6647 ± 0.0001 , and 0.6652 ± 0.0001 , for $N = 1000, 5000$, and 10000 , respectively. The other parameters, see Table 3.3, are very close to each other and to those reported in Table 3.2. These rather small differences between the critical volume fractions (and also the other fit parameters) for different N imply that the system size does not have an important effect on

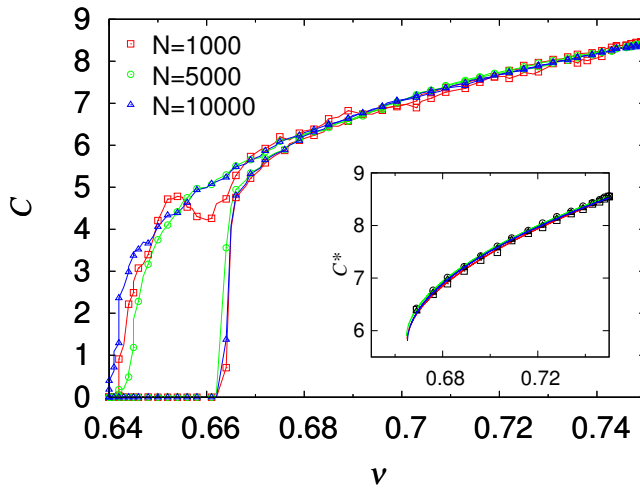


Figure 3.6: Evolution of the coordination number for different system sizes, with $w = 3$ and $D = 0.5$. Inset: Fits of the corrected coordination number C^* according to Eq. (3.4). The red, green and blue lines are the fits for $N = 1000$, 5000 and 10000 , respectively.

the evolution of the (corrected) coordination number C^* . Larger systems display smaller statistical fluctuations, however.

3.3.3 Effect of loading rate

The effect of the loading rate on jamming and the evolution of the coordination number is analyzed by applying isotropic deformation to a polydisperse ($w = 3$) sample at various rates. Figure 3.7(a) shows the evolution of the coordination number as function of volume fraction for a packing of 10000 particles deformed at relative rates $D = 1, 0.5, 0.1, 0.01$, and 0.001 . The fits of Eq. (3.4) to the corrected coordination number are shown in Fig. 3.7(b) and the fit parameters are summarized in table 3.3.

The jamming transition should best be studied in the quasi-static limit, i.e., for $D \rightarrow 0$, when the sample has infinitely long time to relax. However, practically, this is impossible [114]. Using the fit of Eq. (3.4) for a systematic study of the deformation rate effect on the critical volume fraction is not reliable due to the singularity of its derivative at this point. The rapid change of the slope of $C^*(v)$ near jamming increases the sensitivity of other parameters to the fit range and causes them to fluctuate. When studying the jamming transition, in recent studies, the densities very close to v_c were carefully studied. Note that here, we provide data for a much wider range of densities, far away from the transition – to be used for practical applications. Therefore, the parameters and especially the exponents reported in this study

	$N = 1000$		$N = 5000$	
	$D = 1$	$D = 0.5$	$D = 1$	$D = 0.5$
C_0	5.0256	5.8221	5.7645	5.8838
C_1	7.5938	8.4875	8.2019	8.1661
α	0.3904	0.5572	0.5279	0.5431
v_c	0.6650	0.6650	0.6654	0.6647
v_c^\dagger	0.6652	0.6644	0.6624	0.6620

	$N = 10000$				
	$D = 1$	$D = 0.5$	$D = 0.1$	$D = 0.01$	$D = 0.001$
C_0	5.7645	5.7887	6.0643	6.1587	6.1853
C_1	8.2019	7.9915	8.4204	8.8347	8.7514
α	0.5279	0.5199	0.5909	0.6301	0.6318
v_c	0.6654	0.6652	0.6648	0.6645	0.6644
v_c^\dagger	0.6627	0.6632	0.6633	0.6634	0.6633

Table 3.3: Numerical values of the fit parameters of Eq. (3.4) for various system sizes and loading rates. All packings have the polydispersity parameter $w = 3$ and are deformed within the range $v : 0.64 \rightleftharpoons 0.75$. The fits are performed in the intervals $[v_1 : v_2]$, with $v_1 = 0.665$ and $v_2 = 0.75$. v_c^\dagger are the volume fractions at which the pressure vanishes during unloading, see Ref. [40]. Note that the data in table 3.2 are slightly different (since they come from simulations with different initial conditions), which tells us something about the sensitivity and variation of parameters with different initial configurations.

can be slightly different from those in previous studies.

For example, the exponent $\alpha \simeq 0.5$ previously reported in [92] for 2D and [113, 114] for 3D, cannot be always recovered (see Table 3.3) for very slow compression; we rather find $\alpha \simeq 0.66$ for the slowest compression rates. The critical volume fraction, on the other hand, is not varying much and these variations are presumably due to the sensitive fit function with a singular slope close to v_c , as mentioned already above. In Ref. [40], alternative methods were compared to determine the critical volume fraction based on the fraction of rattlers, the pressure, and the ratio of the kinetic and potential energies of the packing. For a better, more objective analysis of rate effects, we believe that the fit should be used in conjunction with at least one of these methods. Then, when obtained independently, v_c is not a free fit parameter anymore. However, since changing the loading rate seems to have no strong effect on v_c , and the coordination numbers at volume fractions considerably above v_c , we do not pursue this further.

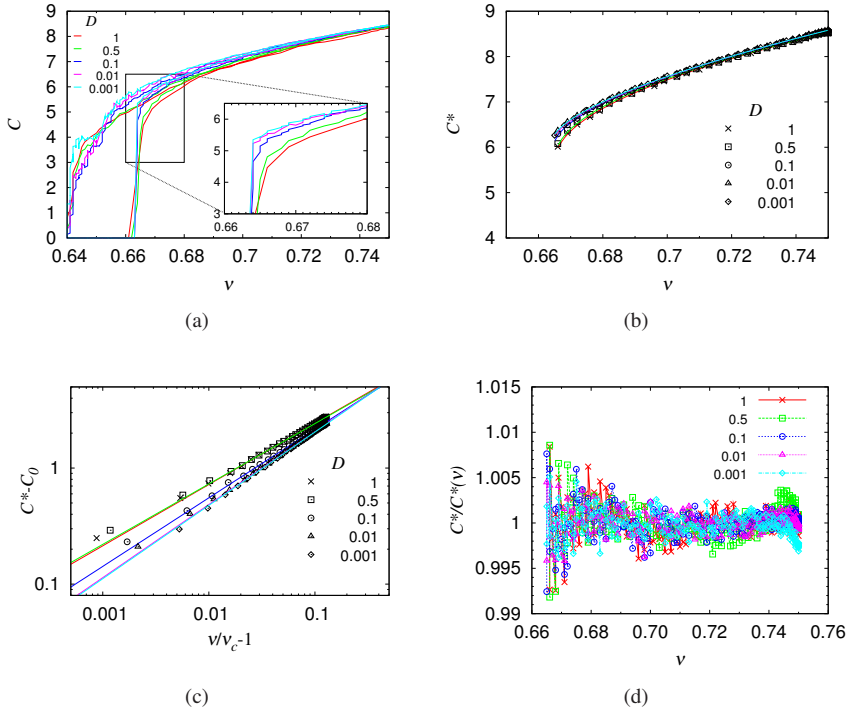


Figure 3.7: (a) Evolution of the coordination number for different deformation rates. Inset: Zoom into the decompression branch during transition from the jammed to the unjammed state. (b) The corrected coordination number C^* and the fits of Eq. (3.4). (c) Log-log plot of $C^* - C_0$ against $(\nu/\nu_c - 1)$ from the same data as in (a) and (b). (d) the ratio of data and fit, $c^*/c^*(\nu)$, indicates that the quality of the fit is better than one percent for the full range of data $[\nu_c; 0.75]$.

3.4 Fabric Tensor

In the following, we compare the simulation results on the trace of the fabric tensor to the recent 3D predictions of Durán *et al.* [33] that complement the older 2D results by Madadi *et al.* [89, 90]. In these studies, the effect of polydispersity on the trace of the fabric tensor was expressed in terms of the moments of the size distribution. The basic assumption, in both 2D and 3D, is that the linear compacity c_s , defined as the fraction of the particle surface shielded by its neighbors, is independent of the particle radius. From this the trace of the fabric is found to be proportional to the contact number density, νC , and a dimensionless pre-factor (see g_3 below) that only depends on the moments of the size-distribution. Since derivation is similar in both 2D and 3D, only some formulas are shown; for more details we

refer to Refs. [33, 89, 90].

As first order approximation, in 3D, the mean number of contacts, $C(r)$, of a particle with radius r is inversely proportional to the fraction of its surface $\Omega(r)/(4\pi)$ shielded by a neighboring sphere of characteristic radius $\langle r \rangle$, such that:

$$C(r) = \frac{4\pi c_s}{\Omega(r)}, \quad (3.5)$$

where $\Omega(r) = 2\pi(1 - \cos \alpha)$, with the sinus and cosinus of the shielding half-angle, $\sin \alpha = 1/(r/\langle r \rangle + 1)$ and $\cos \alpha = \sqrt{1 - \sin^2 \alpha}$, respectively. When inserting Eq. (3.5) into the definition of the average coordination number $C = \int_0^\infty C(r)f(r)dr = 4\pi c_s \int_0^\infty [f(r)/\Omega(r)]dr$, it is possible to calculate explicitly the expected compacity for different C :

$$c_s(C) = \frac{a_2 C}{1 - C_2 + C_2 \hat{r}_2}, \quad (3.6)$$

with the dimensionless second moment \hat{r}_2 from Eq. (3.2). Using the quadratic approximation of Durán *et al.* [33] for the solid angle $\Omega(r)$ leads to $a_2 = \Omega(\langle r \rangle)/(4\pi) = \frac{1}{2}(1 - \sqrt{3}/2)$, $B_2 = \sqrt{3}/24a_2$, and $C_2 = B_2(B_2 - 5/6)$. For example, in the monodisperse special case one has $c_s = a_2 C$, so that inserting the isostatic limit $C^* = C(1 - \phi_c) = 6$ leads to $c_s = 6a_2/(1 - \phi_c) \approx 0.47$ for $\phi_c \approx 0.15$, i.e., about half of the surface of particles is shielded close to the jamming point.

Figure 3.8 shows the numerical data for the coordination number $C(r)$ and the compacity $c_s(r)$ as function of $r/\langle r \rangle$ for $w = 3$ (for which $\hat{r}_2 = 13/12$) and two different volume fractions: a very high one ($v \approx 0.74$) and one close to jamming ($v \approx 0.67$), along with the predicted relations from Eqs. (3.5) and (3.6), for coordination number and compacity, respectively. Although, Eq. (3.5) describes the size-dependent contact number qualitatively well for a broad range of densities, at small radii, the contact number drops considerably below the predictions, see Figs. 3.8(a) and 3.8(c). The assumption of a constant compacity is confirmed for the larger particle radii, but fails for smaller radii, see Figs. 3.8(b) and 3.8(d).

Using the average coordination number, C , or inserting $C^* = C/(1 - \phi_r)$ into Eq. (3.6) leads to the red and blue data sets, respectively. Clearly the theoretical prediction that uses C is superior to the one using C^* . Nevertheless, we report the interesting and intuitive observation that the latter coordination number has a lower limit $C^*(r) \geq 4$, since rattlers are excluded. Since small particles have smaller surface area, their chance to have less than four contacts is higher, so that more rattlers are from the small fractions. Interestingly, the data for $c_s(r)$ indicate that those small particles that are not rattlers have a *higher* compacity than the average. Different shapes and wider size distributions have to be studied to allow more general insights.

Using the definition of the average coordination number, C , the trace of the fabric can be

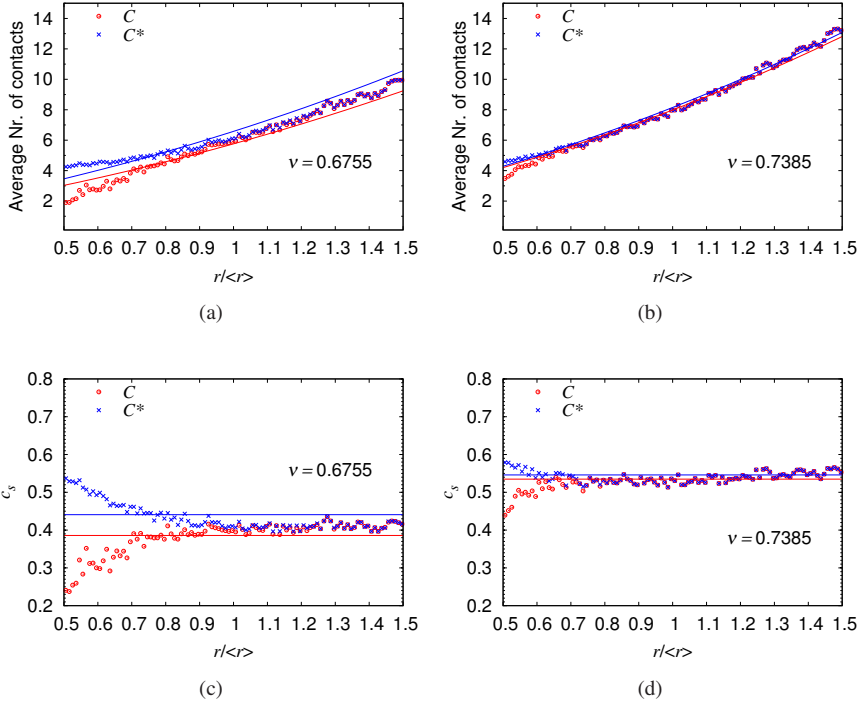


Figure 3.8: (a,b) Average number of contacts $C(r)$ as function of the normalized particle radius, including (red) and excluding (blue) rattlers, at different volume fractions for packings with $N = 10000$ particles. The points are data from the simulations while the solid lines are the analytical predictions of Eq. (3.5) using either $c_s(C)$ (red) or $c_s(C^*)$ (blue), and thus confirming that using $c_s(C) = c_s((1 - \phi_r)C^*)$ in Eq. (3.6) is self-consistent. (c,d) Linear compacity c_s as function of the normalized radius, computed from the same packings as in (a) and (b), including (red) and excluding (blue) rattlers. Again the solid lines are the theoretical prediction of Eq. (3.6).

written as detailed in Ref. [33]:

$$F_V = \text{tr}(\mathbf{F}) = (1/V) \sum_{p \in V} V_p C_p = (N/V) \int_0^\infty dr V_p(r) C(r) f(r) = g_3 v C, \quad (3.7)$$

with the volumes V_p and the contact numbers C_p of particles p , and the term g_3 , which contains the information about the polydispersity, which is defined as [33]:

$$g_3 = \frac{\langle r^3 \rangle_\Omega}{\langle r^3 \rangle} = \frac{\int_0^\infty r^3 [f(r)/\Omega(r)] dr}{\langle r^3 \rangle \int_0^\infty [f(r)/\Omega(r)] dr}, \quad (3.8)$$

where the brackets $\langle \dots \rangle_\Omega$ indicate the normalized averaging over the modified distribution function $[f(r)/\Omega(r)]$. Using the moment expansion of Durán *et al.* [33], the lowest order analytical approximation (that involves moments up to order $k = 5$) is:

$$g_3 \approx \frac{1 - B_2 + C_2 + (B_2 - 2C_2) \frac{\langle r^4 \rangle}{\langle r \rangle \langle r^3 \rangle} + C_2 \frac{\langle r^5 \rangle}{\langle r \rangle^2 \langle r^3 \rangle}}{1 + C_2 \left[\frac{\langle r^2 \rangle}{\langle r \rangle^2} - 1 \right]} \quad (3.9)$$

where the constants B_2 and C_2 were defined in the previous section. This is considerably more involved than the 2D results [89, 90], since none of the above terms can be neglected [33]. Only for the monodisperse situation, one has the simplification $g_3 = 1$.

Equation (3.7) is plotted in Fig. 3.9 using the simulation data for different distribution widths w . For all distributions and packing densities from very loose up to very dense packings ($v \sim 0.9$), the proportionality between the trace of the fabric and the contact density is well described by Eq. (3.9), when the correction factor g_3 is used. More explicitly, the correction factor, even though not perfect, improves the quality of the prediction considerably. The reason for the remaining disagreement of order of 1% can be due to the assumption of particles of radius r being surrounded by particles of mean radius, due to neglecting the overlap of the particles in the theoretical considerations, or due to the higher probability for small particles to be rattlers.

The moments of the size distribution can be expressed in terms of the relative width w using Eq. (3.2), which allows us to study the behavior of g_3 as a function of w . The inset of Fig. 3.9 shows the analytical approximation and the exact definition of g_3 , from Eq. (3.8), along with the values of g_3 obtained from the DEM simulation. For highly polydisperse packings, corresponding to large w , the k th moment becomes $\langle r^k \rangle \rightarrow \langle r \rangle^k 2^k / (k + 1)$ and g_3 thus saturates at a constant $g_3^{\max} \approx 1.62$. Therefore, the influence of an increase in the polydispersity on $\text{tr}(\mathbf{F})$ is limited for high w in the framework of the approximations made. A more detailed study of this prediction for wide size distributions is, however, far from the scope of this study.

3.5 Pressure

In this section, the pressure is introduced and related to the other system properties volume fraction, coordination number, fraction of rattlers, and fabric. In order to better understand the final analytical expressions, the stress is rewritten and re-phrased, starting from the traditional definitions.

The micromechanical stress tensor components for a (static) particle (in mechanical equilib-

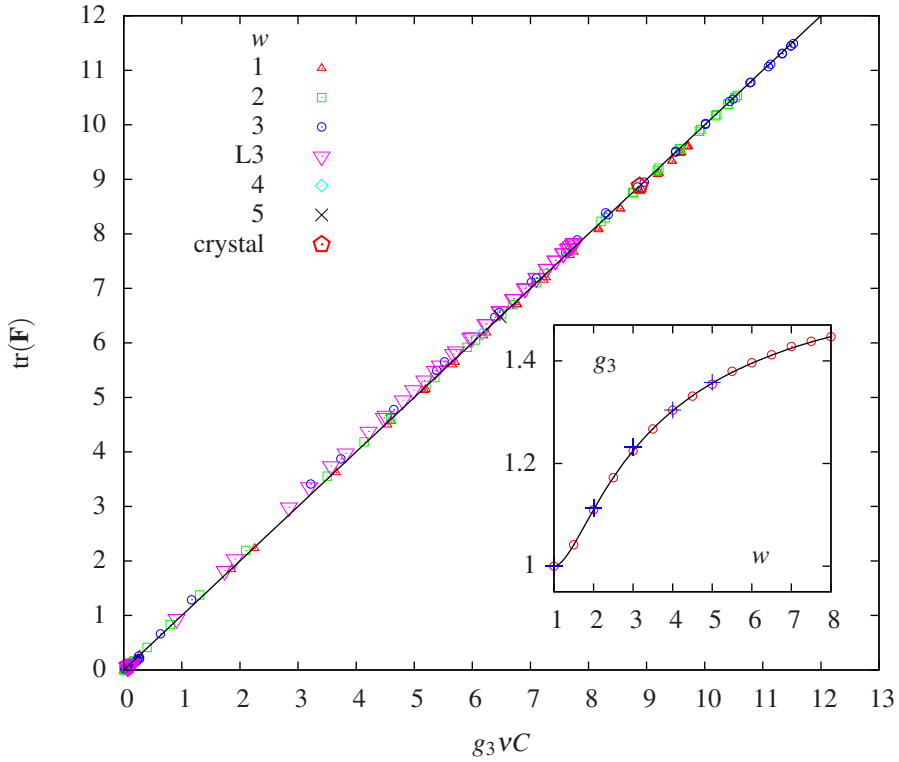


Figure 3.9: The trace of the fabric tensor as given by Eq. (3.7) for different size distributions with w given in the inset from simulations with $N = 1000$ (“L3” indicates a larger simulation with $N = 10000$ and “crystal” indicates an ordered lattice structure whereas $w = 1$ is a disordered, monodisperse configuration). Each data-point corresponds to one density and fabric, as averaged over the whole system, at different densities during decompression. Inset: The constant g_3 plotted as function of w from its definition (\circ), the analytical approximation (solid line) and the simulation data ($+$).

rium) are defined as:

$$\sigma_{ij}^p = \frac{1}{V_p} \sum_{c=1}^{C_p} l_i^{pc} f_j^{pc}, \quad (3.10)$$

where $\mathbf{l}^{pc} = (r_p - \delta_c/2)\hat{\mathbf{n}}$ is the branch vector of contact c and $\mathbf{f}^{pc} = k_n \delta_c \hat{\mathbf{n}}$ is the (linear) force associated, with particle radius, r_p , overlap δ_c , spring-stiffness, k_n , and the contact-direction unit vector, $\hat{\mathbf{n}}$. Here we assume [83] that the contact point is located at the middle of the

overlap.³ From these definitions, the trace of the stress for a single particle becomes:

$$\text{tr}(\boldsymbol{\sigma}^p) = \frac{k_n}{V_p} \sum_{c=1}^{C_p} \delta_c \left(r_p - \frac{\delta_c}{2} \right), \quad (3.11)$$

with the number of contacts C_p of particle p . For a packing of N particles, the trace of the average stress tensor can be computed by weighing the particles according to their volume [73]:

$$\begin{aligned} \text{tr}(\boldsymbol{\sigma}) &= \frac{1}{V} \sum_{p \in V} V_p \text{tr}(\boldsymbol{\sigma}^p) \\ &= \frac{k_n}{V} \sum_{p=1}^N \left(r_p \sum_{c=1}^{C_p} \delta_c - \frac{1}{2} \sum_{c=1}^{C_p} \delta_c^2 \right), \end{aligned} \quad (3.12)$$

where V is the total volume of the packing.

One can express V in terms of the volume fraction and the volume of N particles as $V = N \langle V_p \rangle / \nu$, with $\langle V_p \rangle = \frac{4\pi}{3} \langle r_p^3 \rangle$, where the brackets denote averaging of a particle-property A_p over all particles in a packing, e.g., $\langle A \rangle := \langle A_p \rangle = \frac{1}{N} \sum_{p=1}^N A_p$. Introducing also the normalized average normal force for each particle p as $\phi_p \equiv f_p / \langle f_p \rangle$, with $f_p = \sum_{c=1}^{C_p} k_n \delta_c$, the trace of the averaged stress tensor becomes:

$$\begin{aligned} \text{tr}(\boldsymbol{\sigma}) &= \frac{3k_n \nu}{4\pi \langle r^3 \rangle} \frac{1}{N} \sum_{p=1}^N \left(r_p \sum_{c=1}^{C_p} \delta_c - \frac{1}{2} \sum_{c=1}^{C_p} \delta_c^2 \right) \\ &= \frac{3k_n}{4\pi} \frac{\nu}{\langle r^3 \rangle} \left(\langle \sum_{c=1}^{C_p} \delta_c \rangle \langle r_p \phi_p \rangle - \frac{1}{2} \langle \sum_{c=1}^{C_p} \delta_c^2 \rangle \right) \\ &= \frac{3k_n}{4\pi} \frac{\nu C \langle \delta \rangle_c}{\langle r^3 \rangle} \left(\langle r_p \phi_p \rangle - \frac{\langle \delta^2 \rangle_c}{2 \langle \delta \rangle_c} \right) \end{aligned}$$

where $C = \frac{M_4}{N} = \frac{1}{N} \sum_{p \in N_4} C_p$ is the mean coordination number (or just coordination number, averaged over all particles), $\langle \delta \rangle_c \equiv \frac{1}{M_4} \sum_{c \in M_4} \delta_c$ is the average overlap over all M_4 contacts, of particles with four or more contacts that contribute to the contact network, and we have used the identities: $\langle \sum_{c=1}^{C_p} \delta_c \rangle \equiv C \langle \delta \rangle_c$ and $\langle \sum_{c=1}^{C_p} \delta_c^2 \rangle \equiv C \langle \delta^2 \rangle_c$.

The non-dimensional pressure is defined as $p = \frac{2\langle r \rangle}{3k_n} \text{tr}(\boldsymbol{\sigma})$, so that introducing the normalized particle radius $\xi_p = r_p / \langle r \rangle$ and overlap $\Delta_c = \delta_c / \langle r \rangle$ leads to:

$$p = p(\langle \Delta \rangle_c) = \frac{1}{4\pi} \nu C \langle \Delta \rangle_c (2g_p - b \langle \Delta \rangle_c), \quad (3.13)$$

³A more realistic alternative would be to define it on the plane bisecting the particles in contact and split the overlap accordingly, however, the accuracy gained in doing so would be negligible for small overlaps and similar particle radii.

where the factors are

$$g_p = \frac{\langle \xi_p \phi_p \rangle}{\langle \xi^3 \rangle} \quad \text{and} \quad b = \frac{1}{\langle \xi^3 \rangle} \frac{\langle \Delta^2 \rangle_c}{\langle \Delta \rangle_c^2}.$$

For a monodisperse packing the factor g_p simplifies to 1. In the general polydisperse case, the evaluation of g_p necessitates an integration over the normalized particle size distribution $h(\xi)$ using the *pdfs* of the normalized average normal force $\phi(\xi)$ acting on particles of radius ξ :

$$g_p = \frac{1}{\langle \xi^3 \rangle} \int_0^\infty \xi \phi(\xi) h(\xi) d\xi, \quad (3.14)$$

as discussed in more detail in Ref. [33]. On the other hand, the nonlinear factor b involves the second moment of the normalized normal force distribution function $\langle \Delta^2 \rangle_c / \langle \Delta \rangle_c^2$.

Now we turn our attention to the remaining variable in Eq. (3.13), i.e., the normalized average overlap $\langle \Delta \rangle_c$. We relate it to the volumetric strain under the simplifying assumption of uniform deformation in the packing (non-affine deformations are relevant but go beyond the scope of this study). Given the displacement gradient, $u_{i,j}$, the change of the branch vector of a contact is:

$$dl_i = u_{i,j} l_j, \quad (3.15)$$

where summation is implied over repeating indices and the comma indicates the derivative with respect to the following index, i.e., the j -coordinate. The scalar product with the contact normal corresponds to the change of overlap δ and we assume that for small overlaps the length of the branch vector is equal to $\langle r \rangle$, so that:

$$d\delta = n_i dl_i = \langle r \rangle n_i u_{i,j} n_j \quad (3.16)$$

For an isotropic deformation and contact distribution, as considered in this study, the off-diagonal (i.e., the deviatoric as well as the anti-symmetric) elements of the displacement gradient will cancel in average. Hence, recalling the definition of the normalized contact overlap, $\Delta_c = \delta_c / \langle r \rangle$, one can write:

$$d\langle \Delta \rangle_c = D \epsilon_v. \quad (3.17)$$

where $\epsilon_v = \epsilon_{ii}$ is the trace of the infinitesimal strain tensor defined by $\epsilon_{ij} = \frac{1}{2}(u_{i,j} + u_{j,i})$ and D is a proportionality constant that depends on the size distribution and reflects the non-affinities in the deformation, however, this issue is beyond the scope of this study.

The average normalized overlap $\langle \Delta \rangle_c$ can be obtained by integrating Eq. (3.17), where the integral of ϵ_v , denoted by ϵ_v , is the true or logarithmic volume change of the system, relative to the reference volume V_0 , with corresponding reference volume fraction, v_0 , which we

choose – without loss of generality – to be equal to the critical, jamming volume fraction $v_0 = v_c$, so that:

$$\langle \Delta \rangle_c = D \int_{V_0}^V \epsilon_v = D \epsilon_v = D \ln \left(\frac{V_c}{V} \right). \quad (3.18)$$

Substituting Eq. (3.18) into Eq. (3.13) we obtain for the non-dimensional pressure:

$$p = p_0 \frac{vC}{v_c} (-\epsilon_v) [1 - \gamma_p(-\epsilon_v)], \quad (3.19)$$

where the prefactors are condensed into $p_0 \equiv v_c g_p D / 2\pi$ and $\gamma_p \equiv bD / 2g_p$. The implications of this, e.g., the combination $g_p D$ should not depend on v_c , will be further studied and discussed elsewhere [33].

Note that in our sign-convention, compressive strains are negative – corresponding to decreasing volume with ongoing compression – so that, accordingly, compressive stresses should be negative too. However, we rather use positive compressive stress as above, for the sake of continuity.

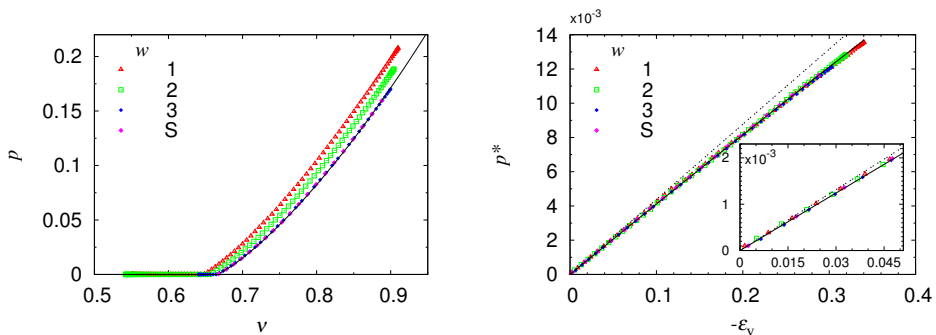


Figure 3.10: The dimensionless pressure as function of the volume fraction (left) (where the solid line is Eq. (3.19), with $v_c = 0.666$ and otherwise using the numbers given in table 3.4 that fit well data-set S with $N \approx 5000$ particles and $w = 3$.) and the scaled pressure as function of the (negative) volumetric strain (right). The solid line is obtained from Eq. (3.20) and the dashed line is the linear approximation. Inset: Zoom into the small deformation regime.

Figure 3.10 shows the non-dimensional pressure as function of volumetric strain, from representative simulations of isotropic deformation for different size distributions. Various other data (not shown, except for one that is indicated by S) using different system sizes and deformation protocols collapse with the same curves – as long as the rate of deformation is small. Interestingly, the scaled pressure

$$p^* = \frac{pV_c}{vC} = p_0(-\epsilon_v) [1 - \gamma_p(-\epsilon_v)], \quad (3.20)$$

is independent of the polydispersity and is well represented by the linear relation in Eq. (3.19), namely $p^* \approx -p_0 \varepsilon_v$, valid for small deformations. The correction factor $[1 + \gamma_p \varepsilon_v]$ is only required for large volumetric strain. The (positive) coefficients $p_0 \approx 0.0418$ and $\gamma_p \approx 0.110$ fit the data well⁴.

Eq. (3.19) now represents the constitutive relation for pressure, from which we can compute, e.g., the bulk modulus of a polydisperse packing, using the definition $B = -V(\partial p/\partial V) = \partial p/\partial(-\varepsilon_v) = v\partial p/\partial v$. Given the dimensionless bulk modulus,

$$B = \frac{\partial p}{\partial(-\varepsilon_v)} = \frac{p_0 F_V}{g_3 v_c} \left[1 - 2\gamma_p(-\varepsilon_v) + (-\varepsilon_v)[1 - \gamma_p(-\varepsilon_v)] \frac{\partial \ln(F_V)}{\partial(-\varepsilon_v)} \right] \quad (3.21)$$

with $F_V = \text{tr}(\mathbf{F}) = g_3 v C$, one has an incremental evolution equation for the dimensionless stress:

$$dp = B(-d\varepsilon_v), \quad (3.22)$$

with the incremental evolution equation for the isotropic fabric:

$$dF_V = F_V \left(1 + v \frac{\partial C}{\partial v} \right) (-d\varepsilon_v), \quad (3.23)$$

where the classical coordination number, $C = (1 - \phi_r(v))C^*(v)$, is an analytically known function of v , see Eqs. (3.3) and (3.4), involving the parameters/coefficients as summarized in Table 3.4.

Note that the above evolution equation for the dimensionless pressure Eq. (3.22), together with Eqs. (3.21), (3.23) and Eqs. (3.3), (3.4), represents the main result of this study that can be easily translated into dimensional pressure and bulk modulus by multiplication with the factor $k_n/(2\langle r \rangle)$. As final remark, the bulk modulus does not explicitly depend on pressure, but F_V does implicitly, hiding the pressure dependence of B . Furthermore, the last term in the bulk modulus involves the derivative $\partial C/\partial v$, which can be very large close the critical density, due to the power $\alpha < 1$, and thus is not negligible. Future work should focus on the validation and comparison of the present approach with experimental data, e.g., concerning the density dependence of pressure and the pressure dependence of B .

⁴The best fit quality (error less than one per-cent for all densities) is obtained when Eq. (3.20) is used to fit the pressure, disregarding the data very close to jamming, i.e., for the best fits, data for $v < v_c + 0.002$ are neglected, since those are hampered by dynamic effects and are thus most unreliable – even when following a very slow unloading procedure (data-set S). Thus we cannot exclude the possibility that the behavior very close to jamming turns out to be different from our results. However, as compared to the very wide range of densities covered, this concerns only a very small regime at very low pressures. The parameter p_0 is of major importance, while γ_p depends on p_0 rather strongly, however, contributing only a small variation to the pressure. Furthermore, fitting power laws proportional to $(v - v_c)^\beta$ to the pressure was not possible over the whole range. For the ranges $0.67 < v < 0.72$ and $0.7 < v < 0.9$ rather good fits lead to power $\beta = 1.21$ and 1.34 , respectively.

3.6 Summary and Conclusion

The transition between fluid- and solid-like phases in idealized, frictionless packings of poly-disperse spheres has been investigated by means of discrete element simulations of isotropic compression and de-compression. As main result, an incremental constitutive relation is given in Eq. (3.22) for the pressure change under isotropic deformation, to be used together with Eqs. (3.21), (3.23) and Eqs. (3.3), (3.4). The pressure evolution equation should be (i) valid for a road range of volume fractions $v \geq v_c$, (ii) should be rather insensitive to (moderate) polydispersity and (iii) involves only analytically known functions of the volume fraction.

The coordination number, i.e., the average number of contacts per all particles, C , is analyzed as function of the volume fraction in order to characterize the state of the granular packing. When the rattlers (i.e. particles with less than four contacts) are disregarded, one obtains the corrected coordination number $C^* \approx C/(1 - \phi_r)$. The fraction of rattlers, ϕ_r , jumps at the jamming volume fraction from $\phi_r = 1$ to ϕ_c and then decays exponentially with increasing volume fraction. Previous studies have shown that the coordination C^* number is discontinuous at the transition and evolves as a power law in the jammed phase close to the critical volume fraction. However, to the authors knowledge, the validity of the power law has not been checked in a broader range up to much higher volume fractions. We fitted an analytical expression of the power law to the simulation data obtained from various packings and confirm that it is not only valid in the neighborhood of v_c but also for very dense packings.

The effect of different system and simulation parameters on the coordination number and the critical volume fraction have been analyzed. We find that changing the polydispersity of the packing causes a shift in the critical volume fraction, i.e., more heterogeneous packings jam at higher volume fractions. However, the power law behavior of the coordination number is not affected by polydispersity. Lowering the deformation rate has the effect of steepening the slope of the coordination number vs. volume fraction curve at the transition, which suggests that the discontinuity will be only achieved in the limit of quasistatic deformation. A study of the effect of deformation rate on the critical volume fraction based on the fit of the power law is unreliable because of the singularity at this point. We recommend that the fit should be used in conjunction with one of the methods proposed in Ref. [40] to determine v_c self-consistently. Finally, we note that varying the deformation rate as well as the system size and deformation history does not have a significant effect on the evolution of the coordination number at high volume fractions: when the rattlers are removed, the power law behavior remains unaffected, at higher densities.

The structure of the contact network plays an important role in determining the mechanical properties of granular materials. In section 3.4 we reviewed previous theoretical predictions regarding the trace of the fabric tensor and compared them with our numerical results. The

Fit parameters for $C(v)$			
jamming volume fraction	v_c	0.66 ± 0.01	variable $v_c(D, w, \dots)$
coordination number at jamming	C_0	6	exact
prefactor for the algebraic coordination number	C_1	8 ± 0.5	variable
power for the algebraic coordination number	α	0.58 ± 0.05	approximate
Fit parameters for $\phi_r(v)$			
fraction of rattlers at jamming	ϕ_c	0.13 ± 0.03	approximate
decay rate of fraction of rattlers	ϕ_v	15 ± 2	approximate
Relation between fabric and contact number density			
polydispersity correction factor	g_3	≥ 1	variable $g_3(w)$
Fit parameters for p			
linear pressure factor	p_0	0.0418 ± 0.001	approximate
non-linear pressure factor	γ_p	0.110	strongly dependent on p_0

Table 3.4: Summary of the coefficients involved in the constitutive relations for the pressure p and the isotropic fabric F_V . In the column right of the symbols are given typical values – some of them are exact, some are fits with a broad spread and some are not changing so much. In the last column some strong dependencies are indicated, e.g., g_3 depends only on the width of the size distribution, w , but not on other variables.

contact number density vC obtained from the simulations and corrected by the factor g_3 , which only depends on the moments of the particle size distribution, as proposed in Ref. [33], is in good agreement with the trace of the fabric tensor, so that $\text{tr}(\mathbf{F}) = g_3 vC^*(1 - \phi_r)$.

Additionally, an incremental expression of the pressure has been derived in section 3.5 based on the micromechanical properties of the particles. The volumetric strain applied to the packing and the isotropic fabric was related to it, thereby enabling us to give an analytical expression for the bulk modulus that includes an evolution term of the isotropic fabric, as specified above. Scaling is observed between the numerical results for different polydispersities when the scaled pressure p^* is plotted against volumetric strain relative to the critical configuration at volume fraction $v = v_c$. We note that the analytical form of the pressure does not explicitly contain a closed power-law relation. The pressure is proportional to the trace of fabric (which contains the power-law relation for the coordination number) and otherwise linear with volumetric strain – involving a rather small quadratic correction for very large strains.

In this chapter we only considered isotropic deformations applied to frictionless packings of

spheres. The natural next steps are to also apply deviatoric (or shear) strain and to include friction and other material parameters. The former will lead to structural anisotropy, while the latter allows to study the effect of various contact properties – like friction – on the evolution of the fabric and the stress. The evolution of, not only, pressure but also of deviatoric stresses is related to the anisotropy of the structure, see the 2D observations in Refs. [80, 81] and the more recent results in 3D, [31, 32], which also confirm that the scaling relation of the fabric – as observed here without friction – holds also in the presence of friction [82, 84].

We note that the jamming volume fraction v_c (e.g. under cyclic loading) is not a constant, but depends on the history of the packing. This issue was not addressed in this study, but will be subject to future research.

Finally, the relations proposed in this study should be compared to experimental data in order to test their predictive value. For example, the pressure dependence of the bulk-modulus is a measurable bulk property, whereas the fraction of rattlers and the isotropic fabric are usually not easily available experimentally.

Acknowledgements

Financial support from the Delft Platform for Computational Science and Engineering is gratefully acknowledged as well as support from the research programme of the “Stichting voor Fundamenteel Onderzoek der Materie (FOM)”, which is financially supported by the “Nederlandse Organisatie voor Wetenschappelijk Onderzoek (NWO)” (project number 03PGM15). We thank N. P. Kruij and K. Bertoldi for helpful comments and discussions.

3.A Determination of the critical volume fraction^{*}

Abstract

The jamming transition in granular packings is characterized by a sudden change in the coordination number. In this work we investigate the evolution of coordination number as function of volume fraction for frictionless packings of spheres undergoing isotropic deformation. Using the results obtained from Discrete Element Method simulations, we confirm that the coordination number depends on volume fraction by a power law with exponent $\alpha \approx 0.5$ above the critical volume fraction and up to

^{*}Published as F. Göncü, O. Durán, and S. Luding. Jamming in frictionless packings of spheres: determination of the critical volume fraction. In M. Nakagawa and S. Luding, editors, *Powders and Grains 2009: Proceedings of the 6th International Conference on Micromechanics of Granular Media*, 13-17 July 2009, Golden, Colorado, pages 531–534. AIP, 2009

rather high densities. We find that the system size and loading rate do not have an important effect on the evolution of the coordination number. Polydispersity of the packing seems to cause a shift in the critical volume fraction, i.e., more heterogeneous packings jam at higher volume fractions. Finally, we propose and evaluate alternative methods to determine the critical volume fraction based on the number of rattlers, the pressure and the ratio of kinetic and potential energies. The results are all consistent with the critical volume fractions obtained from the fits of the power law to the simulation data.

3.A.1 Introduction

A common property of materials like molecular liquids, colloids, foams or granular materials is that they have an amorphous structure and they behave like a solid when either temperature or applied shear force is decreased or volume fraction is increased. The transition from fluid to solid-like behavior in disordered states is generally referred to as jamming. Liu and Nagel [77] have proposed a “jamming phase diagram” to unify this concept for different materials with temperature, volume fraction and applied shear stress as control parameters. For athermal systems such as granular materials, temperature has no effect and at zero applied shear stress, there is a well defined point on the volume fraction axis at which jamming first occurs [114]. The objective of this study is to gain a better understanding of this critical volume fraction, the effect of various system parameters on it and how to best identify it.

In particular, we analyze the coordination number as function of the volume fraction which is discontinuous at jamming and evolves as a power law above the critical volume fraction [92, 113, 114]. We perform DEM simulations of isotropic compression in frictionless packings of spheres. We vary system properties such as the number of particles, polydispersity and loading rate.

3.A.2 Simulation setup

The Discrete Element Method [18, 83, 84] is used. Frictionless spherical particles are enclosed in a cubic volume with periodic boundary conditions. A linear viscoelastic contact model defines the particle normal contact forces. Besides the damping at the contact, an artificial background dissipation is introduced to reduce dynamical effects. Furthermore, in all simulations we neglect gravity. Typical values of the simulation parameters are: system size $N = 1000, 5000, 10000$ particles, density $\rho = 2000$ [kg/m³], elastic stiffness $k_n = 5000$ [N/m], particle damping coefficient $\gamma = 1000$ [kg/s], background dissipation $\gamma_b = 100$ [kg/s] (see Ref. [83] for a discussion of the units). The contact duration of two average particles

is $t_c = 0.64$ seconds in these units and the coefficient of restitution is $r = 0.92$. Polydispersity is measured by the width $w = r_{max}/r_{min}$ of the uniform particle radius distribution. Typical values of w are 1, 2 and 3. Note that $w = 1$ corresponds to a monodisperse packing. The (average) loading rate is defined as the ratio of relative volume change over the total simulation time. Since we are interested in relative rates for identical deformations, we use instead $D = T_{ref}/T_{sim}$ where T_{ref} is the simulation time of the fastest simulation which is 1000 seconds. Typical values of D are 0.1, 0.5 and 1.

3.A.3 Effect of system size

Figure 3.11 shows the evolution of coordination number C including rattlers, i.e. the particles without contacts, for polydisperse packings ($w = 3$) with different sizes. Frictionless particles cannot be mechanically stable unless they have at least 4 contacts. Therefore we define as rattlers those particles having less than 4 contacts. The evolution of the corrected coordination number C^* which excludes rattlers is given by:

$$C^*(v) = C_0 + A \left(\frac{v}{v_c} - 1 \right)^\alpha \quad (3.24)$$

where v_c is the critical volume fraction and C_0 corresponds to the isostatic limit [114, 143] which is $C_0 = 6$ for 3D and $C_0 = 4$ for 2D.

The fluctuations and the finite values of the coordination number C during compression prior to jamming are due to dynamical effects caused by the moving boundaries of the simulation domain. After jamming, these effects are less visible since the ratio between the kinetic and potential energies is much smaller, i.e., $e = E_{kin}/E_{pot} \ll 1$. The strong jump in the coordination number is only clean during decompression at the transition from solid to fluid phase.

The inset of Figure 3.11 shows the fit of Eq. (3.24) to the decompression branch of the simulation data. The critical densities obtained from the fits are 0.6650 ± 0.0002 , 0.6647 ± 0.0002 and 0.6652 ± 0.0001 for $N = 1000, 5000$ and 10000 , respectively. Other parameters are reported in Table 3.5. It is clear that the system size has no significant effect on the critical volume fraction.

3.A.4 Influence of polydispersity

We have performed simulations using three packings of 1000 particles with respective widths of the size distribution $w = 1, 2, 3$. All of the samples were compressed from $v = 0.5$ to $v = 0.9$ and then decompressed. Figure 3.12 shows coordination number as function of the volume fraction for the corresponding packings. The inset shows the fit of Eq. (3.24) to the

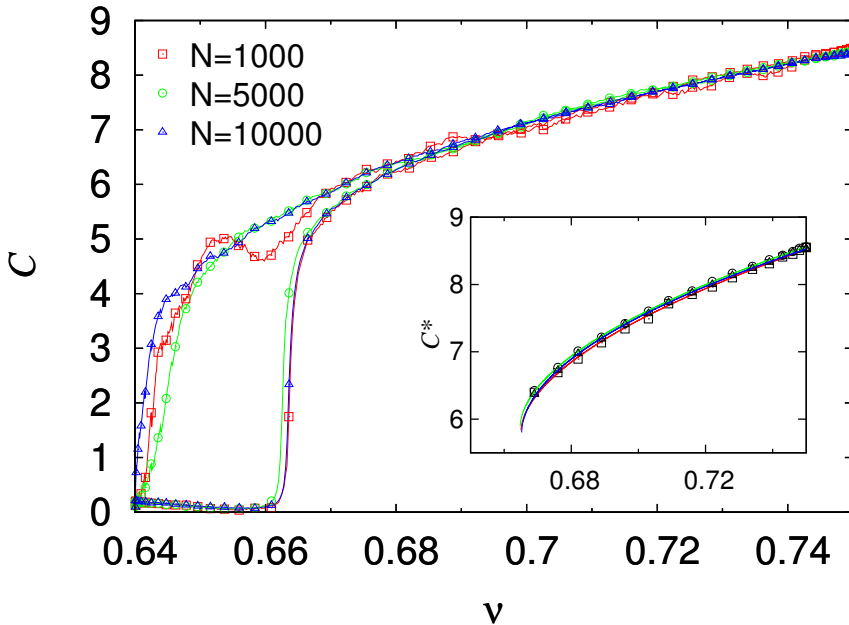


Figure 3.11: Coordination number C as function of density ν for different system sizes. Inset: Fit of Eq. (3.24) to the corrected coordination number C^* computed from the data excluding rattlers recorded during decompression with $D = 0.5$. The red, green and blue lines are the fits of the systems containing 1000, 5000 and 10000 particles, respectively.

decompression branch of the simulation data. The critical volume fractions obtained from the fits are 0.649 ± 0.002 , 0.658 ± 0.002 and 0.671 ± 0.002 for $w = 1, 2$ and 3 , respectively. This indicates that more heterogeneous packings jam at higher volume fractions.

3.A.5 Effect of loading rate

Figure 3.13 shows the coordination number as function of the volume fraction for a polydisperse packing ($w = 3$) of 10000 particles deformed at three different rates. The relative rates of loading are $D = 0.1, 0.5$ and 1 . Jamming occurs at vanishing deformation rates, which is consistent with the observation that the slower the system is deformed, the sharper the transition gets. The evolution of the corrected coordination number and the fits of Eq. (3.24) are shown in the inset of Figure 3.13. It seems that by removal of rattlers the effect of loading rate disappears in high volume fraction. The critical volume fractions obtained from the fits are 0.6648 ± 0.0002 , 0.6652 ± 0.0001 and 0.6654 ± 0.0001 for $D = 0.1, 0.5$ and 1 , respectively. However, these values are questionable since the derivative of Eq. (3.24) has a singularity at ν_c which makes the results very sensitive to the fit range. Consequently, the

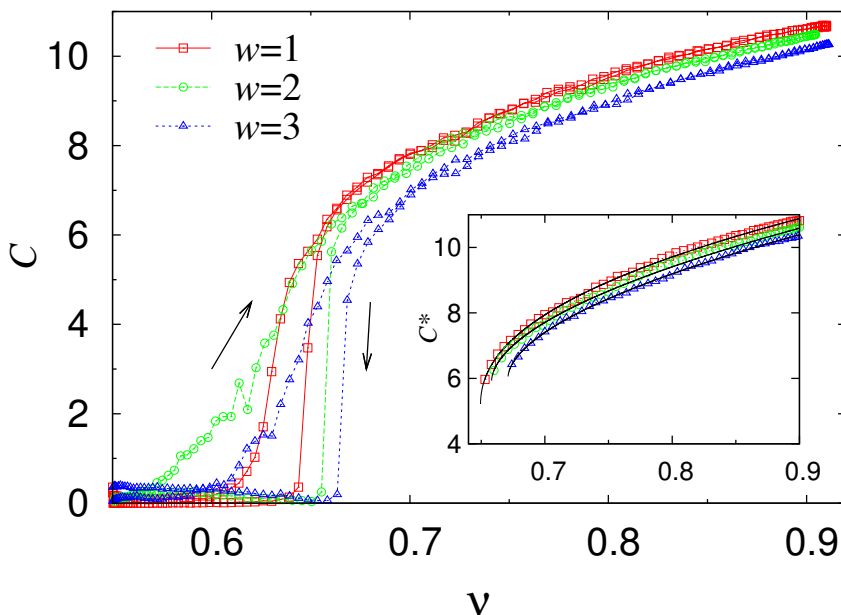


Figure 3.12: The evolution of the coordination number C with the volume fraction v for different polydispersities. The arrows indicate the compression (up) and decompression (down) directions. Inset: The solid lines are the fits of the corrected coordination number C^* according to Eq. (3.24).

exponent $\alpha \approx 0.5$ which is reported in 2D experiments and simulations [92, 113] cannot always be recovered (see Table 3.5). Furthermore, knowing that the rate effects are important close to v_c , using the fit of Eq. (3.24) to analyze the effect of the compression rate might be unreliable. Therefore we propose and evaluate different alternatives.

3.A.6 The fractions of rattlers

An alternative way to determine the critical density v_c at which the jamming transition occurs is to examine the number of rattlers, i.e. particles with fewer than 4 contacts. Typically, it has a reverse behavior to the coordination number, i.e. when C decreases it increases and vice versa. However the number of particles with less than four but more than zero contacts increases or decreases only during the transition. Figure 3.14 shows the evolution of the fraction of particles having different number of contacts during decompression. The critical volume fractions are determined by taking the average of the volume fractions at which the peaks occur in the v - ϕ graphs for the fractions of particles with $0 < C < 4$. The v_c obtained using this method are 0.6634, 0.6623 and 0.6634 for packings with $N = 1000, 5000$

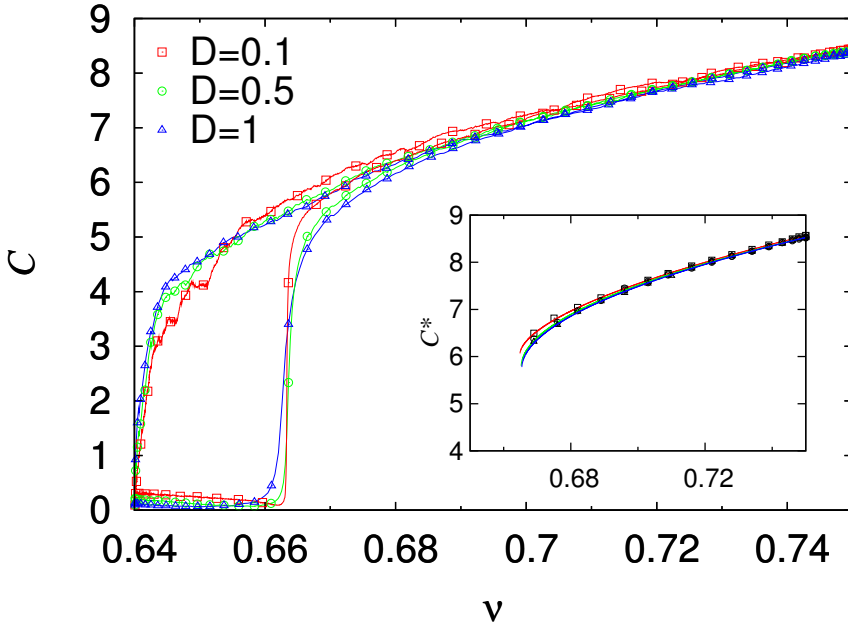


Figure 3.13: Coordination number C as function of density v for different loading rates. Inset: The fits of Eq. (3.24).

N	D	C_0	A	α	v_c	v_c^*	v_c^\dagger	v_c^{**}
1000	0.5	5.8221	8.4875	0.5572	0.6650	0.6641	0.6644	0.6705
	1	5.0256	7.5938	0.3904	0.6650	0.6634	0.6652	0.6669
5000	0.5	5.8838	8.1661	0.5431	0.6647	0.6622	0.6620	0.6658
	1	5.7645	8.2019	0.5279	0.6654	0.6623	0.6624	0.6685
10000	0.1	6.0643	8.4204	0.5909	0.6648	0.6636	0.6624	0.6647
	0.5	5.7887	7.9915	0.5199	0.6652	0.6624	0.6632	0.6665
	1	5.7645	8.2019	0.5279	0.6654	0.6634	0.6627	0.6675

* Obtained from the peaks in the evolution of fraction of rattlers.

† Obtained from the fits of Eq. (3.26).

** Obtained from the intersection points in the $e-v$ graphs.

Table 3.5: Critical volume fractions and fit parameters for polydisperse ($w = 3$) packings obtained from the fits of Eq. (3.24) and alternative methods for different system sizes and loading rates.

and 10000, respectively. These values are close to those obtained from the fits of Eq. (3.24). The advantage of this method is that it can be given a physical explanation. During the transition from the solid to fluid phase, most of the contacts will open and as mentioned earlier

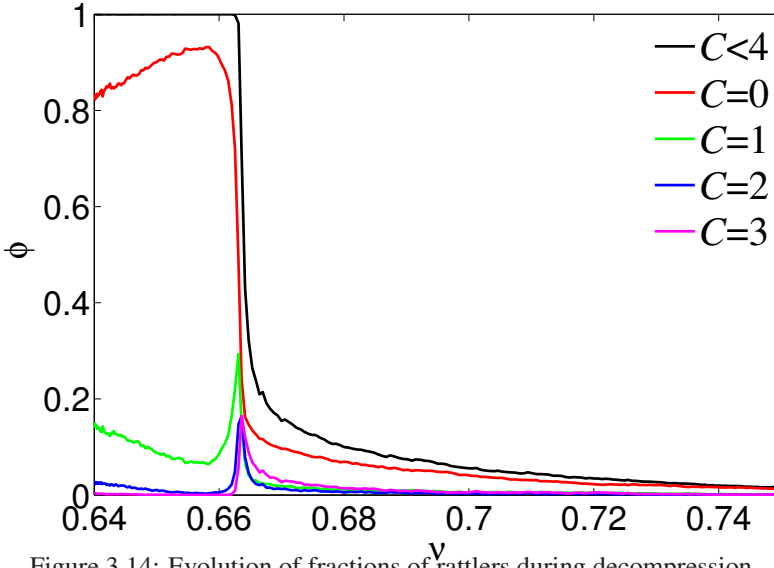


Figure 3.14: Evolution of fractions of rattlers during decompression.

the number of rattlers will quickly increase. However, after the transition the coordination number is normally equal to zero. Therefore, the number of particles with less than four but more than zero contacts will first increase then decrease, which results in the peaks in their fraction.

3.A.7 Pressure

The static pressure p in a packing is obtained from the $(1/3)$ trace of the averaged micromechanical stress:

$$\bar{\sigma}_{ij} = \frac{1}{V} \sum_{c \in \mathcal{V}} f_i^c l_j^c \quad (3.25)$$

where V is the total volume of the packing, l_j^c is the branch vector of contact c and f_i^c is the force associated with the contact. During decompression most of the contacts open at the jamming point and the static pressure drops to zero. Hence, an alternative definition of v_c can be given as the volume fraction at which the pressure vanishes. In order to determine numerical values of v_c we use the relation:

$$\frac{P}{CV} = P_{\text{ref}} \log \left(\frac{v}{v_c} \right) \quad (3.26)$$

where $P = pa_0/k_n$ is the pressure normalized by k_n and the average particle radius a_0 . Figure 3.15 shows the fit of Eq. (3.26) to the simulation data. The critical volume fractions obtained

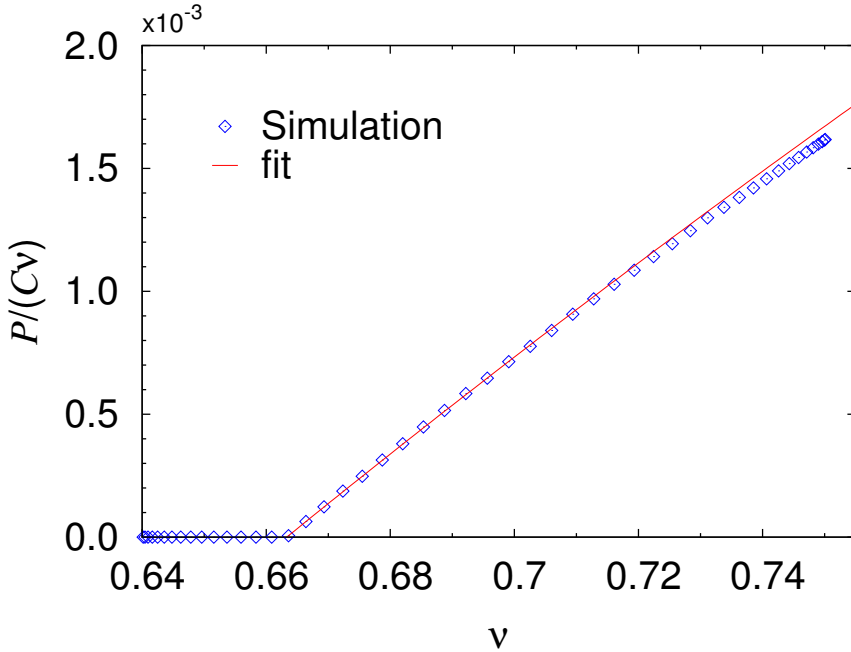


Figure 3.15: $P/(Cv)$ as a function of volume fraction for a polydisperse ($w = 3$) packing.

from the fits are shown in Table 3.5. Note the good agreement between the values obtained from the peaks in the fraction of rattlers and the pressure.

3.A.8 An Energy based criterion

The values of the critical density v_c and coordination number C_0 at the jamming transition can also be obtained from considerations of the ratio of the kinetic and potential energies of the system $e = E_{kin}/E_{pot}$ [83]. We identify the jammed state as the point where the compression branch of the $e-v$ curve crosses its decompression branch (Fig. 3.16). At this point e diverges, which implies a sudden drop in the elastic energy as a clear signature that the unjammed state is reached. This method leads to the expected coordination number $C_0 \approx 6$ which corresponds to the mechanical stability of an isostatic system [114]. The critical volume fractions found using this method are $v_c = 0.652 \pm 0.005$, 0.659 ± 0.005 and 0.6666 ± 0.0006 for polydisperse samples with $w = 1, 2$ and 3 , respectively. The accuracy of this method is limited by the spacing of the data points around the crossing point.

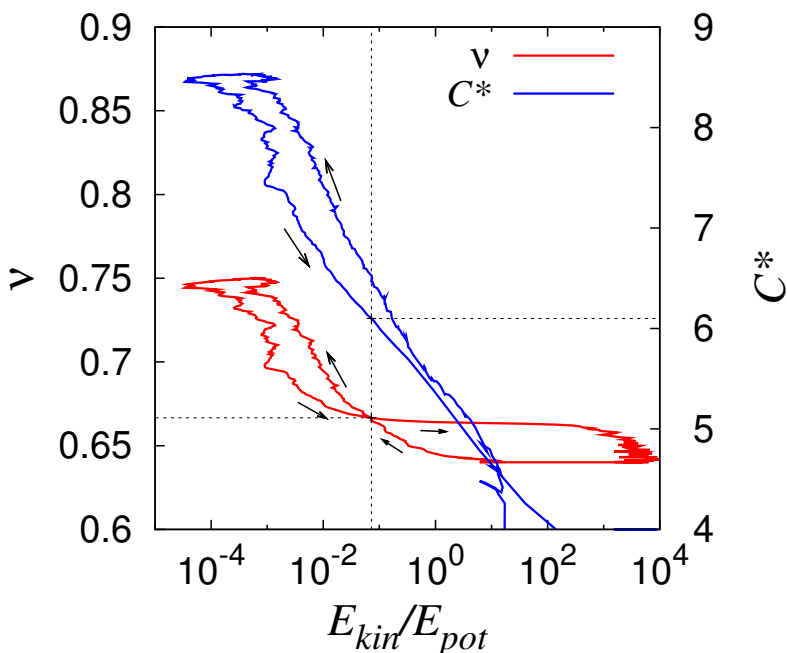


Figure 3.16: Corrected coordination number C^* and volume fraction v as functions of the energy ratio for a polydisperse ($w = 3$) packing of 10000 particles. The arrows indicate the compression (up) and decompression (down) directions.

3.A.9 Conclusions

We have analyzed the effect of different system properties on the critical volume fraction in jamming and the evolution of the coordination number. We find that system size does not have a significant effect on both of these parameters. On the other hand, polydispersity causes a shift in the critical volume fraction, i.e. less homogeneous packings jam at higher volume fractions. We find that the jump in the coordination number becomes sharper as the loading rate is lowered. A more detailed study of the effects of much slower loading rates on the critical volume fraction are required. However, the loading rate has no visible effect on the evolution of the coordination at high volume fractions – after the removal of the rattlers. Finally, we proposed alternative methods to identify the critical volume fraction based on (1) the fraction of rattlers, (2) the energy ratio, and (3) the pressure. A summary of the fits to the power law Eq. (3.24) and the v_c obtained from the proposed methods for different system sizes and compression rates is given in Table 3.5. In conclusion, we recommend to not rely on a single method but, e.g., use the fits to coordination number and pressure in parallel.

Acknowledgements

We thank N.P. Kruyt for helpful comments. Financial support from the Delft Center for Computational Science and Engineering is gratefully acknowledged.

Chapter 4

Effect of particle friction and polydispersity*

Abstract

The macroscopic mechanical behavior of granular materials inherently depends on the properties of the particles which compose them, but it is still unclear how. Using the Discrete Element Method, the effect of particle friction and polydispersity on the macroscopic stress response of 3D sphere packings is studied. The analytical expressions for the pressure, coordination number and fraction of rattlers proposed for isotropically deformed frictionless systems also hold when the interparticle coefficient of friction is finite, however the numerical values of the parameters such as jamming volume fraction change.

The macroscopic response under deviatoric loading is studied with triaxial test simulations. Concerning the shear strength, our results agree with previous studies showing that the deviatoric stress ratio increases with particle coefficient of friction starting from a non-zero value for $\mu = 0$ and saturating for large μ . On the other hand, the volumetric strain does not have a monotonic dependence on the particle friction. Most notably, the maximum compaction is reached at a relatively small value of the coefficient of friction $\mu \approx 0.3$. The effect of polydispersity on the macroscopic stress-strain relationship cannot be studied independent of initial packing conditions. Unlike pressure, the shear strength increases with polydispersity when the initial volume fraction is fixed, but the effect of polydispersity is much less pronounced when

*Based on F. Göncü and S. Luding. Effect of particle friction and polydispersity on the macroscopic stress-strain relations of granular materials. *Acta Geotechnica*, Submitted, 2012

the initial pressure of the packings is fixed. Finally, a hypoplastic constitutive model is calibrated with the numerical test results to ascertain the relation between particle properties and material coefficients of the model.

4.1 Introduction

Understanding the mechanical properties of granular materials and their connection to the microscale particle properties is important for many industrial applications and basic research. Even when grain scale properties such as shape, roughness and elasticity are known it is not straight forward to relate them to the macroscopic constitutive behavior. The main difficulty arises from the discreteness and disorder of granular materials which lead to inhomogeneous and anisotropic contact and force distributions [101, 107].

In general, two types of approaches focusing on different length scales are pursued to model the mechanical behavior of granular materials. Micro-mechanical [57] models consider individual particles and their interactions with the surrounding for example by specifying contact force laws and inter-particle friction. Although this is analytically tractable for a limited number of particles, it is usually implemented numerically in discrete particle methods [18] for useful results. Large scale phenomena and industrial applications of granular materials involve countless particles. Even with the most advanced computational technology of today it is not possible to simulate a nature-scale realistic system following this approach.

An alternative is to assume a granular medium as a continuum and apply the principles of continuum mechanics to obtain macroscopic field variables. Generally numerical methods implementing this approach require comparatively less computational resources. However, besides the lower resolution one has to sacrifice many features of granular materials readily implemented in discrete methods, such as geometric non-linearity due to discreteness, explicit control over particle properties etc. Instead a constitutive model has to be defined typically based on phenomenological observations of the relation between stress and strain. Although, micromechanical parameters are introduced [14, 99, 109] to enhance the models, the main drawback of the continuum approach remains its lack of connection with the microscopic properties of the constituent particles.

The goal of this study is to understand the effect of micro-scale particles properties on the macroscopic mechanical behavior of granular materials. Our approach which is illustrated in Fig. 4.1 tries to combine the advantages of discrete particle simulation and continuum theory. We use numerical simulations as a virtual test facility to systematically characterize the effect of particle properties on the macroscopic mechanical stress-strain relationship of ideal granular packings. In particular, we analyze the effect of particle friction and polydispersity on the macroscopic stress-strain relationship of numerical assemblies subject to isotropic and

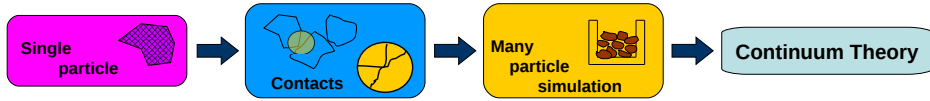


Figure 4.1: From particle simulations to continuum description of granular materials. Schematic illustration of the approach for the development of micromechanically based constitutive models for granular materials using discrete particle methods. In this study we focus on model systems of frictional polydisperse assemblies of spheres.

triaxial loading. Finally we calibrate a hypoplastic constitutive model with the simulation data to characterize the relation between particle properties and the material coefficients of the model.

The manuscript is organized as follows: In section 4.2 we describe the general numerical setup for sample preparation and parameters used in simulations. Next in section 4.3 we present results of isotropic deformation simulations of frictional packings and compare the evolution of the pressure with previously studied frictionless packings with varying polydispersity. Section 4.4 introduces the hypoplastic constitutive model. Following a short description of the numerical test setup, in Section 4.5 we present the results of triaxial test simulations with the calibration of the hypoplastic model for different particle coefficients of friction and polydispersities.

4.2 Simulation setup

The motion of spherical particles with uniformly distributed radii between r_{\min} and r_{\max} was simulated using the Discrete Element Method (DEM) [18]. Linear spring–dashpot contact force laws as function of the overlaps are used to model the interaction of particles in the normal and tangential directions. Artificial background dissipation proportional to the translational and rotational velocities was included to damp dynamics. Friction was modelled according to the Coulomb law involving tangential elasticity, i.e. static friction. Gravity was neglected during all simulations. Numerical values of the parameters used in simulations are presented in Table 4.1.

Cube shape samples were prepared from random granular gases ($\nu = 0.3$) with prescribed polydispersities. The packings were compressed isotropically by moving periodic boundaries until the volume fraction reached the initial value required for subsequent simulations. The boundaries were displaced using a cosine wave function to avoid shocks. They were then relaxed at constant volume fraction to dissipate most of the remaining kinetic energy. Fig. 4.2 illustrates the sample preparation and a typical simulation of an isotropic deformation cycle.

Parameter	Value	Description
N	9261 [-]	Number of particles
$\langle r \rangle$	1 [mm]	Average radius
w	1–5 [-]	Polydispersity parameter $w = r_{\max}/r_{\min}$
ρ	2000 [kg/m ³]	Density
k_n	10 ⁸ [kg/s ²]	Stiffness–normal spring
k_t	2×10 ⁷ [kg/s ²]	Stiffness–tangential spring
	0–100 [-]	Coefficient of friction
γ_n	1 [kg/s]	Viscous dissipation–normal direction
γ_t	0.2 [kg/s]	Viscous dissipation–tangential direction
γ_r	0.01 [kg/s]	Background damping–Translation
γ_{rot}	0.002 [kg/s]	Background damping–Rotation
τ_c	0.64 [s]	Duration of a normal collision for an average size particle

Table 4.1: Summary and numerical values of the particle parameters used in DEM simulations.

It was previously observed [1, 127] that friction has an important effect on the structure and geometry of loose packings generated by compressing random granular gases. The preparation history, which can influence the mechanical behavior of granular packings at later stages, is *not* our aim in this study. However, when studying the effect of friction, we did not entirely disregard it by preparing frictionless samples. Instead, to minimize the effect of friction during the preparation procedure, we used very soft tangential springs, i.e. $k_t/k_n = 0.01$, with the coefficient of friction used in the final simulation. This has no visible consequences for the samples prepared below the jamming density. However, as it will be shown in Sec. 4.5.1, even with soft tangential springs particle friction has noticeable repercussions, e.g. on pressure, at higher densities.

4.3 Isotropic deformations: Evolution of the pressure

Experimental [92] and numerical investigations [1, 114] in 2 and 3 dimensions have shown that pressure along with other quantities such as the coordination number are evolving as a power law of volume fraction in the vicinity of jamming. In our earlier work [41] we derived an analytical expression of the dimensionless pressure $p = \frac{2\langle r \rangle}{3k_n} \text{tr}(\sigma)$ for packings of frictionless polydisperse particles which is applicable to a wide range of volume fractions after jamming:

$$p = p_0 \frac{vC}{v_c} (-\varepsilon_v) [1 - \gamma_p(-\varepsilon_v)], \quad (4.1)$$

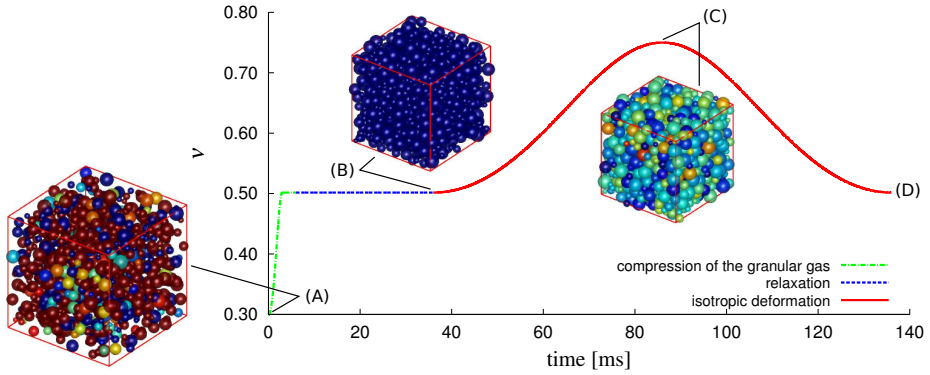


Figure 4.2: Preparation of a sample and isotropic compression-expansion cycle. The initial random granular gas (A) is compressed until the volume fraction reaches the desired value. It is then relaxed at constant volume and used as the initial packing (B) for subsequent simulations. The color of the particles indicates their overlap. Large overlaps are present in the random gas (red particles) whereas in the relaxed packing (blue) particles practically do not touch. The variation in color in the static packing (C) at maximum density is due to well known force-chain inhomogeneity. The data presented later in the manuscript are taken from the branch (C)-(D).

where C is the coordination number, v_c is the critical volume fraction where the pressure drops to zero during unloading, $\varepsilon_v = \ln(v_c/v)$ is the compressive volumetric strain applied to the packing and p_0 and γ_p are fit parameters. The derivation is based on the assumptions that the compacity (contacts per surface area) of the particles is independent of their size distribution and they deform affinely in the assembly. The scaling of the dimensionless pressure by the ratio of inverse contact density and the critical volume fraction, $p^* = \frac{v_c}{vC} p$, indicates that the effect of the polydispersity on pressure is characterized by these quantities. This was also confirmed in simulations [41] for polydispersities up to $w = 3$. Furthermore, we tested the validity of the power law for the coordination number ignoring rattlers, i.e. particles having less than 4 contacts, at high volume fractions:

$$C^*(v) = C_0 + C_1 \left(\frac{v}{v_c} - 1 \right)^\alpha, \quad (4.2)$$

where C_0 is the critical coordination number at jamming, which is equal to 6 in the isostatic limit for frictionless particles, and C_1 and α are fit parameters. The classical coordination number C (taking rattlers in to account) is related to C^* through $C = C^*(1 - \phi_r)$, where ϕ_r is the fraction of rattlers, which we observed to decay [41] exponentially as a function of the volume fraction:

$$\phi_r(v) = \phi_c \exp \left[-\phi_v \left(\frac{v}{v_c} - 1 \right) \right], \quad (4.3)$$

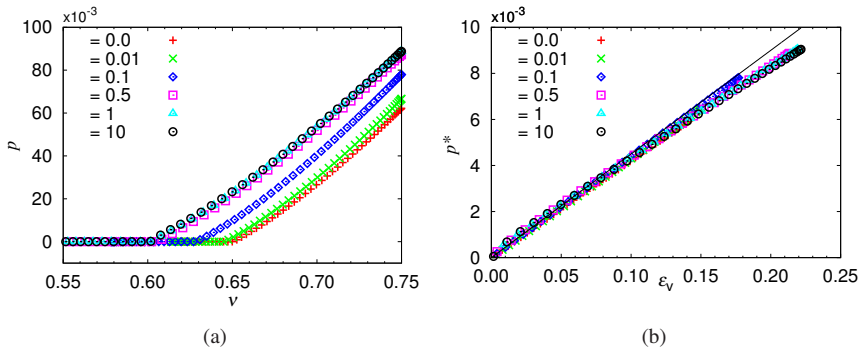


Figure 4.3: (a) Non-dimensional pressure p as function of the volume fraction and (b) scaled pressure $p^* = pv_c/(vC)$ as function of volumetric strain. The points represent simulation data, while the line in (b) is $p^* = -\epsilon_v p_0$ with $p_0 = 0.045$.

where ϕ_c is the fraction of rattlers at jamming and ϕ_v is the rate of decay. In summary, combining Eqs. (4.2) and (4.3) one can express the dimensionless pressure (4.1) merely as a function of the volume fraction.

Next we study numerically the evolution of pressure in isotropically deformed assemblies with varying particle coefficient of friction and fixed polydispersity $w = 1.5$. Samples were prepared, as described in Section 4.2, at a few decimals, i.e. $\Delta v = v_c - v_0 \approx 0.05$, below the estimated jamming volume fractions [86]. The packings were compressed up to $v = 0.75$ and decompressed back to their initial density by imposing a cosine shape displacement on the periodic boundaries. We applied the strains at very low rates in order to approach the quasi-static limit. The maximum average compression rate¹ was $6.33 \times 10^{-6} \tau_c^{-1}$.

Figure 4.3a shows the dimensionless pressures of isotropically expanding² packings as a function of volume fraction for different levels of particle friction. The pressure at a given volume fraction increases with the coefficient of friction and the volume fraction of vanishing pressure v_c decreases with friction [1, 82, 86, 95, 127]. However the effect of particle friction on pressure seems to be limited as the lowest value of v_c saturates around a minimum of ~ 0.60 when μ tends to infinity. Numerical values of v_c are given in Table 4.2 and the procedure to obtain them will be discussed below. In moderately frictionless polydisperse packings v_c is observed to increase with w [41, 112], whereas it is decreasing with friction and rolling resistance [86] as consistent with present data.

The scaled dimensionless pressure is shown in Figure 4.3b. In contrast to previously studied

¹The average compression (expansion) rate is computed as $\frac{\Delta v/V_0}{T_c} = \frac{v/v_0 - 1}{T_c}$ where T_c is the half period of the cosine wave displacement function.

²The data is not shown during compression but during decompression because of artificial dynamical effects in the former, see Chapter 3 for a detailed discussion.

frictionless polydisperse systems, there is *not* a perfect collapse of the data on a single line, which indicates that the effect of particle friction on pressure cannot be assessed solely by the contact density and critical volume fraction. However, the quasi-linear dependence on strain is similar. Nevertheless somewhat stronger non-linearity at low strains is noticeable for large coefficients of friction which causes the quality of the fit of Eq. (4.1) to deteriorate for $v \approx v_c$.

For completeness we also show in Figures 4.4a and 4.4b the coordination number C^* and fraction of rattlers ϕ_r as a function of volume fraction. The critical coordination number $C_0 = 5.95$ of the frictionless packing obtained from the fit of Eq. (4.2) is very close to the theoretically predicted isostatic limit 6. As the particle friction increases C_0 decreases towards 4 (see Table 4.2). The exponential decay function is underestimating the fraction of rattlers close to unjamming for large particle friction. This is due to the fact that the criterion of having less than 4 contact for identifying rattlers is not accurate for frictional particles. About 2.7 % of the particles are rattlers in the frictionless packing (see Table 4.2). Earlier studies have reported about 2 % rattlers for frictionless monodisperse systems [1, 114]. The slightly higher value in our simulation is due to the small amount of polydispersity ($w = 1.5$) present. However, in more polydisperse systems ($w = 3$) we have measured considerably higher percentage of rattlers i.e. $\phi_c \approx 15$ % [41]. We also observe that the decay rate is decreasing as the particle coefficient of friction is increasing which is in line with the expectation that frictional packings are more likely to contain a higher number of rattlers.

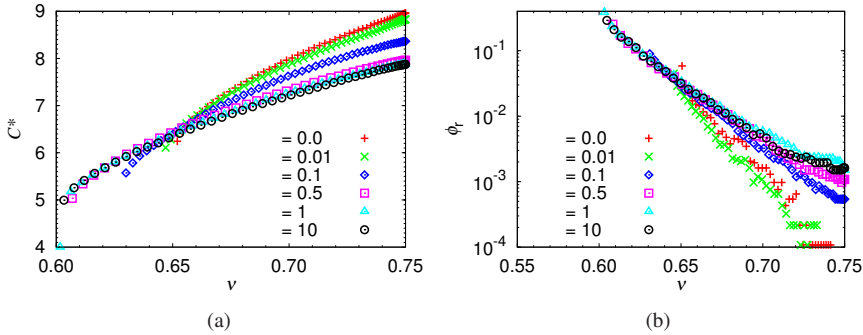


Figure 4.4: (a) Coordination number excluding rattlers as function of the volume fraction for different particle friction coefficients. (b) fraction of rattlers i.e., particles with less than 4 contacts for different particle friction coefficients.

The analytical expressions (4.1), (4.2) and (4.3) of the pressure, coordination number and fraction of rattlers respectively, all depend sensibly on the critical volume fraction v_c . Therefore, it cannot be obtained from the fits as a parameter but must be determined independently. During isotropic decompression, v_c corresponds to the volume fraction where the pressure vanishes and the system loses its mechanical stability [1, 114]. We expressed this with an energy criterion which states that v_c is the first point on the volume fraction axis where the average elastic energy per particle drops below 10^{-5} J. Note that there is not a precise definition of v_c and other authors [1, 40, 41, 114] have used similar criteria to quantify v_c . The numerical values of the fit parameters based on two alternative ways to determine v_c are given in Table 4.2.

We studied the evolution of pressure in isotropically deformed frictional packings prepared with soft tangential springs $k_t/k_n = 0.01$. Interestingly, the equations for pressure, coordination number and rattlers originally proposed for frictionless systems also hold for finite particle coefficient of friction. We note that, the prefactor p_0 is practically constant thus independent of μ , which to our knowledge, has not been predicted theoretically before.

4.4 Hypoplastic constitutive model

As pointed out earlier, a continuum mechanical description of granular materials disregards their discrete nature and focuses on the macroscopic relation between stress and strain. Constitutive models for the plastic deformation of granular materials have been typically developed in the framework of elasto-plasticity [30] which requires a yield surface defined in the principal stress space and a flow rule to determine the direction of plastic strain. More re-

v_c	C_0	C_1	α	ϕ_c	ϕ_v	p_0	γ_p
Energy							
0.0	0.650398	5.95	8.66864	0.564006	0.0279498	40.8483	0.0426764
0.01	0.645326	5.85143	8.67609	0.589765	0.0315906	44.7492	0.0425174
0.1	0.628376	5.24548	7.86626	0.555507	0.0878169	30.5329	0.0441431
0.5	0.605821	4.79637	7.09622	0.556709	0.165372	22.9449	0.0457791
1	0.602273	4.74645	7.10161	0.573719	0.160048	20.3431	0.0458183
10	0.600852	4.68995	7.21218	0.583461	0.179706	21.7361	0.0458584
Extrapolation							
0.0	0.65061	5.98666	8.71241	0.57228	0.024954	37.712	0.0430512
0.01	0.645535	5.88486	8.72471	0.598073	0.0311361	44.7637	0.0428741
0.1	0.628693	5.29016	7.89115	0.564783	0.0864746	30.5483	0.0446279
0.5	0.605661	4.77934	7.09557	0.553545	0.166377	22.9389	0.0455771
1	0.601658	4.68681	7.09945	0.562591	0.170988	20.661	0.0450631
10	0.599892	4.60795	7.21727	0.569347	0.19115	21.9078	0.0446971

Table 4.2: Summary of the parameters appearing in the equations (4.2), (4.3) and (4.1) for the coordination number $C^*(v)$, the fraction of rattlers $\phi_r(v)$ and the dimensionless pressure $p(v)$, respectively. The numerical values of all parameters except v_c are obtained from fits to simulation data. The critical volume fractions are extracted from the dimensionless pressure data during decompression where the average potential energy per particle drops below 10^{-5} J. (Energy) or alternatively, by extrapolating the pressure in Eq. (4.1), excluding the data points closest to and below v_c (Extrapolation).

cently, enhanced models based on higher order gradients of the strain tensor and micropolar Cosserat medium with additional degrees of freedom have been recently developed, to address the microstructural effects, see e.g. [131, 132] among others. Alternative formulations based on rate equations were proposed as hypoplastic models [66]. It is claimed that they lead to simpler formulations without explicit recourse to a yield surface or flow rule and are able to capture basic features of granular materials. We choose a variant of these models for subsequent analysis because of their aforementioned advantages and the ability to calibrate the model with a single triaxial test.

A hypoplastic constitutive model $\dot{\mathbf{T}} = \mathbf{H}(\mathbf{T}, \mathbf{D})$ relates [66, 67, 141] the rate of the stress tensor $\dot{\mathbf{T}}$ to itself and the rate of deformation tensor \mathbf{D} , where $\overset{\circ}{\square}$ denotes the objective Jaumann rate. The basic ingredients of hypoplasticity are (i) rate independence, (ii) homogeneity in stress and (iii) objectivity, which is a requirement for all constitutive models. One of the simplest hypoplastic constitutive models, which satisfies these conditions has the form [141]:

$$\dot{\mathbf{T}} = K_1 \text{tr}(\mathbf{T})\mathbf{D} + K_2 \frac{\text{tr}(\mathbf{T}\mathbf{D})\mathbf{T}}{\text{tr}\mathbf{T}} + \left(K_3 \frac{\mathbf{T}^2}{\text{tr}\mathbf{T}} + K_4 \frac{\mathbf{T}^{*2}}{\text{tr}\mathbf{T}} \right) \|\mathbf{D}\|, \quad (4.4)$$

where \mathbf{T}^* is the deviatoric part of the stress tensor. $\|\mathbf{D}\| = \sqrt{\text{tr}\mathbf{D}^2}$ is the norm of the rate of deformation tensor and K_1, K_2, K_3 and K_4 are material coefficients. The first two terms of Eq. (4.4) express the linear elastic part of the model. A decomposition of stress and strain tensors into isotropic and deviatoric parts shows that under simple biaxial conditions the bulk modulus and the anisotropy can be directly related to the coefficients K_1 and K_2 [72].

In order to predict the mechanical behavior of a specific material, a constitutive model needs to be adapted by providing a suitable set of material coefficients which are usually obtained by calibrating the model with experimental data. Results of a single triaxial test are sufficient to calibrate the hypoplastic constitutive model given in Eq. (4.4). The procedure [67, 141] which consists of solving a linear system of equations to find the numerical values of the material coefficients K_1, K_2, K_3 and K_4 is summarized in Appendix 4.A.

4.5 The triaxial test

The triaxial test is a standard laboratory test procedure widely used to measure mechanical properties of soils [67] and other granular materials. The classical experiment typically consists of compressing a cylindrical specimen wrapped in a membrane in axial direction while keeping the lateral stress constant by means of hydrostatic pressure. We have implemented the triaxial test in DEM simulations for a cubic geometry with periodic boundary conditions in order to avoid wall effects. Similar to the experimental setup, the pressure on the lateral walls (i.e. periodic boundaries) is kept constant while applying a monotonically increasing

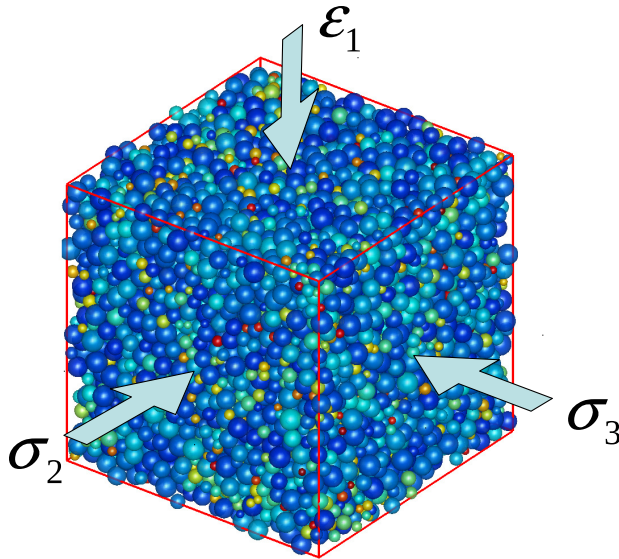


Figure 4.5: Triaxial test simulated with DEM. The boundary conditions are such that the pressure on the side walls is kept constant $\sigma_2 = \sigma_3$ and the strain on top is increased monotonically. The color of the particles indicates the pressure they feel. Shades of red and blue correspond to high and low pressures, respectively.

strain in the third direction. Figure 4.5 illustrates the numerical simulation setup. The average stress of the packing is measured according to the procedure described in [31, 32, 41].

In the following we perform triaxial test simulations with frictional and polydisperse packings and calibrate the hypoplastic constitutive model with the numerical data to understand the relation between material coefficients and particle properties. The initial packings were prepared as described in Sec. 4.2 with different particle friction and polydispersities at volume fractions $v_0 > v_c$.

4.5.1 Friction

Figure 4.6 shows the pressure of the initial samples prepared at $v_0 = 0.70$ from a granular gas with $w = 1.5$ as a function of the particle friction. In accordance with the observations in Section 4.3 the pressure increases with friction and saturates at very high values of μ . However, note that we have used very soft tangential springs ($k_t = 10^6$ [kg/s²], $k_t/k_n = 0.01$) to reduce the effect of friction during the preparation. Nevertheless, it has still a noticeable effect on pressure built-up during initial compression as the difference of pressure for $\mu = 0.01$ and $\mu = 100$ is about 10 %.

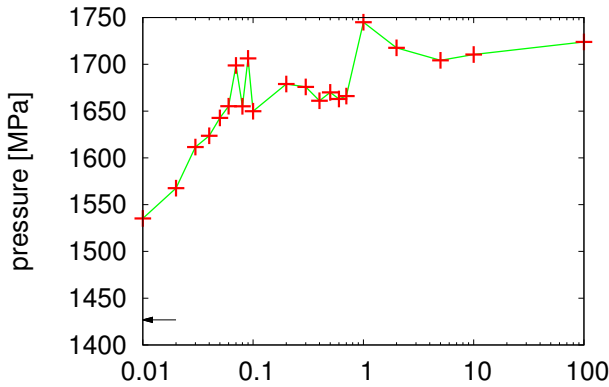
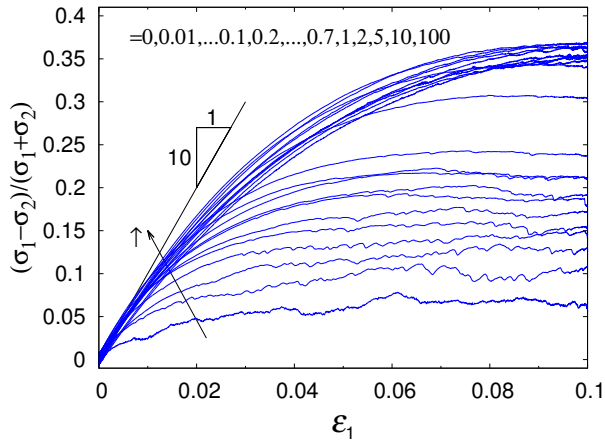


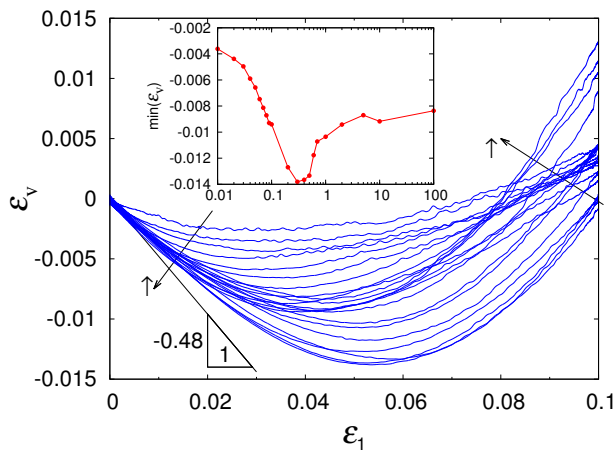
Figure 4.6: Average pressure of the packings ($N = 9261$) as function of particle coefficient of friction for $v_0 = 0.70$ and $w = 1.5$. The pressure of the frictionless packing is indicated by the arrow. The symbols are data, the lines only a guide to the eye.

The results of the DEM triaxial test simulations are shown in Figures 4.7a and 4.7b for the evolution of the deviatoric stress ratio and the volumetric strain. The fluctuations and non-zero values at the initial loading are due to the stress control algorithm which cannot strictly enforce the prescribed lateral stress. For the strain levels applied in the simulations softening after the maximum stress is not observed. However, in a few simulations up to 20 % axial strain the packings with higher particle friction exhibited some softening. In any case the strain levels were not enough to reach the critical state where the stress and volumetric strain have stationary values [125]. The inset of Figure 4.7b shows that the maximum compaction of the packings does not have a linear relationship with the particle friction. It increases with friction and reaches an extremum at $\mu = 0.3$, then decreases and stagnates around $\varepsilon_v \approx -0.009$ for $\mu \geq 1$. The axial strains where the maximum compaction is achieved show a similar trend.

Figure 4.8a shows the macroscopic angle of friction defined by $\varphi_f = \arcsin((\sigma_1 - \sigma_2)/(\sigma_1 + \sigma_2))_{\max}$ as a function of the particle coefficient of friction. It is rapidly increasing and saturates around 21 degrees for $\mu \geq 1$. The percentage of sliding contacts at the peak stress is given in Fig. 4.8b. For large particle friction i.e. $\mu \geq 1$ less than 1 % of the contacts are sliding. This is in agreement with previous experiments [111] and simulations [4, 6, 133]. As shown in Fig. 4.8c the average number of contacts at the peak stress is also decreasing when particle friction is increased. The average contact force is higher in packings with large particle friction because of the lower coordination number and higher macroscopic stress carried by the structure. We also observe that the coordination number of the frictionless packing is practically constant during loading whereas for high friction it decreases linearly with axial strain (data not shown). Finally we note that the macroscopic friction angle is larger than



(a)



(b)

Figure 4.7: Results of DEM triaxial test simulations with different particle coefficients of friction. (a) Deviatoric stress ratio, (b) volumetric strain as a function of axial strain. The inset shows the minimum volumetric strain during axial compression as a function of particle friction.

contact friction angle when $\mu > 0.4$.

We now compare the results of the triaxial tests performed with DEM and calibrated hypoplastic model. Figure 4.9a shows the deviatoric stress ratio and volumetric strain as a function of axial strain for small and large particle friction. The calibrated hypoplastic model captures the stress-strain relationship relatively well, however deviates from the numerical

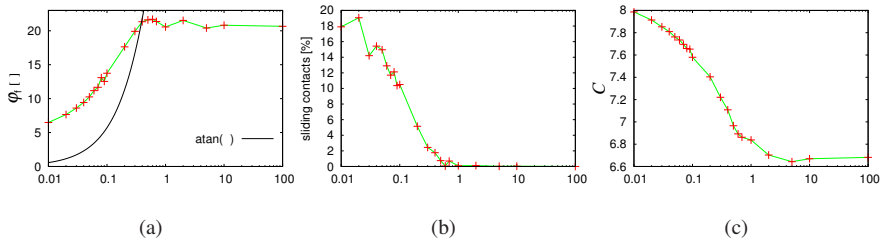


Figure 4.8: Macroscopic angle of friction (a), percentage of sliding contacts (b) and coordination number (c) at the peak stress plotted as a function of particle coefficient of friction.

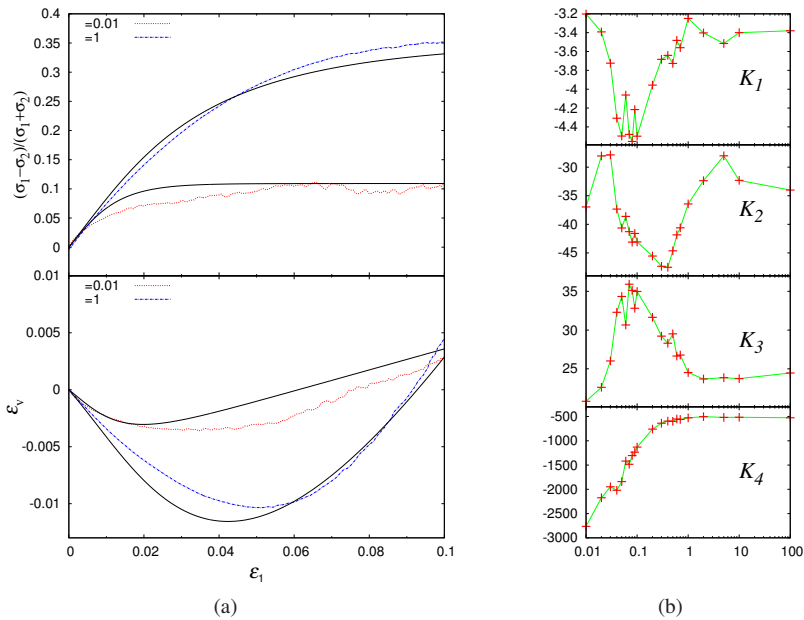


Figure 4.9: (a) Comparison of the triaxial test simulation results of DEM (dashed and dash-dotted lines) and the calibrated hypoplastic constitutive model (solid lines) for $\mu = 0.01$ and 1. (b) Evolution of the material coefficients as function of particle friction.

data over a broad range of volumetric strain when the coefficient of friction is small. Another disagreement between the model and DEM simulations is the longer linear range during initial loading which leads higher stiffness and compactancy. Consequently, the model systematically underestimates the axial strains where the packing starts to dilate. Figure 4.9b shows the relation between the particle coefficient of friction μ and material coefficients K_1, K_2, K_3 and K_4 obtained from the calibration of the model with DEM simulation data. Although the model results are not in perfect agreement with DEM data we can make a few observations.

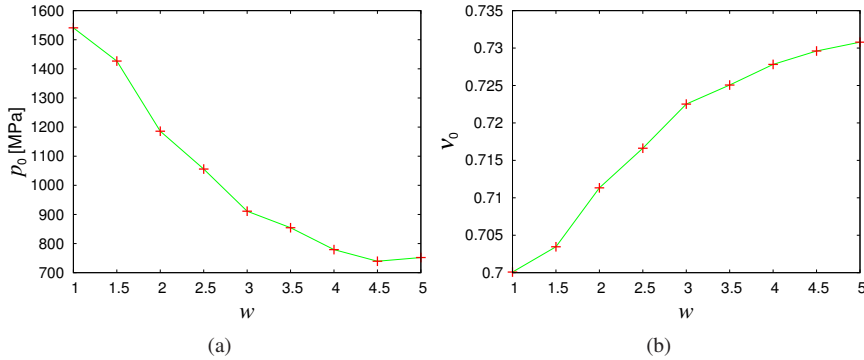


Figure 4.10: (a) Relation between polydispersity w and pressure p in packings with constant volume fraction ($v_0 = 0.70$). (b) Relation between polydispersity w and volume fraction v in packings with constant pressure ($p_0 = 1540.83$ MPa).

First, the numerical values all coefficients seem to saturate at high coefficients of friction i.e. the change for $\mu > 1$ is limited. This is in line with the previously observed limited effect of particle friction on the macroscopic stress-strain relationship for large μ in Fig. 4.7. Next, K_2 reaches its minimum value at $\mu = 0.3$ which coincides with the coefficient of friction of the packing which is most compacted. We also note that K_1 and K_3 have extremal values at $\mu \simeq 0.09$ but we were not able to relate it to any of the microscopic quantities studied here. Finally, the coefficient K_4 which is multiplying the last term of the hypoplastic model, i.e. Eq. (4.4), with the deviatoric stress is strongly correlated with the macroscopic angle of friction.

4.5.2 Polydispersity

An important property of natural granular materials is polydispersity i.e. the size disorder of the grains. In this subsection we study effect of size distribution on the macroscopic stress-strain relationship of granular materials with DEM simulations of the triaxial test. In contrast to subsection 4.5.1, initial samples were prepared at $v_0 = 0.70$ by isotropic compression and relaxation of a *frictionless* granular gas. Figure 4.10a shows the pressure of the samples as a function of the size ratio $w = r_{\max}/r_{\min}$. The results confirm previous studies which have shown that the pressure of frictionless packings at a constant volume fraction decreases with polydispersity [41, 112]. The dependence of the mechanical behavior of granular materials on the initial density and stress level has long been recognized in soil mechanics [7, 68, 141]. The variation of the volume fraction as function of the polydispersity is shown in Fig. 4.10b for another set of initial samples prepared (again without friction) at constant pressure ($p_0 = 1540.83$ MPa). As expected denser packings are needed to achieve a certain level of pressure

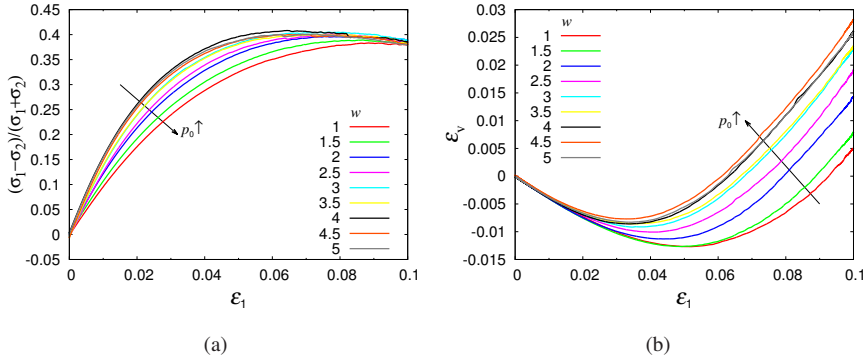


Figure 4.11: Triaxial test simulation results for polydisperse packings of spheres with fixed initial volume fraction $v_0 = 0.70$. (a) Deviatoric stress ratio and (b) volumetric strain plotted against axial strain.

with polydisperse particles.

After the frictionless preparation procedure, the coefficient of friction was set to $\mu = 0.4$ for all polydispersities during the triaxial test simulations. Deviatoric stress ratio and volumetric strain as a function of axial strain are shown in Figures 4.11 and 4.12 for the constant initial volume fraction and constant initial pressure conditions, respectively. When v_0 is fixed the shear strength of the packing increases with polydispersity. Note that the initial pressure which determines the confining stress $\sigma_2 = \sigma_3 = p_0$ is decreasing with polydispersity, see Fig. 4.10a. This is in agreement with laboratory experiments of triaxial test performed at different stress levels which indicate that the macroscopic friction angle decreases with confining pressure [68]. However, as illustrated in Fig. 4.11b, we observe that the “compactancy” angle $\psi_0 = \arctan(\dot{\epsilon}_v / \dot{\epsilon}_1)_{\epsilon_1=0}$ at the initial loading and the dilatancy angle at the peak stress $\psi = \arctan(\dot{\epsilon}_v / \dot{\epsilon}_1)_{\epsilon_1|\sigma_1=\sigma_{1,\max}}$ are practically independent of polydispersity and thus of pressure. The average values are $\psi_0 \approx -21.4^\circ$ and $\psi \approx 34.8^\circ$.

The results of the triaxial test simulations for the packings prepared at constant pressure are shown in Figure 4.12. The effect of polydispersity (and that of the initial volume fraction indirectly) is significantly less visible compared to the case of fixed initial volume fraction. Nevertheless, we still observe that the maximum compaction increases with polydispersity as shown in Fig. 4.12b. Tables 4.3 and 4.4 list the macroscopic angles of friction, the compactancy and dilatancy angles and the calibrated material coefficients of the hypoplastic model for the constant initial volume fraction and constant pressure cases, respectively. Figure 4.13 illustrates the material coefficients scaled with the values corresponding to the monodisperse packing. Remarkably the dependence of all coefficients on polydispersity is the same. When the initial volume fraction is fixed they increase with polydispersity

w	p_0 [MPa]	ϕ_f [°]	ψ_0 [°]	ψ [°]	K_1	K_2	K_3	K_4
1	1540.83	22.49543	-21.18998	33.04488	-4.04089	-52.49076	31.83595	-635.31011
1.5	1426.83	22.87745	-23.53974	32.53466	-4.62523	-64.63187	39.58739	-755.70636
2	1185.86	23.39577	-24.33764	35.57873	-5.25273	-72.51639	45.42480	-846.88653
2.5	1055.82	23.61480	-21.72312	35.33683	-5.58763	-78.61776	46.16641	-881.38010
3	911.014	23.95682	-20.30333	36.15346	-6.22841	-88.75241	50.12968	-965.39575
3.5	854.462	23.67943	-20.43918	36.00398	-6.24474	-86.22269	49.70828	-963.43477
4	779.188	24.09396	-20.03433	33.52743	-7.06777	-109.96195	58.86924	-1130.95892
4.5	739.184	23.67433	-19.17088	36.46762	-6.96138	-93.98721	53.27743	-1050.91184
5	752.058	23.67910	-20.20433	34.20306	-7.03788	-101.93062	56.93340	-1105.46042

Table 4.3: Initial pressures p_0 , macroscopic angles of friction ϕ_f , contractancy ψ_0 and dilatancy ψ angles and calibrated material coefficients of polydisperse packings with constant initial volume fraction $v_0 = 0.70$.

w	V_0	ϕ_f [°]	ψ_0 [°]	ψ [°]	K_1	K_2	K_3	K_4
1	0.70008	22.49527	-21.28796	33.04414	-4.04513	-52.57044	31.94349	-636.66486
1.5	0.70346	22.71975	-23.98075	32.18894	-4.38155	-60.73787	37.69527	-719.80271
2	0.71133	22.91103	-24.38783	31.35850	-4.31862	-62.90054	38.36722	-722.66018
2.5	0.71662	22.92729	-23.03858	31.48031	-4.20785	-60.75263	36.20145	-692.63679
3	0.72252	23.00750	-23.36952	31.22803	-4.30802	-63.39031	37.66598	-715.27426
3.5	0.72506	22.69473	-22.36644	33.19803	-4.02844	-53.68751	32.91812	-642.44591
4	0.72782	22.83221	-23.35456	31.14203	-4.03148	-58.15443	34.90000	-667.14453
4.5	0.72960	22.55928	-22.48739	31.57605	-3.87896	-53.22070	32.20359	-629.29244
5	0.73079	22.34407	-23.44291	31.33758	-3.91703	-52.94555	32.94049	-641.60917

Table 4.4: Initial volume fractions V_0 , macroscopic angles of friction ϕ_f , contractancy ψ_0 and dilatancy ψ angles and calibrated material coefficients of polydisperse packings with constant initial initial pressure $p_0 = 1540.83$ MPa

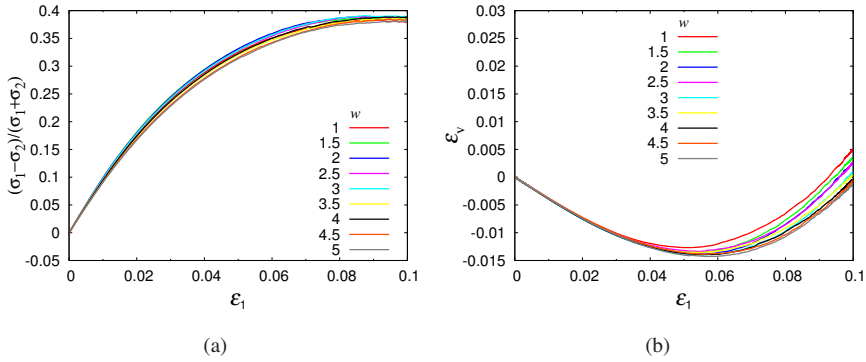


Figure 4.12: Triaxial test simulation results for polydisperse packings of spheres with fixed initial pressure (constant confining stress) $p_0 = 1540.83$ MPa. (a) Deviatoric stress ratio, (b) volumetric strain vs. axial strain.

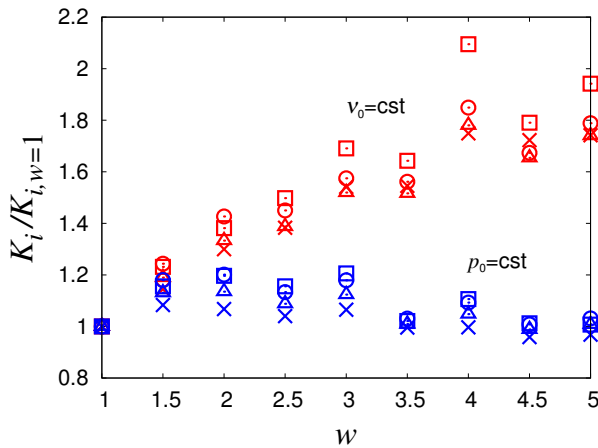


Figure 4.13: Material coefficients K_1 (\times), K_2 (\square), K_3 (\odot) and K_4 (\triangle) of the calibrated hypoplastic constitutive model normalized with the values obtained for the monodisperse packing $w = 1$. Red and blue symbols correspond to the constant initial volume fraction and pressure cases, respectively.

(pressure). On the other hand, the coefficients do not show much variation when the initial pressure is fixed.

4.6 Summary and conclusions

We studied the effect of particle friction and polydispersity on the macroscopic mechanical behavior of sphere packings using the discrete element method. Our results support previous observations on the effect of particle friction in isotropically deformed systems, i.e. the pressure at a given volume fraction decreases with friction and saturates at large values. We also confirm that the critical volume fraction v_c where the packing loses mechanical stability decreases with friction. The scaling of the dimensionless pressure by the ratio of inverse contact number density and the critical volume fraction found for frictionless polydisperse packings also applies although less perfectly close to v_c .

The response of the packings to anisotropic deformations was measured with triaxial tests. An increase in particle friction leads to higher macroscopic friction angles, however the shear strength is bounded and does not increase further for $\mu \geq 1$. The effect of particle friction on the evolution of volumetric strain is more subtle. The angle of compactancy decreases with friction, however, the maximum level of compaction is attained with the packing with $\mu = 0.3$. The axial strain of maximum compaction does not correspond to the strain of maximum stress and displays a non monotonic behavior as function of particle friction. Other microscopic quantities such as the fraction of sliding contacts and the coordination number decrease with increasing friction.

The hypoplastic constitutive model is able to reproduce the basic features of the stress strain relationship of the packings. The quantitative agreement is far from perfect, but qualitatively all features are captured very well. However because of its phenomenological derivation, and the complex interplay of the different deformation modes, it is not possible to link directly the coefficients of the model to the microscopic particle properties. We systematically calibrated the model with DEM simulations in order to clarify the relation between material constants and particle friction. We observe that the fourth coefficient follows a trend similar to the macroscopic angle of friction. The other coefficients have extremal values at various particle friction coefficients corresponding to those of the packings with maximum compaction and initial confining pressure. Their non-monotonous variation with μ reflects the complex influence of the contact friction on the different macroscopic terms in the hypoplastic constitutive relation in Eq. (4.4).

The effect of the polydispersity of the packings cannot be studied independent of the volume fraction or the pressure of the initial samples. When the volume fraction is fixed the pressure decreases as function of polydispersity. The opposite is observed for the volume fraction when the initial pressure is fixed. The shear strength increases with polydispersity for the packings with fixed initial volume fraction. On the other hand, the effect of polydispersity is much less pronounced when the initial pressure is constant.

In conclusion, our results support and confirm previous numerical [4, 6, 133] and experi-

mental [68] studies based on biaxial and triaxial deformation tests. However, an important difference is that in our simulations we have relatively dense packings and soft particles (normal stiffness corresponds approximately to PMMA) and a wide range of particle friction including the frictionless case. In our opinion, this leads to interesting behavior such as the reversal of the maximum compaction after $\phi = 0.3$ which was not reported previously to the authors knowledge.

Systematic variation of the simulation parameters allow to study the effect of micro-scale properties on the macroscopic behavior of granular materials in the spirit of the approach sketched in Fig. 4.1. However, it is difficult to establish a formal relation between the material parameters of a phenomenological constitutive model and microscopic particle properties. Particle simulations can help to identify microscopic mechanisms relevant at the macroscopic scale and facilitate the development of micromechanically based constitutive models for granular materials. The qualitative agreement between DEM and the hypoplastic constitutive model is very encouraging, but the visible quantitative differences could be a sign that an important property, namely the structural anisotropy is missing. The comparison and calibration of an anisotropic constitutive model [87, 91] is in progress.

Acknowledgements

This work has been financially supported by the Delft Center for Computational Science and Engineering. Helpful discussions with V. Magnanimo, N. Kumar, W. Wu and J. Tejchman are appreciated.

4.A Calibration of the hypoplastic constitutive model

The hypoplastic constitutive model given in Eq. (4.4) can be calibrated for a specific material with the results of a triaxial test [67].

Due to the simple geometry of the test setup the stress and strain rate tensors are characterized by their principal components:

$$-\mathbf{T} = \begin{pmatrix} \sigma_1 & 0 & 0 \\ 0 & \sigma_2 & 0 \\ 0 & 0 & \sigma_3 \end{pmatrix}, \quad \mathbf{D} = \begin{pmatrix} \dot{\epsilon}_1 & 0 & 0 \\ 0 & \dot{\epsilon}_2 & 0 \\ 0 & 0 & \dot{\epsilon}_3 \end{pmatrix}. \quad (4.5)$$

As illustrated in Fig. 4.14, the values of $(\sigma_1 - \sigma_2)_{\max}$, the slope ³ E and the angles β_A and β_B

³Due to the fluctuations in the simulation results the stress-strain curves cannot be differentiated easily. In order

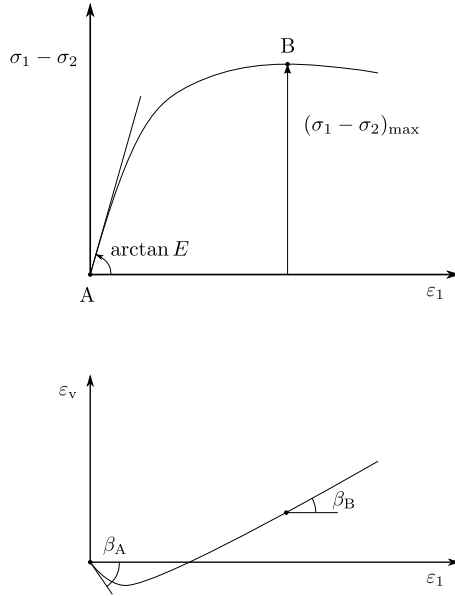


Figure 4.14: Schematic representation of a triaxial test result for the calibration of the hypoplastic constitutive model.

at points A and B can be computed from the test results and are related to **T** and **D**:

$$\beta_{A/B} = \arctan \left(\frac{\dot{\epsilon}_v}{\dot{\epsilon}_1} \right)_{A/B} = \arctan \left(\frac{\dot{\epsilon}_1 + 2\dot{\epsilon}_2}{\dot{\epsilon}_1} \right)_{A/B} = \arctan \left(1 + 2\frac{\dot{\epsilon}_2}{\dot{\epsilon}_1} \right)_{A/B} \quad (4.6)$$

Since the hypoplastic constitutive model is rate independent the magnitude of the strain rate $|\dot{\epsilon}_1|$ can be arbitrary. However, the sign of $\dot{\epsilon}_1$ must be negative due to compression during a conventional triaxial test. Therefore for simplicity $\dot{\epsilon}_1 = -1$ is chosen so that the strain rate tensor **D** at points A and B is:

$$\mathbf{D}_{A/B} = \begin{pmatrix} -1 & 0 & 0 \\ 0 & \frac{1}{2}(1 - \tan \beta_{A/B}) & 0 \\ 0 & 0 & \frac{1}{2}(1 - \tan \beta_{A/B}) \end{pmatrix}. \quad (4.7)$$

The stress tensor **T** at points A and B is known:

$$-\mathbf{T}_A = \begin{pmatrix} \sigma_2 & 0 & 0 \\ 0 & \sigma_2 & 0 \\ 0 & 0 & \sigma_2 \end{pmatrix} \quad \text{and} \quad -\mathbf{T}_B = \begin{pmatrix} \sigma_2 - (\sigma_1 - \sigma_2)_{\max} & 0 & 0 \\ 0 & \sigma_2 & 0 \\ 0 & 0 & \sigma_2 \end{pmatrix}, \quad (4.8)$$

to obtain smooth curves, a fifth order polynomial has been fitted to the data and the slopes have been computed using the fitted curves.

and the stress rates are given by:

$$\dot{\mathbf{T}}_A = \begin{pmatrix} -E & 0 & 0 \\ 0 & 0 & 0 \\ 0 & 0 & 0 \end{pmatrix}, \quad \dot{\mathbf{T}}_B = \begin{pmatrix} 0 & 0 & 0 \\ 0 & 0 & 0 \\ 0 & 0 & 0 \end{pmatrix}, \quad (4.9)$$

where at the point A , $\dot{\sigma}_1 = E\dot{\varepsilon}_1$ since $\dot{\sigma}_2 = 0$ and $\dot{\varepsilon}_1 = -1$.

Substituting \mathbf{D} , \mathbf{T} and $\dot{\mathbf{T}}$ computed at points A and B into Eq. (4.4), the following system of equations is obtained with the unknowns K_1, K_2, K_3 and K_4 :

$$\begin{pmatrix} \text{tr} \mathbf{T}_A D_{1,1}^A & T_{1,1}^A \frac{\text{tr}(\mathbf{T}\mathbf{D})_A}{\text{tr} \mathbf{T}_A} & \|\mathbf{D}_A\| \frac{(T_{1,1})_A^2}{\text{tr} \mathbf{T}_A} & \|\mathbf{D}_A\| \frac{(T_{1,1}^*)_A^2}{\text{tr} \mathbf{T}_A} \\ \text{tr} \mathbf{T}_A D_{2,2}^A & T_{2,2}^A \frac{\text{tr}(\mathbf{T}\mathbf{D})_A}{\text{tr} \mathbf{T}_A} & \|\mathbf{D}_A\| \frac{(T_{2,2})_A^2}{\text{tr} \mathbf{T}_A} & \|\mathbf{D}_A\| \frac{(T_{2,2}^*)_A^2}{\text{tr} \mathbf{T}_A} \\ \text{tr} \mathbf{T}_B D_{1,1}^B & T_{1,1}^B \frac{\text{tr}(\mathbf{T}\mathbf{D})_B}{\text{tr} \mathbf{T}_B} & \|\mathbf{D}_B\| \frac{(T_{1,1})_B^2}{\text{tr} \mathbf{T}_B} & \|\mathbf{D}_B\| \frac{(T_{1,1}^*)_B^2}{\text{tr} \mathbf{T}_B} \\ \text{tr} \mathbf{T}_B D_{2,2}^B & T_{2,2}^B \frac{\text{tr}(\mathbf{T}\mathbf{D})_B}{\text{tr} \mathbf{T}_B} & \|\mathbf{D}_B\| \frac{(T_{2,2})_B^2}{\text{tr} \mathbf{T}_B} & \|\mathbf{D}_B\| \frac{(T_{2,2}^*)_B^2}{\text{tr} \mathbf{T}_B} \end{pmatrix} \begin{pmatrix} K_1 \\ K_2 \\ K_3 \\ K_4 \end{pmatrix} = \begin{pmatrix} -E \\ 0 \\ 0 \\ 0 \end{pmatrix} \quad (4.10)$$

where for clarity the letters A and B have been switched to superscripts when the indicial notation of the tensors is used. The solution to (4.10) can be obtained by simple matrix inversion using linear algebra or well known numerical methods such as e.g. Gauss-Seidel.

Chapter 5

Pattern transformation in a soft granular crystal*

Abstract

We report the results of an experimental and numerical investigation into a novel pattern transformation induced in a regular array of particles with contrasting dimensions and softness. The results indicate new directions for the creation of soft solids with tunable acoustic and optical properties.

5.1 Introduction

It has been realized in recent years that buckling instabilities in elastomeric periodic foams can give rise to counterintuitive pattern switching phenomena [108, 128] with potential for phononic [9, 55] and photonic [147] tunability. An interesting question to ask is whether this richness in behaviour will exist in a broader class of problems.

Ordered arrays of particles are excellent candidates for components of future acoustic, optical and electronic devices and important advances have been reported in the fabrication of such structures at the micro- and nano-scale [47, 65]. Here, we consider the discrete problem of a highly regular array of particles arranged on a two dimensional periodic lattice i.e. a granular crystal (Fig. 5.1a) and we explore its behaviour under uniaxial compression.

*Based on F. Göncü, S. Willshaw, J. Shim, J. Cusack, S. Luding, T. Mullin, and K. Bertoldi. Deformation induced pattern transformation in a soft granular crystal. *Soft Matter*, 7(6):2321, 2011

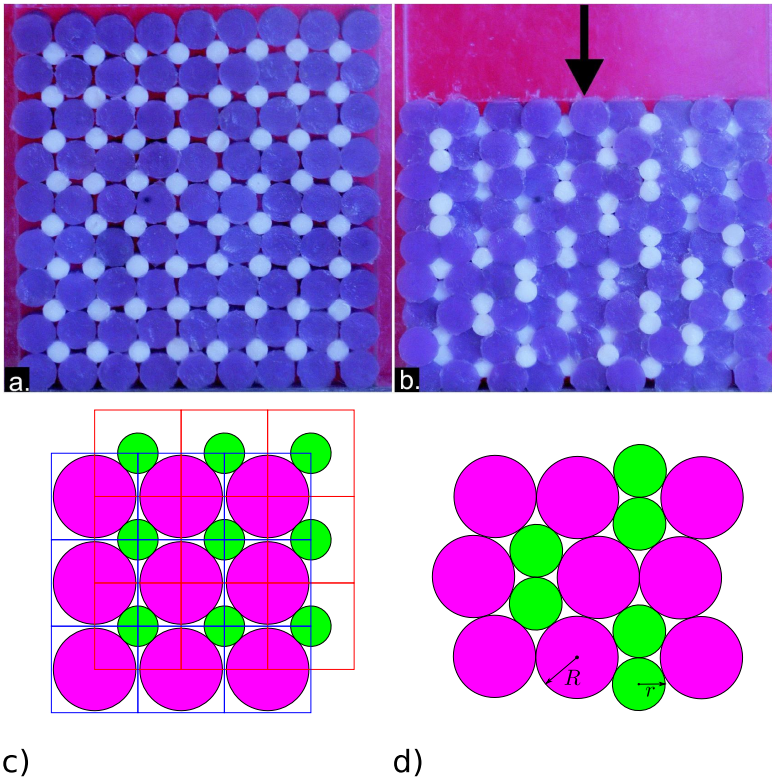


Figure 5.1: (a) Initial configuration of the 2D granular crystal. (b) Deformed configuration of the crystal at 30% uniaxial compression. (c) The initial structure of the crystal consists of two embedded square lattices for small and large particles. (d) The final pattern consists of a vertically aligned pair of small particles surrounded by 6 large ones.

We report the results of an experimental and numerical study of a pattern transformation in a regular array of millimeter-scale cylindrical particles with contrasting dimensions and softness. Under uniaxial compression the system undergoes a rearrangement which leads to a new periodic pattern (Fig. 5.1b). The details of the transformation process depend on the size ratio of the constituent particles but the final state after compression is robust. At small ratios it is homogeneous and approximately reversible i.e. the initial geometry is almost recovered after unloading. In contrast, when the size ratio is increased the same final pattern is reached but now involves the sudden rearrangement of the particles via the formation of a shear band. The robustness of the experimental results and the scalability of the numerical work suggests a way of creating novel soft solids with interesting acoustic and optical properties.

5.2 Experiments

The building blocks of the crystal are two types of cylindrical particles with different dimensions and mechanical properties. Soft particles, which are larger in diameter, are cast from the addition-curing silicone rubber “Sil AD Translucent” (*Feguramed GmbH*, with Young Modulus $E = 360\text{kPa}$) and the “hard” cylinders are machined from a PTFE (Young Modulus $E = 1\text{GPa}$) rod. The average height of soft and hard particles were measured $9 \pm 0.5\text{ mm}$ and $9 \pm 0.02\text{ mm}$, respectively.

The initial configuration consisted of hard and soft particles placed on two embedded square lattices. Each experimental configuration was constructed carefully by hand and repeatability checks were performed on stress/strain datasets. The distances between the particles was such that they touched but were not compressed (see Fig. 5.1c). Focus in the experiments was on investigations of two crystals formed from particles with size ratios $\chi = r/R$ where r and R are the radii of hard and soft particles, respectively. The first one with $\chi = 0.53$ consists of a 7 by 9 array of 2.7 mm radius hard particles embedded in a 8 by 10 array of 5.1 mm radius soft particles. The second one with size ratio $\chi = 0.61$ is a 9 by 9 array of 3.1 mm radius hard particles embedded in a 10 by 10 array of 5.1 mm radius soft particles. The crystals were assembled manually into a PMMA housing with dimensions adjusted to hold the sample in the horizontal and out of plane directions.

Experiments were performed using a 1kN load cell on an “Instron 5569” machine and compression was applied to the top surface of the granular crystal at a constant speed of 1 mm/s up to a strain (ϵ) of 0.25 relative to its original height, with rigid lateral walls. Before each experiment, all cylinders were coated with Vaseline to help reduce friction. For each experiment the stress-strain data was recorded and stored for post-processing and analysis.

5.3 Simulations

The commercial software package Abaqus/Explicit was used to perform the finite element (FEM) simulations. Both large-soft and small-hard particles were modelled as nearly incompressible neo-Hookean [137] solids with Poisson ratio $\nu = 0.49$ and Young’s moduli as mentioned above. Friction between contacting particles was accounted using a Coulomb friction model with $\mu = 0.01$. The simulations were performed under plane stress condition using a quasi-2D mesh to reduce computational cost, and the results match the experimental data reasonably well. Note that out-of-plane displacements are observed during the experiments, making the setup closer to plane stress condition.

In addition to FEM, a 2D soft particle Molecular Dynamics (MD) approach [83] was used to simulate the pattern transformation due to its computational advantage. The force f between

contacting particles is determined by $f(\delta) = k_1 \delta + k_2 \delta^\alpha$, where δ is the geometrical overlap. Numerical values of the fit parameters k_1, k_2 and α ¹ were obtained from contact simulations performed with FEM for ranges of pairs of particles. A Coulomb type friction between particles was used with $\mu = 0.01$. In addition to normal and tangential contact forces artificial damping proportional to the particle velocity was added. It should be noted that the simplification of particle deformations by geometrical overlaps is best suited for small strains where point contacts can be assumed. Furthermore, soft particle MD assumes uncoupled contacts (i.e. the force-overlap relationship does not depend on the number of contacts) which obviously neglects volumetric effects at large deformations. Therefore, this approach may not be appropriate beyond certain particle deformation.

5.4 Results

The pattern transformation is captured both by FEM and MD simulations. Snapshots taken from the experiments, FEM and MD simulations for the small size ratio crystal ($\chi = 0.53$) at intermediate (15 %), maximum (25 %) and zero strain after unloading are shown in Figure 5.2a-i . The pattern transformation in this case occurs gradually and homogeneously over the packing. The full pattern (i.e. the pairing of hard particles) is complete at around 20% deformation and after unloading, the initial square lattice is approximately recovered. Reversible structural rearrangements have been also observed in localized zones of 2D foams undergoing cyclic shear [88]. The stress-strain curves obtained from the experiment and the numerical simulations are shown in Figure 5.2j. The hysteresis in the experimental curve comes from the friction between particles and the PMMA plates which hold the samples in the out of plane direction. Although this was not modelled in the numerical simulations, there is still good quantitative agreement between all sets of results up to 13% compression where the result of MD begins to deviate due to its aforementioned limitation. This affirms the robustness of the phenomena under investigation since each experimental arrangement will contain imperfections at different locations within the crystal. All of the curves are relatively smooth in accordance with the gradual and homogeneous transformation.

For larger size ratio χ , the transformation is inhomogeneous and proceeds through sudden local rearrangements of groups of particles. Snapshots of the experiment, FEM and MD simulations for the $\chi = 0.61$ crystal are shown in Figure 5.3a-i. A rather disordered configuration is reached after unloading, hence the transformation is not reversible for this case. The jumps in the stress in Figure 5.3g are associated with local rearrangements. In particular, the

¹Contact force parameters used in MD simulations for the crystal with size ratio $\chi = 0.51$: *Soft-Soft* $k_1 = 1.3458 \text{ Nmm}^{-1}$, $k_2 = 0.1264 \text{ Nmm}^{-\alpha}$ and $\alpha = 2.9792$, *Soft-Hard* $k_1 = 2.6443 \text{ Nmm}^{-1}$, $k_2 = 0.1816 \text{ Nmm}^{-\alpha}$ and $\alpha = 3.4942$, *Hard-Hard* $k_1 = 3362.8 \text{ Nmm}^{-1}$, $k_2 = 1597.2 \text{ Nmm}^{-\alpha}$ and $\alpha = 2.7198$ and for the crystal with size ratio $\chi = 0.61$: *Soft-Hard* $k_1 = 2.8328 \text{ Nmm}^{-1}$, $k_2 = 0.1274 \text{ Nmm}^{-\alpha}$ and $\alpha = 3.7673$, *Hard-Hard* $k_1 = 3205.5 \text{ Nmm}^{-1}$, $k_2 = 1393.7 \text{ Nmm}^{-\alpha}$ and $\alpha = 2.5769$. See Appendix 5.A for a detailed discussion of FEM contact simulations.

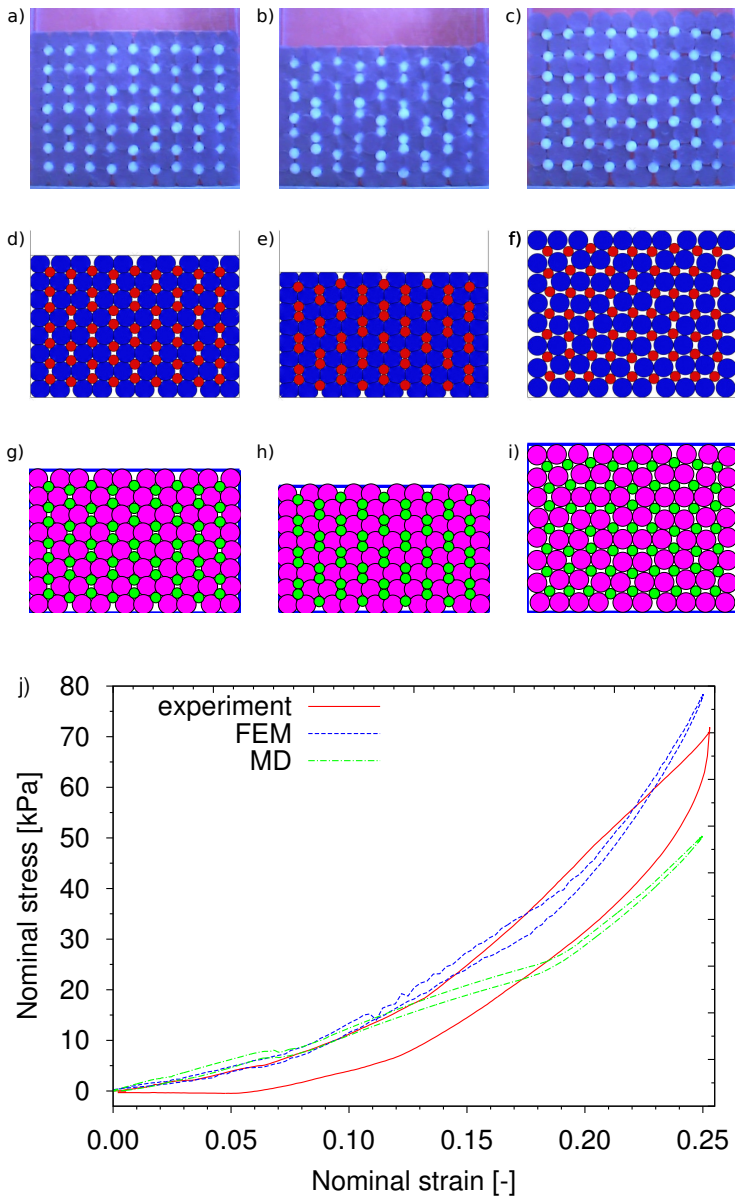


Figure 5.2: Snapshots of the experiment (a, b, c), Finite Element (d, e, f) and Molecular Dynamics simulations (g, h, i) at 15%, 25% strain levels and after unloading for the crystal with size ratio $\chi = 0.53$. The transformation is homogeneous and occurring gradually over the loading phase. (j) Experimental and numerical stress-strain curves.

final state in the experiment is reached after a sudden stress drop at $\sim 16\%$ strain after the reordering of a diagonal structure which is reminiscent of a shear band.

The results of the experiments and the numerical simulations both indicate that the size ratio of the particles changes the qualitative nature of the pattern transformation process whereas the mechanical properties are of lesser importance. Indeed, we have performed FEM and MD simulations where the relative stiffness of the particles $E_{\text{small}}/E_{\text{large}}$ have been varied by three orders of magnitude and find that, for an appropriate size ratio, the characteristic pairing of small particles occurred irrespective of the relative particle stiffness. Moreover, we observe that large values of friction, loading rate or artificial damping can prevent pattern formation. However, small variations of these do not appear to change the qualitative nature of the pattern transformation.

Analytical calculations based on the structure of the crystal [75] before and after transformation and the assumption that both particle types are rigid can be used to provide an estimate of the range of size ratio where a paired pattern can occur. The minimum value $\chi_{\text{min}} = \sqrt{2} - 1$ is determined by the geometry of the initial square lattice such that large particles are touching and the small one in the middle is in contact with its neighbors. In practice, the pattern transformation is unlikely to occur in this situation because small particles are trapped inside the cage of large ones which strictly constrains their mobility. Similarly, the maximum size ratio $\chi_{\text{max}} = 0.637$ is obtained when rigid particles satisfy the connectivity of the patterned state (See Fig. 5.1b,d).

To further investigate the qualitative difference induced by the size ratio, we have performed a series of simulations based on Energy Minimization (EM) [114]. The total elastic energy of the system was computed by adding up the work of the contact forces. For the sake of brevity, we present only the results for three cases which show a qualitatively distinct transformation behavior i.e. quasi-reversible ($\chi = 0.5$), irreversible ($\chi = 0.6$) and transformation leading to another non-periodic structure ($\chi = 1$). We monitored the structural changes of the crystals during loading using the concept of shape factor based on Voronoi tessellation of the particle centers introduced by Moucka and Nezbeda [104]. The shape factor for a Voronoi cell associated with particle i is given by $\zeta_i = C_i^2/4\pi S_i$ where C_i and S_i are the cell's perimeter and surface area, respectively.

A contour plot of the probability distribution of the shape factors for the crystal with size ratio $\chi = 0.5$ over a cycle of loading and unloading is shown in Figure 5.4a. Two distinct branches of high probability shape factors appear gradually as the packing is compressed and upon unloading the branches converge back. At maximum strain, the upper branch at $\zeta \simeq 1.17$ corresponds to the Voronoi cells of the small (hard) particles which are irregular pentagons (at the patterned state). The lower branch which groups cells with shape factor $\zeta \simeq 1.11$ corresponds to the Voronoi cells of the big (soft) particles which are heptagons (not regular; almost hexagons). The symmetry of the branches about 25 % strain axis confirms

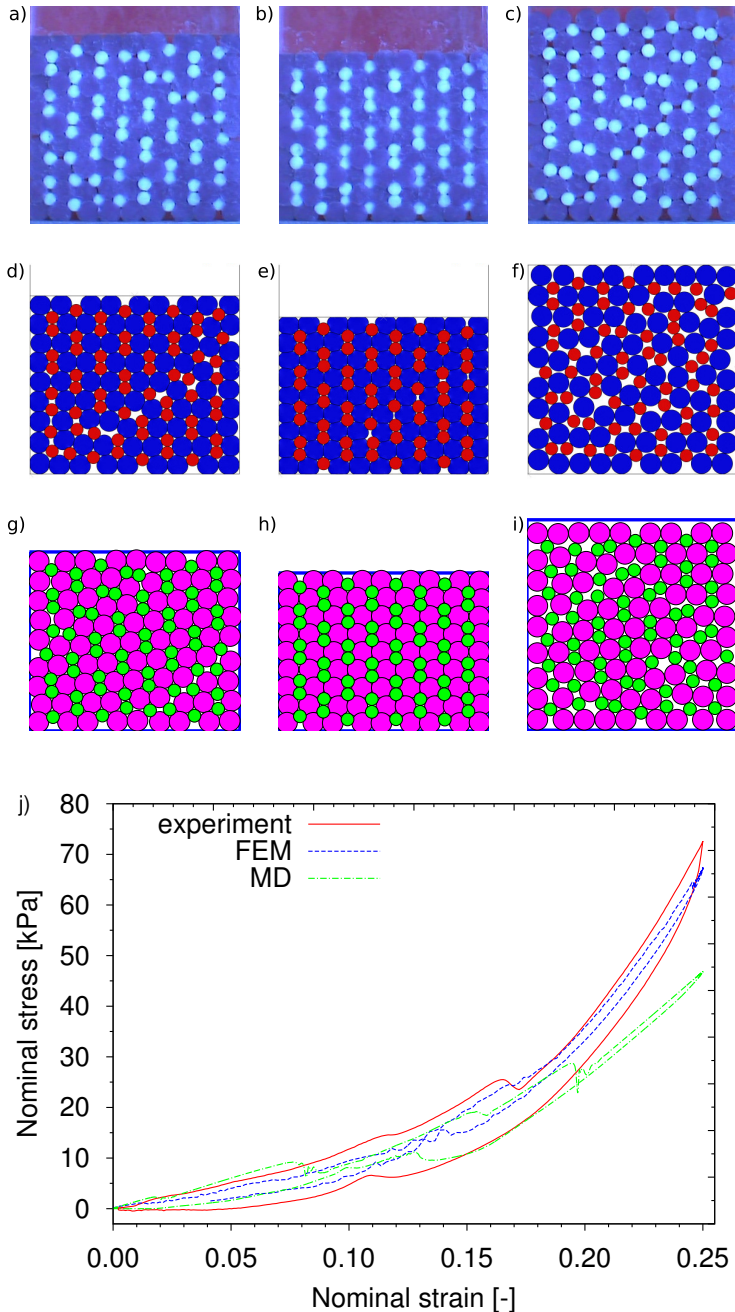


Figure 5.3: Snapshots of the experiment (a, b, c) Finite Element simulations (d, e, f) and Molecular Dynamics simulations (g, h, i) at 15%, 25% strain levels and after unloading for the crystal with size ratio $\chi = 0.61$. The transformation is inhomogeneous and happens as a result of a series of spontaneous local rearrangements. (j) Experimental and numerical plots of the stress-strain data. The drops in the stress correspond to reordering events.

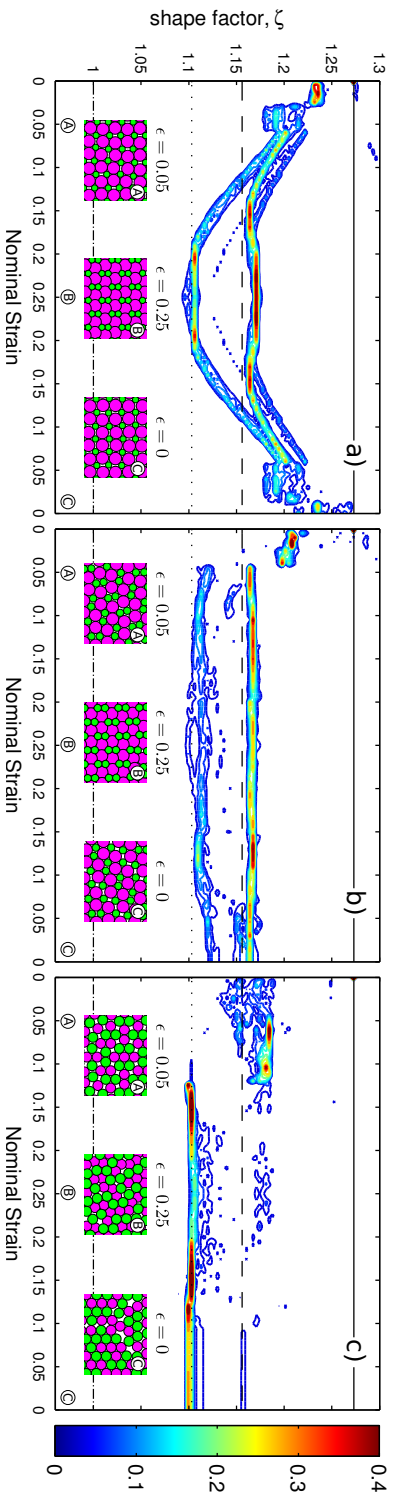


Figure 5.4: Evolution of the probability distribution of the shape factor ζ in minimum energy configurations as function of compression for the size ratios (a) $\chi = 0.5$, (b) $\chi = 0.6$ and (c) $\chi = 1$. The solid, dashed, dotted and dashed-dotted lines denote the shape factors for squares $\zeta = 1.273$, regular pentagons $\zeta = 1.156$, regular hexagons $\zeta = 1.103$ and circles $\zeta = 1$, respectively.

the reversibility of the pattern transformation for this size ratio.

On the other hand, as can be seen in Figure 5.4b, the evolution of the probability distribution of the shape factor ζ for the crystal with $\chi = 0.6$ is significantly different. First, two bands appear spontaneously around $\zeta \simeq 1.16$ and $\zeta \simeq 1.12$ at approximately 5% compression indicating that the characteristic structure of the pattern begins to form very early. Secondly, they remain until the end of the loading cycle. Thus, the transformation for $\chi = 0.6$ is irreversible in contrast with the crystal with size ratio $\chi = 0.5$ where reversibility was found. The evolution of the shape factor distribution for a crystal with size ratio $\chi = 1$ as function of compression is illustrated by the results shown in Figure 5.4c. In this case the crystal develops a non-periodic structure and the deformation is irreversible.

5.5 Conclusions

In conclusion, a combined experimental and numerical study has been used to uncover a novel pattern transformation when regular arrays of macroscopic particles are subjected to uniaxial compression. The reversibility of the transition process only depends on the size ratio of the particles but the final transformed state is robust and it does not depend on the details of its evolution. The work was inspired by bifurcation sequences found in model martensitic transitions [34] at the microscopic level. Connections can also be drawn with energy absorption processes at the macroscopic level in one-dimensional granular crystals which may be considered as shock absorbers and nonlinear acoustic lenses [21, 48, 130]. We believe that the 2D granular crystals studied in the current study combined with pattern transformation can find equivalently interesting applications as tunable phononic devices [9, 59]. Furthermore, we expect that the same mechanism will persist at microscopic scales leading to exciting prospects such as color tuning by mechanical loading [59] and novel applications in photonic crystals [144, 147].

Acknowledgements

The experiments were performed by S. Willshaw and J. Cusack at The University of Manchester. We acknowledge the financial support from the Delft Center for Computational Science and Engineering and the Institute of Mechanics Processes and Control Twente.

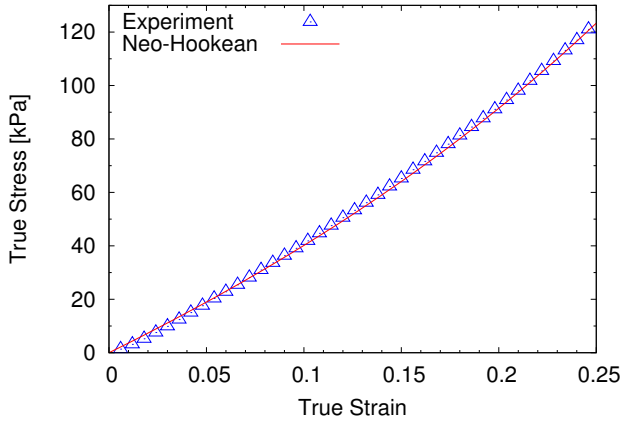


Figure 5.5: Uniaxial compression test of silicone rubber and fit of the neo-Hookean hyperelastic model.

5.A Finite element simulations of contact and pattern transformation

Details of the finite element model and constitutive equation used to simulate contacts between particles and the pattern transformation are given.

5.A.1 Material behavior

Compression tests were performed to characterize the material response of the silicone rubber particles. The specimens were compressed uniaxially at a constant rate up to 0.25 strain. The stress-strain response at 1 mm/s rate of compression is shown in Fig. 5.5.

The observed material behavior is modeled as hyperelastic. Here, we briefly summarize the constitutive model. The strain energy density an isotropic hyperelastic material W is expressed as a function of the invariants of the right Cauchy-Green tensor $\mathbf{C} = \mathbf{F}^T \mathbf{F}$ (or, alternatively those of the left Cauchy-Green tensor $\mathbf{B} = \mathbf{F} \mathbf{F}^T$) where the deformation gradient $\mathbf{F} = \partial \mathbf{x} / \partial \mathbf{X}$ maps a material point from the reference position \mathbf{X} to its current location \mathbf{x} :

$$W = W(I_1, I_2, I_3) \quad (5.1)$$

with

$$I_1 = \text{tr} \mathbf{C}, \quad I_2 = \frac{1}{2} [(\text{tr} \mathbf{C})^2 - \text{tr} \mathbf{C}^2], \quad I_3 = \det \mathbf{C} = J^2, \quad (5.2)$$

and $J = \det \mathbf{F}$ the determinant of the deformation gradient.

The neo-Hookean strain energy density which is special case of the Money-Rivlin model [102, 121] was used:

$$W(I_1, I_3) = c_1(I_1 - 3) + \frac{K}{2}(J - 1)^2, \quad (5.3)$$

where c_1 is related to the elastic modulus and K is the bulk modulus. Note that the model was modified to include compressibility. The Cauchy stress, is given by

$$\boldsymbol{\sigma} = \frac{2}{J} \frac{\partial W}{\partial I_1} \mathbf{B} + \frac{\partial W}{\partial J} \mathbf{I} \quad (5.4)$$

yielding

$$\boldsymbol{\sigma} = \frac{2c_1}{J} \mathbf{B} + K(J - 1) \mathbf{I}. \quad (5.5)$$

Both silicone rubber and PTFE were modeled as nearly incompressible, characterized by $K/G \approx 50$, where G is the initial shear modulus. The initial Young's modulus of silicone rubber was measured to be 360 kPa, so that $c_1 = G/2 = 61$ kPa. Fig. 5.5 shows that the neo-Hookean model captures the stress-strain behavior very well in the strain range of experimental data.

5.A.2 Finite Element Model

The pattern transformation (see Chapter 5) was analyzed using the finite element method where the commercial finite element software ABAQUS/Explicit is used. The boundary conditions of the numerical models aimed to replicate the experimental setup. The PMMA side-wall housing in the experiment is modeled as a rigid body and only the motion of the top plate is allowed during the simulation. Since both finite element (FE) and discrete element (DE) modelings were performed under the 2D assumption, the PMMA front/back-wall housing was not modeled in the simulations. Instead, in FE simulations, the effect of constraint on the out-of-plane degree of freedom (DOF) was investigated by plane strain and plane stress conditions. For plane strain conditions, the displacement in thickness direction (i.e., the out-of-plane direction) was constrained to have no strain through the thickness direction. On the other hand, plane stress conditions release the displacement constraint in the thickness direction, so that the out-of-plane stresses do not develop through the simulations. The DE model is also performed in the 2D assumption, and the simulations can be considered as either plane strain or plane stress depending on the method how the contact force is defined. Since the FEM simulations showed that the experimental conditions were close to the plane stress conditions, the contact forces for DE modelings were estimated based on the plane stress

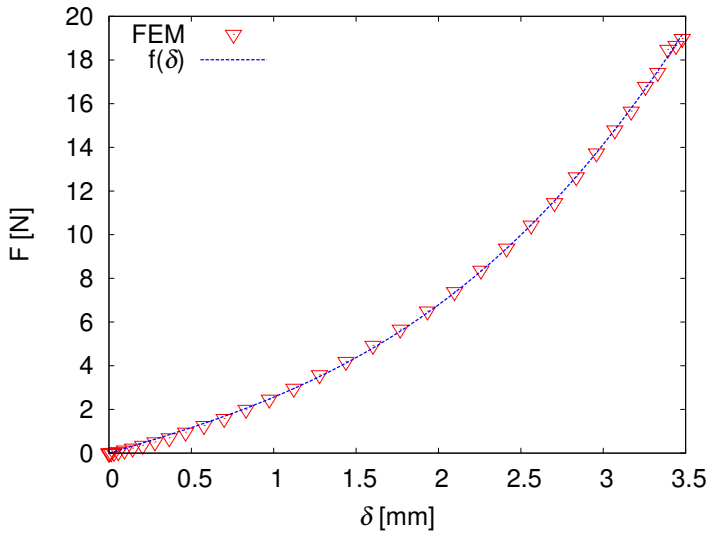


Figure 5.6: Force overlap relation of a 5 mm soft and 3 mm hard particle.

condition of FE models. Thus, all the DE simulations should be considered as plane stress simulation.

The typical length of the mesh was designed to be the length of the thickness dimension, i.e. 0.25mm . The 8-node 3D cubic element with reduced integration points (i.e., C3D8R) was employed. In order to model contact conditions, the friction between all the contacting bodies was modeled by the Coulomb friction model with a friction coefficient of $\mu = 0.01$. When explicit calculations are employed for the exact simulation of the quasi-static experiments, it usually takes very expensive computation time due to the existence of the stable time limit. Thus to perform the analysis in reasonable time, a mass scaling factor of $f_{ms} = 10^4$ was used after confirming the total kinematic energy is less than 1% of the total external work throughout the simulations. Both silicone rubber and PTFE particles were modeled using the neo-Hookean constitutive model introduced in the previous subsection with the material coefficients for silicone rubber $c_1 = 60.9\text{ kPa}$, $K = 6.05\text{ MPa}$, and for PTFE $c_1 = 168\text{ MPa}$, $K = 1.67\text{ GPa}$.

Contact force parameters

The parameters of the contact force model used in discrete element simulations of pattern transformation (cf. Chapter 5) and dispersion relation calculations (cf. Chapter 6) of the granular crystal were determined from finite element simulations of contact. The constitutive model and material properties given in the previous subsections were used. Only half of a

	R_1 [mm]	R_2 [mm]	k_1 [N/mm]	k_2 [N/mm $^\alpha$]	α [-]
Hard – Hard	2	2	3693.4927	1941.8071	3.0181
	3	3	3205.1825	1432.9685	2.5775
	5	2	2761.2961	1596.3658	2.1687
	5	3	3114.6429	1011.8045	2.4750
	5	5	3212.9765	649.4558	2.5665
Soft – Soft	2	2	1.3510	0.6942	3.0370
	3	3	1.4554	0.2565	3.2507
	5	2	1.1149	0.4586	2.3951
	5	3	1.0864	0.4122	2.3791
	5	5	1.3459	0.1265	2.9793
Soft – Hard	2	5	3.4126	2.8023	4.0336
	3	5	3.1614	0.9300	3.7652
	5	2	2.2523	0.3078	2.8921
	5	3	2.8313	0.1215	3.7815
	5	5	2.8624	0.2401	3.4990
Wall – Hard	∞	2	8012.34	15588.4	3.27358
	∞	3	8065.78	6747.28	3.27158
	∞	5	8135.72	2081.98	3.29001
Wall – Soft	∞	2	2.91963	5.64501	3.28119
	∞	3	2.93891	2.43643	3.27949
	∞	5	2.96433	0.748355	3.29851

Table 5.1: Fitted values of k_1 , k_2 and α for different types of contact simulated with FEM.

pair of particles in contact was meshed due to symmetry. The contact force model

$$f = k_1 \delta + k_2 \delta^\alpha, \quad (5.6)$$

was calibrated by fitting it to the force displacement data obtained from FEM simulations with a least square method. Figure 5.6 shows the force-overlap relation of a pair of 5 mm soft and 3 mm hard particles. In order to study the effect of size ratio and material properties of the particles on the pattern transformation contact simulations with several combinations of radii and materials were performed. A list of the calibrated contact parameters is given in Table 5.1. If FEM simulations were not available for a given combination of radius or materials, the contact force model parameters were interpolated from the closest available pairs of particles.

Chapter 6

Phononic band gaps in a two-dimensional granular crystal*

Abstract

*The band structure of a two-dimensional granular crystal composed of silicone rubber and polytetrafluoroethylene (PTFE) cylinders is investigated numerically. This system was previously shown to undergo a pattern transformation with uniaxial compression [Göncü et al. *Soft Matter* 7, 2321 (2011)]. The dispersion relations of the crystal are computed at different levels of deformation to demonstrate the tunability of the band structure which is strongly affected by the pattern transformation that induces new band gaps. Replacement of PTFE particles with rubber ones reveals that the change of the band structure is essentially governed by pattern transformation rather than particles' mechanical properties.*

6.1 Introduction

Wave propagation in materials with periodic microstructures [11] has been studied extensively in the context of photonic and more recently phononic crystals [96]. The attenuation

*Published as F. Göncü, S. Luding, and K. Bertoldi. Exploiting pattern transformation to tune phononic band gaps in a two-dimensional granular crystal. *The Journal of the Acoustical Society of America*, 131(6), 2012

of electromagnetic, acoustic or elastic waves in certain frequency ranges known as band gaps is an important feature of these materials which allows to use them as wave guides or filters [64, 117].

Recent research has focused on the ability to control and tune the band gaps in phononic crystals. Several authors have reported [61, 122, 145] the modification and tuning of the band structure of phononic crystals with external fields. On the other hand, 1D granular crystals (i.e. periodic chains of particles) attracted increasing attention due to their non-linear dynamics arising from tensionless contacts and non-linear interactions between particles. Their non-linear response can be tuned by changing the initial compression of the chain [16, 20, 22], leading to the design of tunable acoustic lenses [130] and phononic band gap materials [10]. Moreover, theoretical studies [52] point out the possibility to control the band gaps of a periodic 2D granular crystal by introducing new periodicities in addition to existing ones.

Here, we investigate numerically the propagation of elastic waves in a 2D bi-disperse granular crystal composed of large (and soft) silicone rubber and small (and stiff) polytetrafluoroethylene (PTFE) cylinders [45]. In the undeformed crystal, particles are placed on two embedded square lattices [Fig. 6.1(a)]. When the system is uniaxially compressed particles rearrange into a new periodic pattern [45] as illustrated in Fig. 6.1(b). We will show that the pattern transformation triggered by deformation can be effectively used to tune and transform the band gaps of the structure. The crystal under consideration consists of 5 mm radius silicone rubber and 2.5 mm radius PTFE particles. Material properties of silicone rubber are characterized by density $\rho_r = 1.05 \times 10^3 \text{ kg/m}^3$, Young's modulus $E_r = 360 \text{ kPa}$, shear modulus $G_r = 120 \text{ kPa}$ and longitudinal speed of sound $c_r^{l0} = 77.1 \text{ m/s}$, while for PTFE one has $\rho_t = 2.15 \times 10^3 \text{ kg/m}^3$, $E_t = 1 \text{ GPa}$, $G_t = 336.2 \text{ MPa}$, and $c_t^{l0} = 1350 \text{ m/s}$.

6.2 Modeling

Particles are modeled as 2D disks in a way similar to soft-particle Molecular Dynamics (MD)[49]. The forces in the normal contact direction are described by a non-linear contact force law as function of the geometric overlap δ [see Figures 6.1(c) and (d)] :

$$f(\delta) = k_1 \delta + k_2 \delta^\alpha. \quad (6.1)$$

The parameters k_1, k_2 and α depend on the radii and mechanical properties of the particles in contact and their numerical values (listed in Table 6.1) are determined by fitting Eq. (6.1) to force-displacement data obtained from Finite Element Method (FEM) simulations of various contacts. For the sake of simplicity, tangential contact forces are modeled with a linear spring of stiffness k_t . Since a parametric study reveals that the magnitude of the tangential stiffness does not have a significant effect on the pattern transformation, here we assume

$k_t/k_n = 0.1481$ based on an estimate by Luding [79], with the linearized normal stiffness, k_n , defined below.

The propagation of elastic waves in infinite periodic lattices has been studied using techniques based on structural mechanics and FEM [58, 97, 119]. Following this approach two contacting particles p and q can be viewed as a finite element [69] with the nodes located at the particle centers. Their interaction is then characterized by a stiffness matrix \mathbf{K}^{pq} which relates the displacements and orientations [Fig. 6.1(c)] $\mathbf{U}^{pq} = [u_x^p u_y^p \theta^p u_x^q u_y^q \theta^q]^T$ to the forces and torques acting on the particle centers $\mathbf{F}^{pq} = [f_x^p f_y^p \tau^p f_x^q f_y^q \tau^q]^T$ such that $\mathbf{F}^{pq} = \mathbf{K}^{pq} \mathbf{U}^{pq}$ in the local coordinate system of the contact defined by the normal $\hat{\mathbf{n}}$ and tangent $\hat{\mathbf{s}}$, see Fig. 6.1(c). For a contact characterized by linear stiffnesses k_n and k_t in normal

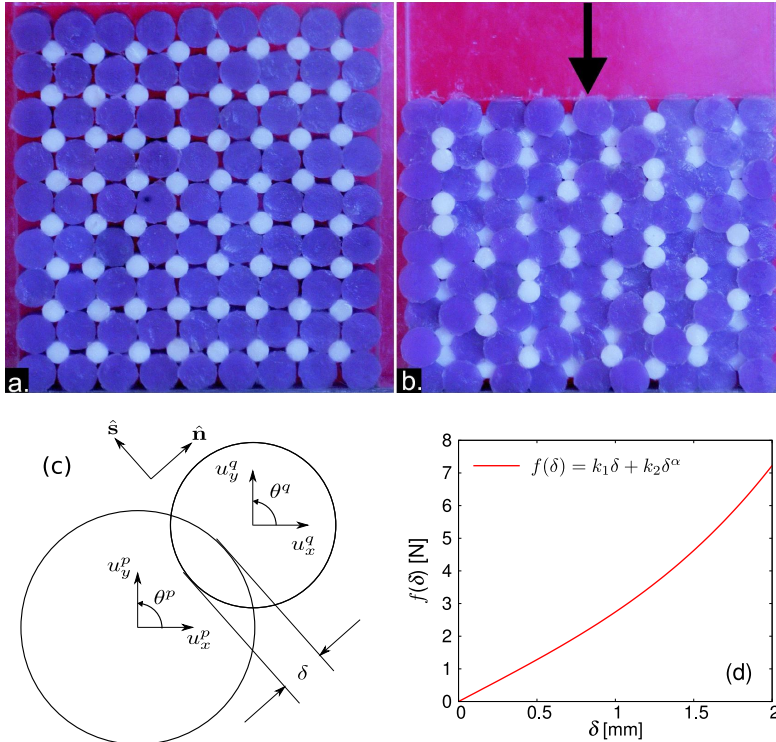


Figure 6.1: (a) Initial undeformed granular crystal and (b) patterned configuration after 25% uniaxial compression, adapted from Göncü *et al.* [45]. (c) Sketch of two particles in contact showing displacements and the geometric overlap δ . (d) Normal contact force as a function of the overlap for a pair of (5 mm) silicone rubber and (2.5 mm) PTFE particles.

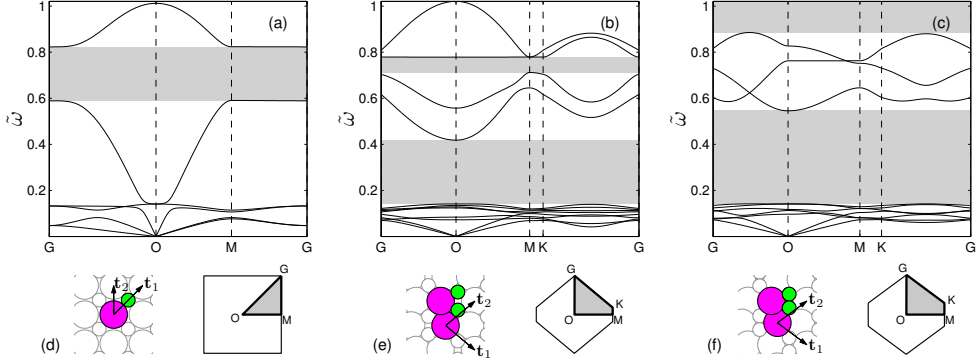


Figure 6.2: Top: Dispersion curves of the bi-disperse granular crystal composed of large rubber (5 mm) and small PTFE (2.5 mm) particles with tangential stiffness $k_t = 0.1481 \times k_n$ at (a) 0%, (b) 15% and (c) 25% uniaxial compression. The vertical axes represent the non-dimensional frequencies $\tilde{\omega} = \omega A / (2\pi c_r^{I0})$ with $A = (||\mathbf{t}_1|| + ||\mathbf{t}_2||) / 2$. Bottom: Unit cells, lattice vectors \mathbf{t}_1 and \mathbf{t}_2 and the first Brillouin zones of the crystal at (d) 0%, (e) 15% and (f) 25% uniaxial compression. The shaded areas indicate the irreducible parts of the Brillouin zones.

and tangential direction, respectively, \mathbf{K}^{pq} is given by[69]:

$$\mathbf{K}^{pq} = \begin{bmatrix} k_n & 0 & 0 & -k_n & 0 & 0 \\ 0 & k_t & k_t R^p & 0 & -k_t & k_t R^q \\ 0 & k_t R^p & k_t R^p R^p & 0 & k_t R^p & k_t R^p R^q \\ -k_n & 0 & 0 & k_n & 0 & 0 \\ 0 & -k_t & -k_t R^p & 0 & -k_t & -k_t R^q \\ 0 & k_t R^q & k_t R^p R^p & 0 & -k_t R^q & k_t R^q R^q \end{bmatrix}, \quad (6.2)$$

where R^p and R^q are the radii of the particles. Note that, since we consider small amplitude perturbations of statically compressed particles with initial overlap δ_0 , Eq. (6.1) can be linearized as

$$f(\delta) \approx f(\delta_0) + k_n(\delta - \delta_0), \quad (6.3)$$

where $k_n = df/d\delta|_{\delta=\delta_0}$ is the linearized contact stiffness.

To compute the dispersion relation we consider an infinite crystal and solve the equations of motion for its periodic unit cell, disregarding effects due to finite systems with walls. Free harmonic oscillations are assumed and periodic boundary conditions are applied using Bloch's theorem [97, 119]. The final form of the equation of motion is of a generalized eigenvalue problem:

$$[-\omega^2 \mathbf{M} + \mathbf{K}] \mathbf{U} = 0, \quad (6.4)$$

	k_1 [N/mm]	k_2 [N/mm $^\alpha$]	α
SR ¹ - SR ¹	1.3459	0.1264	2.9793
SR ¹ - PTFE ²	2.5197	0.2217	3.3028
PTFE ² - PTFE ²	3468	1706.9	2.8147
SR ¹ - SR ²	1.3992	0.4921	3.1357
SR ² - SR ²	1.1018	0.4372	2.3877

¹ $R = 5$ mm

² $R = 2.5$ mm

Table 6.1: Numerical values of contact force parameters k_1 , k_2 and α for pairs of silicone rubber (SR) and PTFE particles.

where ω is the radial frequency of the oscillations. \mathbf{M} and \mathbf{U} are the mass matrix and displacement vector of the unit cell, respectively and the global stiffness matrix \mathbf{K} is assembled from the contributions of individual contacts according to the classical finite element assembly procedure. Note that although this approach assumes a fixed contact network and sliding between particles (i.e. friction) is neglected, it is still valid for this study since small amplitude perturbations superimposed to a given (finite) state of deformation are considered.

6.3 Results

The dispersion diagrams for the 2D granular crystal at different levels of macroscopic nominal strain are provided in Fig. 6.2, clearly revealing the transformation of the band gaps with deformation. In the undeformed configuration the periodic unit cell of the crystal consists of a pair of rubber and PTFE particles arranged on a square lattice (Fig. 6.2(d)) and the structure possesses a phononic band gap for nondimensional frequencies $0.590 < \tilde{\omega} < 0.823$, where $\tilde{\omega} = \omega A / (2\pi c_r^{I0})$ with $A = (|\mathbf{t}_1| + |\mathbf{t}_2|) / 2$, \mathbf{t}_1 and \mathbf{t}_2 being the lattice vectors.

At 15% compression the new pattern starts to emerge and the crystal has a unit cell composed of two pairs of rubber and PTFE particles (Fig. 6.2(e)). The structural transformation alters the dispersion relation of the crystal. Remarkably, a new band gap is open and the structure has now two band gaps at $0.141 < \tilde{\omega} < 0.419$ and $0.712 < \tilde{\omega} < 0.778$ [Fig. 6.2(b)].

The transformation is complete when the PTFE particles touch (Fig. 6.2(f)). Figure 6.2(c) shows the corresponding band structure of the patterned crystal at 25% compression. The stiff contacts between PTFE particles leads to transmission and band gaps at much higher frequencies. At this level of deformation the structure is characterized by three band gaps in the intervals $0.142 < \tilde{\omega} < 0.545$, $0.885 < \tilde{\omega} < 3.557$ (partially shown in Fig. 6.2(c)) and $3.557 < \tilde{\omega} < 19.417$ (not shown in Fig. 6.2(c)).

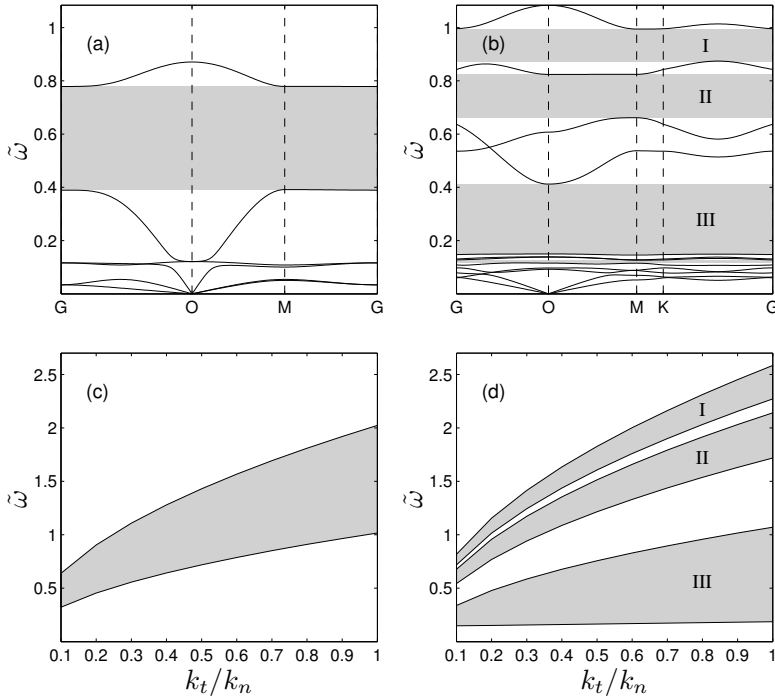


Figure 6.3: Dispersion relation of a soft granular crystal made of rubber particles in the (a) undeformed and (b) patterned state (at 25% compression) with $k_t/k_n = 0.1481$. Evolution of the band gaps in the (c) undeformed and (d) patterned (band gaps marked by I, II and III in Fig. 6.3(b)) soft granular crystal as function of the stiffness ratio k_t/k_n .

Our previous study suggested that the qualitative nature of the pattern transformation mainly depends on the size ratio of the particles [45]. The characteristic pattern was observed to form only when the size ratio $\chi = R_{\text{small}}/R_{\text{large}}$ of the small and large particles is in the range $\sqrt{2} - 1 \leq \chi \leq 0.637$ and the transformation was found to be practically reversible around $\chi \approx 0.5$. Both FEM and MD simulations showed that the material properties of the particles do not play an essential role in the pattern transformation [45]. To investigate the effect of the material properties on the band gaps, we consider a crystal made entirely of rubber, replacing the 2.5 mm radius PTFE particles with rubber ones of the same size. The dispersion curves of the structure in the undeformed configuration and at 25% compression after pattern transformation are shown in Figs. 6.3(a) and 6.3(b), respectively, showing that the band structure is not affected qualitatively by the replacement. However, (i) the band structure is lowered due to the softer particles [Fig. 6.3(a)], and is significantly lowered at large strains [Fig. 6.3(b)] due to the absence of stiff contacts, (ii) the band gap of the undeformed rubber-rubber crystal [Fig. 6.3(a)] is wider than before [Fig. 6.2(a)], and (iii) in the deformed state of the soft structure, an additional narrow band gap is present at low

frequencies.

Finally, we investigate the effect of the tangential stiffness of the contacts on the band structure by varying the ratio k_t/k_n in the crystal composed of rubber-rubber particles, since the tangential stiffness depends on the material properties of the particles and can change when the crystal is further processed (e.g. by sintering [76]). Increasing tangential stiffness k_t leads to higher frequencies, but does not influence the pattern transformation. Focusing on the phononic properties, Figs. 6.3(c) and 6.3(d) show that both width and frequency of the band gaps increase with increasing tangential stiffness.

6.4 Discussion and conclusion

In conclusion, we have shown that the band structure of a 2D bi-disperse soft granular crystal composed of large and small particles placed on two embedded square lattices can be modified considerably by deformation. The structural transformation triggered by compression leads to the opening of new band gaps. When translated to real frequencies the band gap marked with I in Fig. 6.3(b) falls between 5015.8 Hz and 5706.5 Hz, which indicates that the crystal could be used as a tunable filter in the audible range, which makes such crystals promising candidates for applications in acoustics, when tunable band gap materials are needed. In this study we focused on the dispersion relations of infinite regularly patterned granular crystals neglecting damping. Nevertheless, band gaps have been also detected in finite size, viscous systems [58]. Therefore we expect our results to hold also for the finite size, dissipative versions of the granular crystals studied here.

Acknowledgments

F. Göncü and S. Luding acknowledge financial support from the Delft Center for Computational Science and Engineering. K. Bertoldi acknowledges the support from Harvard Materials Research Science and Engineering Center and from the Kavli Institute at Harvard University.

6.A Wave propagation in periodic lattices

A general procedure for the computation of the dispersion relation of mechanical lattices is given as follows [97, 119]:

1. Define reference (unit) cell
2. Define the nodes in the reference (unit) cell
3. Define the connectivity of the nodes including the nodes in the neighbor cells
4. Assemble stiffness matrix for the reference (unit) cell using Bloch's theorem to account for periodicity

The unit cell is the irreducible unit of the lattice which tessellates space by translation along the lattice vectors $\{\mathbf{t}_1, \mathbf{t}_2, \dots, \mathbf{t}_D\}$ in D dimensions. Any cell in the lattice can be indexed with respect to the reference cell by specifying how much it is translated from the origin:

$$\Omega^{\mathbf{n}} = \Omega^{\mathbf{0}} + T\mathbf{n} \quad (6.5)$$

where the index of the cell $\mathbf{n} \in \mathbb{Z}^D$ and $T = [\mathbf{t}_1, \mathbf{t}_2, \dots, \mathbf{t}_D]$.

The nodes $\{\mathbf{x}^1, \mathbf{x}^2, \dots, \mathbf{x}^q\}^{\mathbf{n}} \subset \Omega^{\mathbf{n}}$ denote the centers of the particles which are indexed by their number in the unit cell and the index of the cell they belong to e.g $\mathbf{x}^{(\lambda, \mathbf{m})}$ for the node λ in cell \mathbf{m} .

The connectivity of the nodes is determined by the physical contacts between particles. To assemble the stiffness matrix for the unit cell only the contacts between particles within the cell and neighbor cells need to be specified.

The force acting on the particles is computed from contact forces. A contact between two particles located at $\mathbf{x}^{(\kappa, \mathbf{0})}$ and $\mathbf{x}^{(\lambda, \mathbf{m})}$ is denoted by $(\kappa, \mathbf{m}, \lambda)$ and can be modelled as a fictitious bar or beam element assuming contacts are permanent. The force-displacement relation for two particles in contact is given by:

$$\begin{bmatrix} \mathbf{f}^{(\kappa, \mathbf{0})} \\ \mathbf{f}^{(\lambda, \mathbf{m})} \end{bmatrix} = K^{(\kappa, \mathbf{m}, \lambda)} \begin{bmatrix} \mathbf{u}^{(\kappa, \mathbf{0})} \\ \mathbf{u}^{(\lambda, \mathbf{m})} \end{bmatrix} \quad (6.6)$$

where $K^{(\kappa, \mathbf{m}, \lambda)}$ is the element stiffness matrix composed of symmetric non-negative sub-matrices:

$$K^{(\kappa, \mathbf{m}, \lambda)} = \begin{bmatrix} K_{11}^{(\kappa, \mathbf{m}, \lambda)} & K_{12}^{(\kappa, \mathbf{m}, \lambda)} \\ K_{21}^{(\kappa, \mathbf{m}, \lambda)} & K_{22}^{(\kappa, \mathbf{m}, \lambda)} \end{bmatrix}. \quad (6.7)$$

The equation of motion for a particle is obtained from (6.6) and (6.7):

$$\mathbf{f}^{(\kappa, \mathbf{0})} = M^{\kappa} \ddot{\mathbf{u}}^{(\mathbf{0}, \kappa)} + \sum_{(\lambda, \mathbf{m}) \in \mathbb{B}_{\kappa}} \left[K_{11}^{(\kappa, \mathbf{m}, \lambda)} \mathbf{u}^{(\kappa, \mathbf{0})} + K_{12}^{(\kappa, \mathbf{m}, \lambda)} \mathbf{u}^{(\lambda, \mathbf{m})} \right] \quad (6.8)$$

where $\mathbb{B}_\kappa = \{(\lambda, \mathbf{m})\}$ is a set of nodes (λ, \mathbf{m}) connected to the node $(\kappa, \mathbf{0})$. Now using Bloch's theorem, we apply the condition of periodicity $\mathbf{u}^{(\mathbf{n}+\mathbf{m}, \kappa)} = e^{i\mathbf{k}\cdot T\mathbf{m}}\mathbf{u}^{(\mathbf{n}, \kappa)}$:

$$\mathbf{f}^{(\kappa, \mathbf{0})} = M^\kappa \ddot{\mathbf{u}}^{(\mathbf{0}, \kappa)} + \sum_{(\lambda, \mathbf{m}) \in \mathbb{B}_\kappa} \left[K_{11}^{(\kappa, \mathbf{m}, \lambda)} \mathbf{u}^{(\kappa, \mathbf{0})} + K_{12}^{(\kappa, \mathbf{m}, \lambda)} e^{i\mathbf{k}\cdot T\mathbf{m}} \mathbf{u}^{(\lambda, \mathbf{0})} \right] \quad (6.9)$$

The equation of motion for the unit cell can be written in matrix form by assembling the global stiffness matrix \mathbf{K} from the contributions of all elements i.e. contacts using Eq. 6.9 :

$$\mathbf{F} = \mathbf{M}\ddot{\mathbf{U}} + \mathbf{K}\mathbf{U} \quad (6.10)$$

where $\mathbf{U} = [\mathbf{u}^1, \mathbf{u}^2, \dots, \mathbf{u}^q]^T$ and $\mathbf{F} = [\mathbf{f}^1, \mathbf{f}^2, \dots, \mathbf{f}^q]^T$ and $\mathbf{M} = \text{diag}\{M^1, M^2, \dots, M^q\}$ is the mass matrix.

Assuming harmonic oscillations of frequency ω and free wave motion we obtain the following generalized eigenvalue problem:

$$[-\omega^2 \mathbf{M} + \mathbf{K}] \mathbf{U} = 0. \quad (6.11)$$

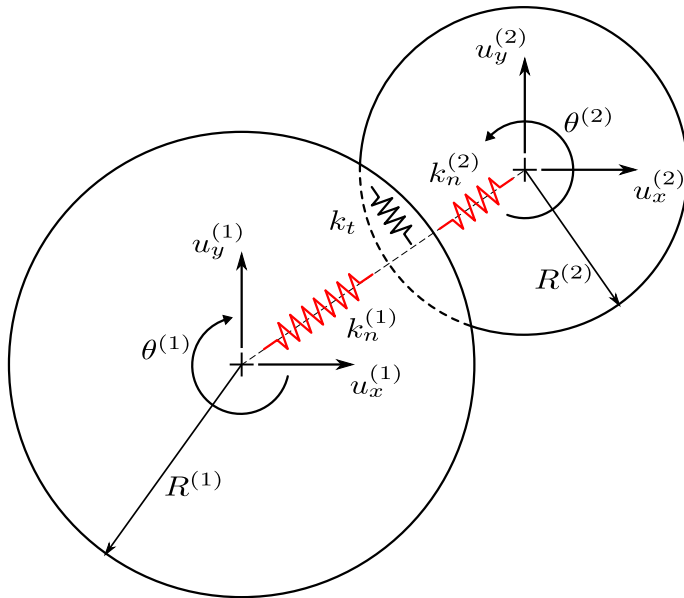


Figure 6.4: Geometry and displacement of two particles in contacts.

Element (contact) stiffness matrix

If particles transmit only normal forces along the contact line, contacts can be modelled as truss elements. The stiffness matrix for a truss element in 2D is:

$$K = k_n \begin{bmatrix} \mathbf{a}\mathbf{a}^T & -\mathbf{a}\mathbf{a}^T \\ -\mathbf{a}\mathbf{a}^T & \mathbf{a}\mathbf{a}^T \end{bmatrix} \quad (6.12)$$

where \mathbf{a} is the unit vector along the contact direction and k_n is the normal contact stiffness.

When particles also support transverse loads tangential contact forces must be considered. In this case, the rotation in the third direction is introduced as an additional degree of freedom corresponding to the moment acting on the particles. The equation of equilibrium in local coordinates is given by [69]:

$$\begin{bmatrix} f_x^{(\kappa)} \\ f_y^{(\kappa)} \\ \tau^{(\kappa)} \\ f_x^{(\lambda)} \\ f_y^{(\lambda)} \\ \tau^{(\lambda)} \end{bmatrix} = \underbrace{\begin{bmatrix} k_n & 0 & 0 & -k_n & 0 & 0 \\ 0 & k_t & k_t R^{(\kappa)} & 0 & -k_t & k_t R^{(\lambda)} \\ 0 & k_t R^{(\kappa)} & k_t R^{(\kappa)} R^{(\kappa)} & 0 & k_t R^{(\kappa)} & k_t R^{(\kappa)} R^{(\lambda)} \\ -k_n & 0 & 0 & k_n & 0 & 0 \\ 0 & -k_t & -k_t R^{(\kappa)} & 0 & -k_t & -k_t R^{(\lambda)} \\ 0 & k_t R^{(\lambda)} & k_t R^{(\kappa)} R^{(\kappa)} & 0 & -k_t R^{(\lambda)} & k_t R^{(\lambda)} R^{(\lambda)} \end{bmatrix}}_{K^{(\lambda\kappa)}} \begin{bmatrix} u_x^{(\kappa)} \\ u_y^{(\kappa)} \\ \theta^{(\kappa)} \\ u_x^{(\lambda)} \\ u_y^{(\lambda)} \\ \theta^{(\lambda)} \end{bmatrix} \quad (6.13)$$

where $K^{(\lambda\kappa)}$ is the stiffness matrix, $R^{(\kappa)}$ and $R^{(\lambda)}$ are the radii of the particles and k_t is the tangential contact stiffness.

Chapter 7

Conclusions and Recommendations

Conclusions

Understanding the mechanical properties of granular materials is important both for practical and fundamental reasons. In the first part of this thesis, we have studied the constitutive behavior of idealized granular materials modeled as random polydisperse sphere packings using the discrete element method. Particle scale properties such as coefficient of friction and polydispersity were varied systematically to characterize their effect on the macroscopic stress-strain response. Several conclusions can be drawn from the analysis:

In isotropically deformed systems:

1. The coordination number is discontinuous at the transition between solid and fluid like states. Previous studies have shown that it obeys a power law of volume fraction near jamming. Our results indicate that this relation holds in a broader range extending to very high densities.
2. The critical volume fraction marking the transition, increases with particle polydispersity¹ and decreases with the coefficient of friction.
3. The dimensionless pressure scales with the ratio of contact number density and the

¹Recent studies have shown that it saturates at large polydispersities when the radius is uniformly distributed (c.f. Ogarko and Luding [112]).

critical volume fraction for different polydispersities which indicates that it is characterized by these numbers.

4. A constitutive model for the bulk modulus derived from the micromechanical stress tensor captures the pressure evolution unifying different polydispersities. Remarkably, this model is also applicable to frictional packings, despite not taking friction into account.

In packings under triaxial loading:

5. The shear strength increases with particle coefficient of friction when the initial volume fraction is fixed. However, the effect is limited and saturates at high values.
6. There is a non monotonic relation between particle friction and the volumetric strain. The maximum compaction is reached at relatively small (i.e. $\mu = 0.3$) coefficient of friction. Higher friction does not improve because particles can “roll” away.
7. The polydispersity determines initial pressure and volume fraction which cannot be imposed simultaneously. When the volume fraction is set constant the initial pressure and the shear strength decrease with polydispersity. If the initial pressure is fixed the opposite is observed, however, the effect of polydispersity on the stress-strain behavior is less pronounced in this case.
8. A hypoplastic constitutive model captures main features of the stress-strain behavior but there is not a perfect quantitative agreement between the model and simulation results. Calibration of the model with simulations suggests that the fourth material coefficient multiplying the deviatoric stress is correlated to the macroscopic angle of friction.

Granular materials are notorious for their disorder. However, artificial crystal structures can be constructed by placing particles on a lattice. The second part of this thesis is dedicated to such two-dimensional granular crystals composed of bi-disperse soft and hard particles. We studied structural transformations in these systems triggered by mechanical loading. The main conclusions of this study are:

9. Upon uniaxial compression a uniform hexagonal pattern is formed from an initial square lattice arrangement.
10. The characteristics of the transformation are predominantly controlled by the geometry. Material properties of the particles seem to play a lesser role. If the ratio of small and large particles’ radii is small and within a certain range the transformation is smooth and homogeneous. Moreover, it is quasi-reversible i.e. the initial arrangement is almost recovered after unloading.
11. Pattern transformation changes the band structure of the granular crystal. Bandgaps open and close as the particles rearrange.

Recommendations

The work in this thesis is a first step towards understanding the relation between microscale particle properties and macroscopic behavior of granular materials and pattern transformation in regular arrays of particles. There are several limitations and many aspects can be improved in future research.

In disordered packings, interactions between particles were modeled with a linear contact force-overlap law. This simple approach is able to capture important features of granular materials, however simulations with more realistic contact models such as Hertz-Mindlin should be performed to generalize the results in this thesis for the case of elastic spheres. Similarly, the constitutive model for the bulk modulus was derived assuming a linear contact force. Effective medium theories based on Hertz contact model were proposed previously, but they did not take into account structure evolution. Therefore, a possible direction of future research is the generalization of the model to include non-linear contact forces together with the structural changes. Interestingly, friction does not destroy the validity of relations derived from frictionless packings. Furthermore, non-affine deformation of particles was not considered in the derivation. This should be given particular attention if a model were to be developed for the shear modulus as previous studies indicate that non-affine deformations play an important role in this case.

Furthermore, the simulation results should be checked against available experiments and if required new experiments should be carried out. Some parameters such as the coordination number are not easily accessible in experiments. Therefore, the use of advanced imaging techniques like X-ray tomography may be necessary for this purpose.

Anisotropy in granular materials is apparent at the microscale and can also be measured in the macroscopic stress-strain behavior. We have shown that the material coefficients of the hypoplastic model can be related to the stress anisotropy. However, a study was not conducted for the microscopic origins of it and therefore is a future direction of research. Likewise, a rigorous derivation of the relation between particle properties and the material coefficients of the hypoplastic model was not attempted, even though calibration with simulation results indicated that they are correlated. Note that the hypoplastic model does not contain structural anisotropy as found in DEM simulations.

Discrete element simulations of pattern transformation were performed with a non-linear contact force model calibrated with finite element simulations. A drawback of this approach is that the model considers only a single contact at a time and volumetric effects arising in multiple contact situations are not taken into account. This is the reason why the stress is underestimated in discrete element simulations at large compression. To overcome this, the model can be calibrated with finite element simulations of multiple contacts, however it is yet to be determined how the force will be distributed among different contacts. Furthermore,

the stress may be overestimated at low compression, in this case. A more robust approach would be to incorporate the number of contacts in the model.

It would be interesting for future research to investigate whether similar pattern transformation occurs in granular crystals composed of particles other than cylindrical shape and topology. The study could be repeated also for three-dimensional crystals and different initial lattice arrangements. Finally, the prospect of using pattern transformation in tunable acoustic devices should be verified with physical realizations.

Outlook

Discrete particle methods offer a convenient way to simulate the collective behavior of granular materials. With the advance of computational technology their use in practical situations will certainly increase. However, the computational cost is still very high and it is unlikely, at least in the near future, that they will replace mainstream analysis tools based on the continuum assumption. Nevertheless, they can still play an important role in bridging the gap between microscale and macroscopic continuum by providing valuable insight for the development of physically based, realistic constitutive models. We hope that the results presented in this thesis will be useful in the future for the formulation of such constitutive models.

Granular materials are often considered as a paradigm to understand the behavior of more complex materials. For example as mentioned in the introduction, jamming is a common property of many amorphous materials that is usually studied with simplified disk or sphere models. Similarly, the pattern transformation presented in this work is reminiscent of martensitic phase transformations in shape memory alloys and could provide an opportunity to study and better understand this phenomenon directly at the macroscale.

References

- [1] I. Agnolin and J.-N. Roux. Internal states of model isotropic granular packings. I. Assembling process, geometry, and contact networks. *Physical Review E*, 76(6):1–27, Dec. 2007.
- [2] M. Allen and D. Tildesley. *Computer Simulation of Liquids*. Oxford University Press, 1993.
- [3] L. Anand. Granular materials: constitutive equations and strain localization. *Journal of the Mechanics and Physics of Solids*, 48(8):1701–1733, Aug. 2000.
- [4] S. Antony and N. Kruyt. Role of interparticle friction and particle-scale elasticity in the shear-strength mechanism of three-dimensional granular media. *Physical Review E*, 79(3):31308, Mar. 2009.
- [5] I. Aranson and L. Tsimring. Patterns and collective behavior in granular media: Theoretical concepts. *Reviews of Modern Physics*, 78(2):641–692, June 2006.
- [6] J. Bardet. Observations on the effects of particle rotations on the failure of idealized granular materials. *Mechanics of Materials*, 18(2):159–182, July 1994.
- [7] K. Been and M. G. Jefferies. A state parameter for sands. *Géotechnique*, 35(2):99–112, Jan. 1985.
- [8] J. Berryman. Random close packing of hard spheres and disks. *Physical Review A*, 27(2):1053–1061, Feb. 1983.
- [9] K. Bertoldi and M. Boyce. Mechanically triggered transformations of phononic band gaps in periodic elastomeric structures. *Physical Review B*, 77(5), Feb. 2008.
- [10] N. Boechler, J. Yang, G. Theocharis, P. G. Kevrekidis, and C. Daraio. Tunable vibrational band gaps in one-dimensional diatomic granular crystals with three-particle unit cells. *Journal of Applied Physics*, 109(7):074906, 2011.
- [11] L. Brillouin. *Wave Propagation in Periodic Structures*, volume 301. Dover Publications, 1953.
- [12] E. Brown, N. Rodenberg, J. Amend, A. Mozeika, E. Steltz, M. R. Zakin, H. Lipson, and H. M. Jaeger. Universal robotic gripper based on the jamming of granular material. *Proceedings of the National Academy of Sciences*, 107(44):18809–18814, Oct. 2010.
- [13] X. Cheng, J. Lechman, A. Fernandez-Barbero, G. Grest, H. Jaeger, G. Karczmar, M. Möbius, and S. Nagel. Three-Dimensional Shear in Granular Flow. *Physical Review Letters*, 96(3):38001, Jan. 2006.
- [14] J. Christoffersen, M. Mehrabadi, and S. Nemat-Nasser. A Micromechanical Description of Granular Material Behavior. *Journal of Applied Mechanics*, 48(2):339, 1981.

- [15] A. Clarke and J. Wiley. Numerical simulation of the dense random packing of a binary mixture of hard spheres: Amorphous metals. *Physical Review B*, 35(14):7350–7356, May 1987.
- [16] C. Coste, E. Falcon, and S. Fauve. Solitary waves in a chain of beads under Hertz contact. *Physical Review E*, 56(5):6104–6117, Nov. 1997.
- [17] C. A. Coulomb. Essai sur une application des règles de maximis & minimis à quelques problèmes de statique, relatifs à l'architecture. *Académie des Sciences Mémoires présentées par divers savants*, 7:343–382, 1776.
- [18] P. A. Cundall and O. D. L. Strack. A discrete numerical model for granular assemblies. *Géotechnique*, 29(1):47–65, Jan. 1979.
- [19] F. da Cruz, S. Emam, M. Prochnow, J.-N. Roux, and F. Chevoir. Rheophysics of dense granular materials: Discrete simulation of plane shear flows. *Physical Review E*, 72(2), Aug. 2005.
- [20] C. Daraio, V. Nesterenko, E. Herbold, and S. Jin. Strongly nonlinear waves in a chain of Teflon beads. *Physical Review E*, 72(1):16603, July 2005.
- [21] C. Daraio, V. Nesterenko, E. Herbold, and S. Jin. Energy Trapping and Shock Disintegration in a Composite Granular Medium. *Physical Review Letters*, 96(5), Feb. 2006.
- [22] C. Daraio, V. Nesterenko, E. Herbold, and S. Jin. Tunability of solitary wave properties in one-dimensional strongly nonlinear phononic crystals. *Physical Review E*, 73(2):26610, Feb. 2006.
- [23] C. T. David, R. G. Rojo, H. J. Herrmann, and S. Luding. Hysteresis and creep in powders and grains. In R. Garcia-Rojo, H. J. Herrmann, and S. McNamara, editors, *Powders and Grains 2005*, pages 291–294, Leiden, Netherlands, 2005. Balkema.
- [24] R. de Borst and L. Sluys. Localisation in a Cosserat continuum under static and dynamic loading conditions. *Computer Methods in Applied Mechanics and Engineering*, 90(1-3):805–827, Sept. 1991.
- [25] P. de Gennes. Granular matter: a tentative view. *Reviews of Modern Physics*, 71(2):S374–S382, Mar. 1999.
- [26] J. Desrues and G. Viggiani. Strain localization in sand: an overview of the experimental results obtained in Grenoble using stereophotogrammetry. *International Journal for Numerical and Analytical Methods in Geomechanics*, 28(4):279–321, Apr. 2004.
- [27] A. Donev, I. Cisse, D. Sachs, E. A. Variano, F. H. Stillinger, R. Connelly, S. Torquato, and P. M. Chaikin. Improving the density of jammed disordered packings using ellipsoids. *Science*, 303(5660):990–3, Mar. 2004.
- [28] A. Donev, S. Torquato, and F. Stillinger. Pair correlation function characteristics of nearly jammed disordered and ordered hard-sphere packings. *Physical Review E*, 71(1):011105, Jan. 2005.
- [29] R. Doney and S. Sen. Impulse absorption by tapered horizontal alignments of elastic spheres. *Physical Review E*, 72(4):1–11, Oct. 2005.
- [30] D. C. Drucker and W. Prager. Soil mechanics and plastic analysis or limit design. *Quarterly of Applied mathematics*, 10:157–165, 1952.
- [31] O. Durán, N. Kruyt, and S. Luding. Analysis of three-dimensional micro-mechanical strain formulations for granular materials: Evaluation of accuracy. *International Journal of Solids and Structures*, 47(2):251–260, Jan. 2010.
- [32] O. Durán, N. Kruyt, and S. Luding. Micro-mechanical analysis of deformation characteristics of three-dimensional granular materials. *International Journal of Solids and Structures*, 47(17):2234–2245, Aug. 2010.

- [33] O. Durán, M. Madadi, and S. Luding. Fabric and Stress Tensors for Frictionless, Polydisperse, Three Dimensional Granular Media. 2010.
- [34] R. S. Elliott, N. Triantafyllidis, and J. A. Shaw. Stability of crystalline solids—I: Continuum and atomic lattice considerations. *Journal of the Mechanics and Physics of Solids*, 54(1):161–192, Jan. 2006.
- [35] D. Fenistein and M. Van Hecke. Kinematics: wide shear zones in granular bulk flow. *Nature*, 425(6955):256, Sept. 2003.
- [36] N. Fleck and J. Hutchinson. Strain gradient plasticity. *Advances in Applied Mechanics*, 33:295–361, 1997.
- [37] Y. Forterre and O. Pouliquen. Flows of Dense Granular Media. *Annual Review of Fluid Mechanics*, 40(1):1–24, Jan. 2008.
- [38] J. D. Goddard. Continuum Modeling of Granular Assemblies. In H. J. Herrmann, J. P. Hovi, and S. Luding, editors, *Physics of dry granular media - NATO ASI Series E 350*, pages 1–24, Dordrecht, 1998. Kluwer Academic Publishers.
- [39] I. Goldhirsch. Rapid Granular Flows. *Annual Review of Fluid Mechanics*, 35(1):267–293, Jan. 2003.
- [40] F. Göncü, O. Durán, and S. Luding. Jamming in frictionless packings of spheres: determination of the critical volume fraction. In M. Nakagawa and S. Luding, editors, *Powders and Grains 2009: Proceedings of the 6th International Conference on Micromechanics of Granular Media, 13-17 July 2009, Golden, Colorado*, pages 531–534. AIP, 2009.
- [41] F. Göncü, O. Durán, and S. Luding. Constitutive relations for the isotropic deformation of frictionless packings of polydisperse spheres. *Comptes Rendus Mécanique*, 338(10-11):570–586, Oct. 2010.
- [42] F. Göncü and S. Luding. From “soft” particle simulations to macroscopic constitutive relations. In *World Congress of Particle Technology 6, Nuremberg, CD-Proceedings*, 2010.
- [43] F. Göncü and S. Luding. Effect of particle friction and polydispersity on the macroscopic stress-strain relations of granular materials. *Acta Geotechnica*, Submitted, 2012.
- [44] F. Göncü, S. Luding, and K. Bertoldi. Exploiting pattern transformation to tune phononic band gaps in a two-dimensional granular crystal. *The Journal of the Acoustical Society of America*, 131(6), 2012.
- [45] F. Göncü, S. Willshaw, J. Shim, J. Cusack, S. Luding, T. Mullin, and K. Bertoldi. Deformation induced pattern transformation in a soft granular crystal. *Soft Matter*, 7(6):2321, 2011.
- [46] J. Gray and K. Hutter. Pattern formation in granular avalanches. *Continuum Mechanics and Thermodynamics*, 9(6):341–345, Dec. 1997.
- [47] B. A. Grzybowski, A. Winkleman, J. A. Wiles, Y. Brumer, and G. M. Whitesides. Electrostatic self-assembly of macroscopic crystals using contact electrification. *Nature materials*, 2(4):241–5, Apr. 2003.
- [48] E. B. Herbold, J. Kim, V. F. Nesterenko, S. Y. Wang, and C. Daraio. Pulse propagation in a linear and nonlinear diatomic periodic chain: effects of acoustic frequency band-gap. *Acta Mechanica*, 205(1-4):85–103, Apr. 2009.
- [49] H. J. Herrmann and S. Luding. Modeling granular media on the computer. *Continuum Mechanics and Thermodynamics*, 10(4):189–231, Aug. 1998.
- [50] J. M. Hill and a. P. S. Selvadurai. Mathematics and mechanics of granular materials. *Journal of Engineering Mathematics*, 52(1):1–9, July 2005.

- [51] K. Hutter and K. R. Rajagopal. On flows of granular materials. *Continuum Mechanics and Thermodynamics*, 6(2):81–139, 1994.
- [52] C. Inerra, V. Tournat, and V. Gusev. A method of controlling wave propagation in initially spatially periodic media. *Europhysics Letters (EPL)*, 78(4):44001, May 2007.
- [53] H. Jaeger, S. Nagel, and R. Behringer. Granular solids, liquids, and gases. *Reviews of Modern Physics*, 68(4):1259–1273, Oct. 1996.
- [54] H. M. Jaeger and S. R. Nagel. Physics of the granular state. *Science*, 255(5051):1523–31, Mar. 1992.
- [55] J.-H. Jang, C. Y. Koh, K. Bertoldi, M. C. Boyce, and E. L. Thomas. Combining pattern instability and shape-memory hysteresis for phononic switching. *Nano Letters*, 9(5):2113–9, May 2009.
- [56] A. W. Jenike. Storage and Flow of Solids, Bulletin No. 123. *Bulletin of the University of Utah*, 53(26):198, 1964.
- [57] J. T. Jenkins and M. Satake, editors. *Micromechanics of Granular Materials*. Elsevier, Amsterdam, 1988.
- [58] J. Jensen. Phononic band gaps and vibrations in one- and two-dimensional mass-spring structures. *Journal of Sound and Vibration*, 266(5):1053–1078, Oct. 2003.
- [59] K.-U. Jeong, J.-H. Jang, C. Y. Koh, M. J. Graham, K.-Y. Jin, S.-J. Park, C. Nah, M.-H. Lee, S. Z. D. Cheng, and E. L. Thomas. Colour-tunable spiral photonic actuators. *Journal of Materials Chemistry*, 19(14):1956, 2009.
- [60] X. Jia, C. Caroli, and B. Velicky. Ultrasound Propagation in Externally Stressed Granular Media. *Physical Review Letters*, 82(9):1863–1866, Mar. 1999.
- [61] K. L. Jim, C. W. Leung, S. T. Lau, S. H. Choy, and H. L. W. Chan. Thermal tuning of phononic bandstructure in ferroelectric ceramic/epoxy phononic crystal. *Applied Physics Letters*, 94(19):193501, 2009.
- [62] P. Jop, Y. Forterre, and O. Pouliquen. Crucial role of sidewalls in granular surface flows: consequences for the rheology. *Journal of Fluid Mechanics*, 541(-1):167, Oct. 2005.
- [63] P. Jop, Y. Forterre, and O. Pouliquen. A constitutive law for dense granular flows. *Nature*, 441(7094):727–30, June 2006.
- [64] A. Khelif, A. Choujaa, S. Benchabane, B. Djafari-Rouhani, and V. Laude. Guiding and bending of acoustic waves in highly confined phononic crystal waveguides. *Applied Physics Letters*, 84(22):4400, 2004.
- [65] S. J. Koh. Strategies for Controlled Placement of Nanoscale Building Blocks. *Nanoscale Research Letters*, 2(11):519–545, Oct. 2007.
- [66] D. Kolymbas. An outline of hypoplasticity. *Archive of Applied Mechanics*, 61:143–154, 1991.
- [67] D. Kolymbas. *Introduction to Hypoplasticity (Advances in Geotechnical Engineering and Tunneling)*. A.A. Balkema, Rorredam, 1 edition, Nov. 1999.
- [68] D. Kolymbas and W. Wu. Recent results of triaxial tests with granular materials. *Powder Technology*, 60(2):99–119, Feb. 1990.
- [69] N. Kruyt, I. Agnolin, S. Luding, and L. Rothenburg. Micromechanical study of elastic moduli of loose granular materials. *Journal of the Mechanics and Physics of Solids*, 58(9):1286–1301, Sept. 2010.
- [70] N. P. Kruyt. Three-dimensional lattice-based dispersion relations for granular materials. In J. Goddard, P. Giovine, and J. T. Jenkins, editors, *IUTAM-ISIMM Symposium on Mathematical Modeling and Physical Instances of Granular Flows*, pages 405–415, Reggio Calabria (Italy), 14.18 September 2009, 2010. AIP.

- [71] N. P. Kruyt and L. Rothenburg. Micromechanical Definition of the Strain Tensor for Granular Materials. *Journal of Applied Mechanics*, 63(3):706, 1996.
- [72] N. Kumar, F. Göncü, V. Magnanimo, and S. Luding. Analysis of the components of a hypoplastic constitutive model. *In preparation*.
- [73] M. Lätzel, S. Luding, and H. J. Herrmann. Macroscopic material properties from quasi-static, microscopic simulations of a two-dimensional shear-cell. *Granular Matter*, 2(3):123–135, June 2000.
- [74] A. Lazaridi and V. Nesterenko. Observation of a new type of solitary waves in a one-dimensional granular medium. *Journal of Applied Mechanics and Technical Physics*, pages 405–408, 1985.
- [75] C. N. Likos and C. L. Henley. Complex alloy phases for binary hard-disc mixtures. *Philosophical Magazine Part B*, 68(1):85–113, July 1993.
- [76] Y. Y. Lin, C. Y. Hui, and A. Jagota. The Role of Viscoelastic Adhesive Contact in the Sintering of Polymeric Particles. *Journal of colloid and interface science*, 237(2):267–282, May 2001.
- [77] A. J. Liu and S. R. Nagel. Nonlinear dynamics - Jamming is not just cool any more. *Nature*, 396(6706):21–22, 1998.
- [78] C.-H. Liu and S. R. Nagel. Sound and vibration in granular materials. *Journal of Physics: Condensed Matter*, 6(23A):A433–A436, June 1994.
- [79] S. Luding. Collisions & Contacts between two particles. In H. J. Herrmann, J. P. Hovi, and S. Luding, editors, *Physics of dry granular media - NATO ASI Series E350*, page 285, Dordrecht, 1998. Kluwer Academic Publishers.
- [80] S. Luding. Micro-Macro Models for Anisotropic Granular Media. In P. A. Vermeer, W. Ehlers, H. J. Herrmann, and E. Ramm, editors, *Modelling of Cohesive-Frictional Materials*, pages 195–206, Leiden, Netherlands, 2004. Balkema.
- [81] S. Luding. Anisotropy in cohesive, frictional granular media. *Journal of Physics: Condensed Matter*, 17(24):S2623–S2640, June 2005.
- [82] S. Luding. The Effect of Friction on Wide Shear Bands. *Particulate Science and Technology*, 26(1):33–42, Dec. 2007.
- [83] S. Luding. Cohesive, frictional powders: contact models for tension. *Granular Matter*, 10(4):235–246, Mar. 2008.
- [84] S. Luding. Constitutive relations for the shear band evolution in granular matter under large strain. *Partic-uology*, 6(6):501–505, Dec. 2008.
- [85] S. Luding. Introduction to Discrete Element Methods: Basics of Contact Force Models and how to perform the Micro-Macro Transition to Continuum Theory,. *European Journal of Environmental and Civil Engineering*, 12(7-8):785–826, 2008.
- [86] S. Luding and E. Bauer. Evolution of swelling pressure of cohesive-frictional, rough and elasto-plastic granulates. In M. Jiang, MJ and Liu, F and Bolton, editor, *Geomechanics and Geotechnics: From Micro to Macro, Vols 1 and 2*, pages 495–499, 6000 BROKEN SOUND PARKWAY NW, STE 300, BOCA RATON, FL 33487-2742 USA, 2011. Int Soc Soil Mech & Geotechn Engr, CRC PRESS-TAYLOR & FRANCIS GROUP.
- [87] S. Luding and E. S. Perdahcioglu. A Local Constitutive Model with Anisotropy for Various Homogeneous 2D Biaxial Deformation Modes. *Chemie Ingenieur Technik*, 83(5):672–688, May 2011.

- [88] M. Lundberg, K. Krishan, N. Xu, C. S. O'Hern, and M. Dennin. Reversible plastic events in amorphous materials. *Physical Review E*, 77(4), Apr. 2008.
- [89] M. Madadi, S. M. Peyghoon, and S. Luding. Stress and fabric for polydisperse, frictionless, dense 2D granular media. In R. Garcia-Rojo, H. J. Herrmann, and S. McNamara, editors, *Powders and Grains 2005*, pages 93–97, Leiden, Netherlands, 2005. Balkema.
- [90] M. Madadi, O. Tsoungui, M. Lätzel, and S. Luding. On the fabric tensor of polydisperse granular materials in 2D. *International Journal of Solids and Structures*, 41(9-10):2563–2580, May 2004.
- [91] V. Magnanimo and S. Luding. A local constitutive model with anisotropy for ratcheting under 2D axial-symmetric isobaric deformation. *Granular Matter*, 13(3):225–232, May 2011.
- [92] T. Majmudar, M. Sperl, S. Luding, and R. Behringer. Jamming Transition in Granular Systems. *Physical Review Letters*, 98(5):1–4, Jan. 2007.
- [93] T. S. Majmudar and R. P. Behringer. Contact force measurements and stress-induced anisotropy in granular materials. *Nature*, 435(7045):1079–82, June 2005.
- [94] H. Makse, N. Gland, D. Johnson, and L. Schwartz. Why Effective Medium Theory Fails in Granular Materials. *Physical Review Letters*, 83(24):5070–5073, Dec. 1999.
- [95] H. Makse, D. Johnson, and L. Schwartz. Packing of Compressible Granular Materials. *Physical Review Letters*, 84(18):4160–4163, May 2000.
- [96] M. Maldovan and E. L. Thomas. *Periodic Materials and Interference Lithography*. Wiley-VCH Verlag GmbH & Co. KGaA, Weinheim, Germany, Oct. 2008.
- [97] P. G. Martinsson and A. B. Movchan. Vibrations of Lattice Structures and Phononic Band Gaps. *The Quarterly Journal of Mechanics and Applied Mathematics*, 56(1):45–64, Feb. 2003.
- [98] M. Mehrabadi and S. Cowin. Initial planar deformation of dilatant granular materials. *Journal of the Mechanics and Physics of Solids*, 26(4):269–284, Aug. 1978.
- [99] M. Mehrabadi, B. Lorent, and S. Nemat-Nasser. Incremental Constitutive Relations for Granular Materials Based on Micromechanics. *Proceedings of the Royal Society A: Mathematical, Physical and Engineering Sciences*, 441(1913):433–463, June 1993.
- [100] G. D. R. Midi. On dense granular flows. *The European physical journal. E, Soft matter*, 14(4):341–65, Aug. 2004.
- [101] B. Miller, C. O'Hern, and R. Behringer. Stress Fluctuations for Continuously Sheared Granular Materials. *Physical Review Letters*, 77(15):3110–3113, Oct. 1996.
- [102] M. Mooney. A Theory of Large Elastic Deformation. *Journal of Applied Physics*, 11(9):582, 1940.
- [103] O. Mouraille and S. Luding. Sound wave propagation in weakly polydisperse granular materials. *Ultrasonics*, 48(6-7):498–505, Nov. 2008.
- [104] F. Moučka and I. Nezbeda. Detection and Characterization of Structural Changes in the Hard-Disk Fluid under Freezing and Melting Conditions. *Physical Review Letters*, 94(4), Feb. 2005.
- [105] A. Mozeika, E. Steltz, and H. M. Jaeger. The first steps of a robot based on jamming skin enabled locomotion. In *2009 IEEE/RSJ International Conference on Intelligent Robots and Systems*, pages 408–409. IEEE, Oct. 2009.

- [106] D. Mueth, G. Debregeas, G. Karczmar, P. Eng, S. Nagel, and H. Jaeger. Signatures of granular microstructure in dense shear flows. *Nature*, 406(6794):385–9, July 2000.
- [107] D. Mueth, H. Jaeger, and S. Nagel. Force distribution in a granular medium. *Physical Review E*, 57(3):3164–3169, Mar. 1998.
- [108] T. Mullin, S. Deschanel, K. Bertoldi, and M. Boyce. Pattern Transformation Triggered by Deformation. *Physical Review Letters*, 99(8):1–4, Aug. 2007.
- [109] S. Nemat-Nasser. A micromechanically-based constitutive model for frictional deformation of granular materials. *Journal of the Mechanics and Physics of Solids*, 48(6-7):1541–1563, June 2000.
- [110] V. F. Nesterenko. Propagation of nonlinear compression pulses in granular media. *Journal of Applied Mechanics and Technical Physics*, pages 733–743, 1984.
- [111] M. Oda, J. Konishi, and S. Nemat-Nasser. Experimental micromechanical evaluation of strength of granular materials: Effects of particle rolling. *Mechanics of Materials*, 1(4):269–283, Dec. 1982.
- [112] V. Ogarko and S. Luding. Equation of state and jamming density for equivalent bi- and polydisperse, smooth, hard sphere systems. *The Journal of chemical physics*, 136(12):124508, Mar. 2012.
- [113] C. O’Hern, S. Langer, A. Liu, and S. Nagel. Random Packings of Frictionless Particles. *Physical Review Letters*, 88(7):3–6, Jan. 2002.
- [114] C. S. O’Hern, L. E. Silbert, and S. R. Nagel. Jamming at zero temperature and zero applied stress: The epitome of disorder. *Physical Review E*, 68(1):11306–11319, July 2003.
- [115] G. Onoda and E. Liniger. Random loose packings of uniform spheres and the dilatancy onset. *Physical Review Letters*, 64(22):2727–2730, May 1990.
- [116] E. T. Owens and K. E. Daniels. Sound propagation and force chains in granular materials. *Europhysics Letters*, 94(5):54005, June 2011.
- [117] Y. Pennec, B. Djafari-Rouhani, J. Vasseur, A. Khelif, and P. Deymier. Tunable filtering and demultiplexing in phononic crystals with hollow cylinders. *Physical Review E*, 69(4):3–8, Apr. 2004.
- [118] P.-E. Peyneau and J.-N. Roux. Solidlike behavior and anisotropy in rigid frictionless bead assemblies. *Physical Review E*, 78(4), Oct. 2008.
- [119] A. S. Phani, J. Woodhouse, and N. Fleck. Wave propagation in two-dimensional periodic lattices. *The Journal of the Acoustical Society of America*, 119(4):1995, 2006.
- [120] O. Reynolds. LVII. On the dilatancy of media composed of rigid particles in contact. With experimental illustrations. *Philosophical Magazine Series 5*, 20(127):469–481, Dec. 1885.
- [121] R. S. Rivlin. Large Elastic Deformations of Isotropic Materials. IV. Further Developments of the General Theory. *Philosophical Transactions of the Royal Society A: Mathematical, Physical and Engineering Sciences*, 241(835):379–397, Oct. 1948.
- [122] J.-F. Robillard, O. B. Matar, J. O. Vasseur, P. A. Deymier, M. Stippinger, A.-C. Hladky-Hennion, Y. Pennec, and B. Djafari-Rouhani. Tunable magnetoelastic phononic crystals. *Applied Physics Letters*, 95(12):124104, 2009.
- [123] J. Rudnicki and J. Rice. Conditions for the localization of deformation in pressure-sensitive dilatant materials. *Journal of the Mechanics and Physics of Solids*, 23(6):371–394, Dec. 1975.

- [124] B. Scarlett, M. van der Kraan, and R. J. M. Janssen. Porosity: a parameter with no direction. *Philosophical Transactions of the Royal Society A: Mathematical, Physical and Engineering Sciences*, 356(1747):2623–2648, Nov. 1998.
- [125] A. N. Schofield and P. Wroth. *Critical state soil mechanics*. McGraw-Hill, 1968.
- [126] J. Schwedes. Review on testers for measuring flow properties of bulk solids. *Granular Matter*, 5(1):1–43, May 2003.
- [127] L. Silbert, D. Ertas, G. Grest, T. Halsey, and D. Levine. Geometry of frictionless and frictional sphere packings. *Physical Review E*, 65(3):51302, Feb. 2002.
- [128] S. Singamaneni and V. V. Tsukruk. Buckling instabilities in periodic composite polymeric materials. *Soft Matter*, 6(22):5681, 2010.
- [129] E. Somfai, J.-N. Roux, J. Snoeijer, M. van Hecke, and W. van Saarloos. Elastic wave propagation in confined granular systems. *Physical Review E*, 72(2), Aug. 2005.
- [130] A. Spadoni and C. Daraio. Generation and control of sound bullets with a nonlinear acoustic lens. *Proceedings of the National Academy of Sciences of the United States of America*, 107(16):7230–4, Apr. 2010.
- [131] A. Suiker, A. Metrikine, and R. de Borst. Comparison of wave propagation characteristics of the Cosserat continuum model and corresponding discrete lattice models. *International Journal of Solids and Structures*, 38(9):1563–1583, Feb. 2001.
- [132] A. S. J. Suiker and R. de Borst. Enhanced continua and discrete lattices for modelling granular assemblies. *Philosophical transactions. Series A, Mathematical, physical, and engineering sciences*, 363(1836):2543–80, Nov. 2005.
- [133] A. S. J. Suiker and N. a. Fleck. Frictional Collapse of Granular Assemblies. *Journal of Applied Mechanics*, 71(3):350, 2004.
- [134] T. S. Tan, K. K. Phoon, D. W. Hight, and S. Leroueil, editors. *Characterisation and engineering properties of natural soils*, volume 3-4. Taylor & Francis, 2002.
- [135] A. Tordesillas. Force chain buckling, unjamming transitions and shear banding in dense granular assemblies. *Philosophical Magazine*, 87(32):4987–5016, Nov. 2007.
- [136] S. Torquato, T. Truskett, and P. Debenedetti. Is Random Close Packing of Spheres Well Defined? *Physical Review Letters*, 84(10):2064–2067, Mar. 2000.
- [137] L. R. G. Treloar. The elasticity of a network of long-chain molecules?II. *Transactions of the Faraday Society*, 39:241, 1943.
- [138] I. Vardoulakis and H. B. Mühlhaus. The thickness of shear bands in granular materials. *Géotechnique*, 37(3):271–283, Jan. 1987.
- [139] K. Walton. The effective elastic moduli of a random packing of spheres. *Journal of the Mechanics and Physics of Solids*, 35(2):213–226, Jan. 1987.
- [140] W. Wu. Rational approach to anisotropy of sand. *International Journal for Numerical and Analytical Methods in Geomechanics*, 22(11):921–940, Nov. 1998.
- [141] W. Wu, E. Bauer, and D. Kolymbas. Hypoplastic constitutive model with critical state for granular materials. *Mechanics of Materials*, 23(1):45–69, May 1996.

-
- [142] W. Wu and D. Kolymbas. Numerical testing of the stability criterion for hypoplastic constitutive equations. *Mechanics of Materials*, 9(3):245–253, Nov. 1990.
- [143] M. Wyart, L. Silbert, S. Nagel, and T. Witten. Effects of compression on the vibrational modes of marginally jammed solids. *Physical Review E*, 72(5), Nov. 2005.
- [144] J.-K. Yang, C. Schreck, H. Noh, S.-F. Liew, M. Guy, C. O’Hern, and H. Cao. Photonic-band-gap effects in two-dimensional polycrystalline and amorphous structures. *Physical Review A*, 82(5), Nov. 2010.
- [145] J. Yeh. Control analysis of the tunable phononic crystal with electrorheological material. *Physica B: Condensed Matter*, 400(1-2):137–144, Nov. 2007.
- [146] H. Zhu, M. M. Mehrabadi, and M. Massoudi. Incorporating the effects of fabric in the dilatant double shearing model for planar deformation of granular materials. *International Journal of Plasticity*, 22(4):628–653, Apr. 2006.
- [147] X. Zhu, Y. Zhang, D. Chandra, S.-C. Cheng, J. M. Kikkawa, and S. Yang. Two-dimensional photonic crystals with anisotropic unit cells imprinted from poly(dimethylsiloxane) membranes under elastic deformation. *Applied Physics Letters*, 93(16):161911, 2008.

Curriculum vitae

Fatih Göncü

Born on September 26, 1982 in Ilgaz, Turkey

June 2000	High school diploma, Ankara Anadolu Lisesi
August 2005	Bachelor of Science in Textile Engineering, Istanbul Technical University
Sep. 2006 - Feb. 2007	Internship, Philips Research Laboratories, Eindhoven
June 2007	Master of Engineering in Mechanical Engineering, Institut National des Sciences Appliquées de Lyon
September 2008	Master of Science in Applied Mathematics, École Normale Supérieure de Cachan
Feb. 2008 - Feb. 2012	PhD candidate, Delft University of Technology
May - November 2010	Visiting researcher, Harvard School of Engineering and Applied Sciences
May - August 2011	Harvard School of Engineering and Applied Sciences
March - August 2012	Researcher, University of Twente

Publications

Journal Papers

1. F. Göncü, O. Durán, and S. Luding. Constitutive relations for the isotropic deformation of frictionless packings of polydisperse spheres. *Comptes Rendus Mécanique*, 338(10-11):570–586, Oct. 2010
2. F. Göncü, S. Willshaw, J. Shim, J. Cusack, S. Luding, T. Mullin, and K. Bertoldi. Deformation induced pattern transformation in a soft granular crystal. *Soft Matter*, 7(6):2321, 2011

3. F. Göncü, S. Luding, and K. Bertoldi. Exploiting pattern transformation to tune phononic band gaps in a two-dimensional granular crystal. *The Journal of the Acoustical Society of America*, 131(6), 2012
4. F. Göncü and S. Luding. Effect of particle friction and polydispersity on the macroscopic stress-strain relations of granular materials. *Acta Geotechnica*, Submitted, 2012

Proceedings and Abstracts

5. F. Göncü, O. Durán, and S. Luding. Jamming in frictionless packings of spheres: determination of the critical volume fraction. In M. Nakagawa and S. Luding, editors, *Powders and Grains 2009: Proceedings of the 6th International Conference on Micromechanics of Granular Media, 13-17 July 2009, Golden, Colorado*, pages 531–534. AIP, 2009
6. F. Göncü and S. Luding. From “soft” particle simulations to macroscopic constitutive relations. In *World Congress of Particle Technology 6, Nuremberg, CD-Proceedings*, 2010
7. K. Bertoldi, J. Shim, F. Göncü, S. Willshaw, T. Mullin, and S. Luding, Pattern switches in granular crystals, *APS March Meeting* 2011.
8. F. Göncü, S. Luding, and K. Bertoldi, Dispersion and Band Gaps in Binary Ordered Structures *8th European Solid Mechanics Conference 2012*, Graz Austria
9. N. Kumar, F. Göncü, V. Magnanimo and S. Luding, Analysis of the components of a hypoplastic constitutive model, *8th European Solid Mechanics Conference 2012*, Graz Austria

Propositions

1. The effect of particle friction on the macroscopic stress-strain response of disordered sphere packings is stronger than the effect of particle polydispersity.
2. A two-dimensional granular crystal composed of soft and hard cylindrical particles undergoes a pattern transformation from an initial square lattice to hexagon-like structure when subjected to uniaxial compression.
3. Pattern transformation can be used to control wave propagation in soft granular crystals.
4. Discrete particle methods will eventually be the main tool to analyze granular materials.
5. Disorder and discreteness are the main reasons of the non-linear mechanical behavior of granular materials.
6. It is not necessary neither important for the prime minister of a country to speak a foreign language.
7. The view of Turkish people about the Ottoman Empire is generally biased towards extremes. Some refuse to attribute it any merit while others ignore obvious mistakes. Unfortunately, foreigners are not more objective on this topic.
8. Religion and people who adhere to it will always exist unless science gives a definitive answer to the existential questions of mankind.
9. Good parenting balances between discipline and freedom. Although freedom must always prevail.
10. Successful governments bring together people sharing the same passion and ideal regardless of their background, race or nationality.

These propositions are considered opposable and defensible and as such have been approved by the supervisors Prof.dr. S. Luding and Prof.dr. A. Schmidt-Ott.

Stellingen

1. Het effect van wrijving op de macroscopische spanning-rek relatie van ongeordende pakkingen van bolvormige deeltjes is sterker dan het effect van deeltjes polydispersiteit.
2. Een tweedimensionaal granulaair kristal, bestaande uit harde en zachte cilindrische deeltjes, ondergaat een transformatie van een initieel rechthoekig rooster naar een hexagonaalachtige structuur, wanneer belast met uniaxiale compressie.
3. Structuurtransformaties kunnen gebruikt worden om golfpropagatie in zachte granulaire kristallen te beheersen.
4. Discrete deeltjesmethoden, zullen uiteindelijk het voornaamste gereedschap worden om granulaire materialen te analyseren.
5. Wanorde en discreetheid zijn de belangrijkste oorzaken van het mechanische niet-lineaire gedrag van granulaire materialen.
6. Het is niet noodzakelijk, noch belangrijk voor een minister-president om een buitenlandse taal te spreken.
7. De standpunten van Turken, betreffende het Ottomaanse rijk, zijn voornamelijk verdeeld over de twee extremen. Sommigen weigeren het enige verdienste toe te schrijven, waar anderen de Ottomaanse periode verheerlijken en daarbij gemaakte fouten negeren. Jammer genoeg zijn buitenlanders ook niet objectief over dit onderwerp.
8. Geloof en gelovigen zullen altijd blijven bestaan, tenzij de wetenschap een sluitend antwoord geeft op de vraag van het bestaan.
9. Goed ouderschap balanceert tussen discipline en vrijheid, hoewel vrijheid altijd moet overheersen.
10. Succesvolle overheden/regeringen brengen mensen met dezelfde passies en idealen samen, onafhankelijk van hun achtergrond, ras en nationaliteit.

Deze stellingen worden oponeerbaar en verdedigbaar geacht en zijn als zodanig goedgekeurd door de promotoren Prof.dr. S. Luding and Prof.dr. A. Schmidt-Ott.

